1. CMS HADRON CALORIMETER OVERVIEW

1.1 OVERVIEW

1.1.1 The compact muon solenoid

The CMS detector[1] has been designed to detect cleanly the diverse signatures of new physics at the Large Hadron Collider. It will do so by identifying and precisely measuring muons, electrons and photons over a large energy range; by determining the signatures of quarks and gluons through the measurement of jets of charged and neutral particles (hadrons) with moderate precision; and by measuring missing transverse energy flow, which will enable the signatures of non-interacting new particles as well as neutrinos to be identified.

The CMS detector is shown in Fig. 1.1. It consists of a 4 Tesla Solenoidal Superconducting Magnet 13.0m long with an inner diameter of 5.9m. It is surrounded by 5 "wheels" (cylindrical structures) and 2 endcaps (disks) of muon absorber and muon tracking chambers, giving a total length of 21.6m and an outer diameter of 14.6m. This system forms the "Compact Muon Solenoid" which gives the detector its name. The Solenoid Magnet and everything located inside its cryostat are supported by the central wheel. Inside the magnet cryostat are placed three sets of charged particle tracking devices and a two-section calorimeter to measure particle energies (electromagnetic and hadron calorimeters). The cryostat, all detectors inside it, as well as the 5 muon wheels, are in a barrel (cylindrical) geometry and form the so-called "barrel" detectors. The endcap calorimeters are mounted on the inside of the two muon endcaps and are inserted into the ends of the cryostat.

The CMS tracker consists of a silicon pixel barrel and forward disks, followed by silicon microstrip devices again placed in a barrel and forward disk configuration. This silicon tracker system is surrounded by microstrip gas chamber (MSGC) planes with the same barrel and disk geometry. The tracker is located inside the calorimeter system and is suported by it. The CMS electromagnetic calorimeter barrel consists of about 100,000 rectangular crystals of $PbWO_4$, each 23 cm (25.8 X_0, 1.1 λ) in length and approximately 2cm $\times$ 2cm in cross-section. Outside the crystal calorimeter, and supporting it, is the barrel hadron calorimeter, which rests on two rails in the cryostat vessel (on either side of the median plane). The combined response of the electromagnetic and hadron calorimeters provides the raw data for the reconstruction of particle jets and missing transverse energy.

1.1.2 The CMS hadron calorimeter

The combined CMS calorimeter system will measure quark, gluon and neutrino directions and energies by measuring the energy and direction of particle jets and of the missing transverse energy flow. This determination of missing energy will also form a crucial signature for new particles and phenomena, such as will be encountered in the searches for the supersymmetric partners of quarks and gluons. The hadron calorimeter will also help in the identification of electrons, photons and muons in conjunction with the electromagnetic calorimeter and the muon system. Thus the Hadron Calorimeter is an essential subsystem of the CMS detector, and will contribute to most if not all of CMS's physics studies.

The central pseudorapidity range $(|\eta| < 3.0)$ is covered by the barrel and endcap calorimeter system consisting of a hermetic crystal electromagnetic calorimeter (ECAL)

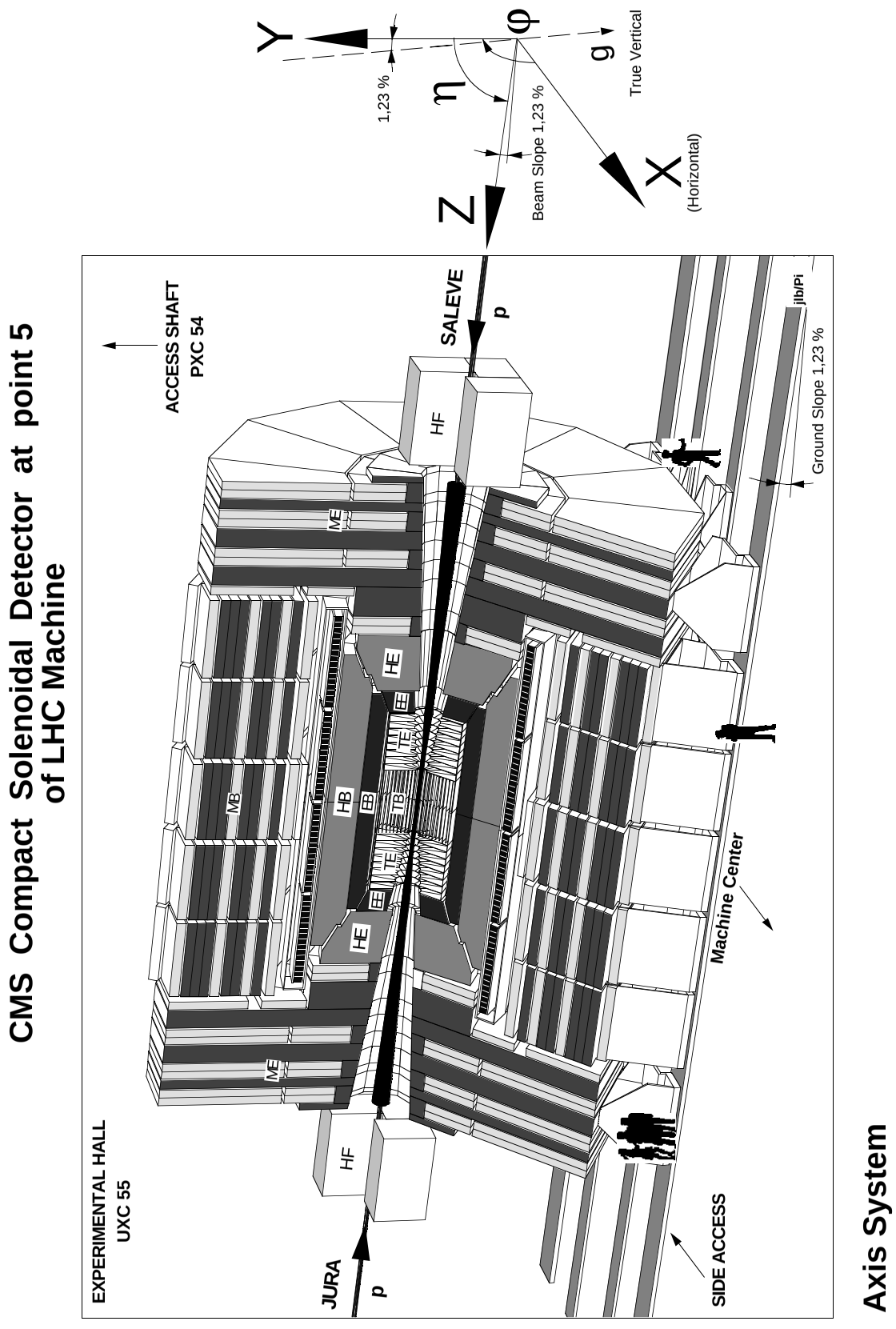

Fig. 1. 1: The CMS detector.

followed by the hadron calorimeter barrel (HB) and endcap (HE) as shown in Fig. 1.2. Both the barrel and endcap calorimeters experience the 4 Tesla field of the CMS solenoid and hence are necessarily fashioned out of non-magnetic material (copper alloy and stainless steel). The Central Hadron calorimeter is a sampling calorimeter: it consists of active material inserted between copper absorber plates. The absorber plates are 5cm thick in the barrel and 8cm thick in the endcap. The active elements of the entire central hadron calorimeter are 4mm thick plastic scintillator tiles read out using wavelength-shifting (WLS) plastic fibers.The barrel hadron calorimeter is about 79 cm deep, which at η=0 is 5.15 nuclear interaction lengths (λ) in thickness. This is somewhat thin, as is the transition region between barrel and endcap. To ensure adequate sampling depth for the entire $|\eta| < 3.0$ region the first muon absorber layer is instrumented with scintillator tiles to form an Outer Hadronic Calorimeter (HO). These layers are shown in red in Fig. 1.2.

The choice of crystals for the EM calorimeter, as well as the thinness of the barrel calorimetry, places severe constraints on the hadron calorimeter design and tempers its peformance. A certain amount of ingenuity is required to optimize the calorimeter resolution and response. Constant vigilance during the design stage is also required in order that all necessary cable and service paths are kept to an absolute minimum to minimize hadronic energy leakage or absorption by unsampled material. Accounting for all energy is essential for an optimal missing transverse energy measurement.

To extend the hermeticity of the central hadron calorimeter system to pseudorapidity (η) of five (as required for a good missing transverse energy measurement), CMS employs a separate forward calorimeter (HF) located 6m downstream of the HE endcaps. The HF calorimeter covers the region $3.0 < |\eta| < 5.0$. It uses quartz fibers as the active medium, embedded in a copper absorber matrix. The HF will be located in a very high radiation and a very high rate environment. Because of the quartz fiber active element, it is predominantly sensitive to Cerenkov light from neutral pions. This leads to its having the unique and desirable feature of a very localized response to hadronic showers.

1.1.3 The CMS baseline barrel calorimeter

The hadron calorimeter barrel is a sampling calorimeter with 5cm thick copper absorber plates. The innermost and outermost plates are 7cm thick and are made of stainless steel for structural strength. The CMS baseline for the hadron barrel calorimeter comprises 13 copper plates plus the 2 stainless steel plates for a total of 15 sampling plates and a sampling depth of about 79 cm (5.15 λ). There is good evidence that there may be adequate space inside the cryostat to increase the calorimeter depth by two additional copper plates by optimizing the use of space by the electromagnetic calorimeter and the tracker. If such space savings can be achieved, the hadron calorimeter could be increased in depth to 17 sampling plates for a sampling depth of about 89 cm (5.82 λ). Throughout this Technical Design Report it is assumed that the 5.82 λ barrel calorimeter configuration will be the final CMS configuration (this viewpoint was endorsed by the CMS Technical Board and Management Board in March of 1997). Since the optimization of space utilization for both the crystal calorimeter and the tracker is still in progress the final calorimeter layout will have to await the Crystal Calorimeter and Tracker TDR's. The performance of the hadron calorimeter for both the 5.15 λ inner barrel configuration and the 5.82 λ inner barrel configuration are discussed in the appropriate calorimeter performance sections of this report.

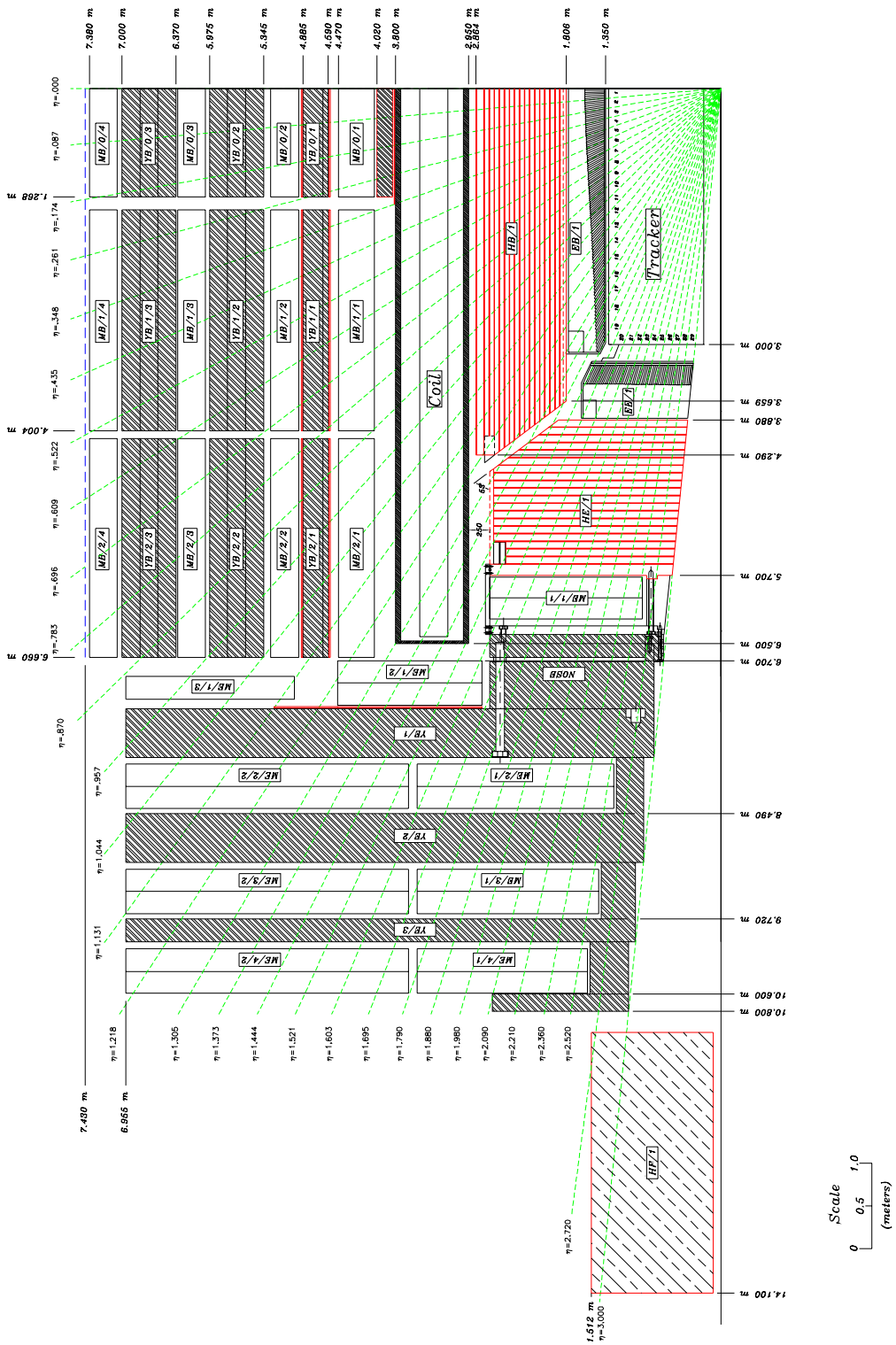

Fig. 1. 2 (see also C.S.): Section of CMS detector with HCAL shown in red.

1.1.4 The CMS forward calorimeter

The measurement of E_T^{miss} is essential for the study of top quark production and for Standard Model (SM) Higgs searches for $m_H \approx 80$ - 140 GeV and $m_H \geq 500$ GeV in the

$H \rightarrow WW \rightarrow l\nu jj$ channels. It is also important in SUSY Higgs searches for $A \rightarrow \tau\tau \rightarrow e\mu + E_T^{miss}$ and $A \rightarrow \tau\tau \rightarrow l^{\pm}h^{\pm} + E_T^{miss}$, allowing the A mass reconstruction.

Forward jet detection is critical in the search for a heavy Higgs boson ($m_H \approx 1$ TeV), with the decay $H \rightarrow WW \rightarrow l\nu jj$, $H \rightarrow ZZ \rightarrow lljj$, at high luminosity, 10^{34} $cm^{-2}s^{1}$. The production of the Higgs boson in this mass range through the WW or ZZ fusion mechanism is often characterised by two forward tagging jets. The jets are energetic ($<p_L> \approx 1$ TeV), with a transverse momentum of the order of m_W and they are produced in the pseudorapidity range $2.0 \leq |\eta| \leq 5.0$. The detection of these tagging jets is needed in order to suppress the large QCD W, Z + jets background.

It is essential to have the capability to recognise and veto jets at forward angles in the search for direct Drell-Yan (DY) slepton pair production or the associate direct DY chargino-neutralino production, leading to final states with two or three isolated leptons, no jets and E_t^{miss}. This is necessary to suppress the SUSY and SM backgrounds. With a coverage up to $|\eta| \approx 4.5$, vetoing events containing a forward jet of $E_T^{jet} \approx 25$ - 30 GeV will reject SUSY backgrounds by a factor 350 - 400 (SM background by a factor 9 - 10), with a 7% signal loss. In the case of slepton searches in two-lepton final states, the corresponding SUSY (SM) rejection factor, by veto on same type of forward jets, will be 30-50 (8 -10) with a loss in signal acceptance in the order of 10%.

In heavy ion collisions, the production rate of heavy vector mesons (Y, Y', Y'') as a function of the global energy density in nucleus-nucleus interactions, will be measured and the energy density can be estimated from the transverse energy flow measured in the calorimeters.

1.1.5 The luminosity monitor

The CMS luminosity monitor detector will consist of the forward quartz fiber calorimeter as well as Roman Pots 300-400 m upstream of the low beta insertion.

1.2 PHYSICS REQUIREMENTS

The Standard Model (SM) is a very successful description of the interactions of the components of matter at the smallest scales ($<10^{-18}$ m) and highest energies (~ 200 GeV) available. It is a quantum field theory which describes the interaction of spin-1/2, point-like fermions, whose interactions are mediated by spin-1 gauge bosons. The bosons arise when local gauge invariance is applied to the fermion fields, and are a manifestation of the symmetry group of the theory, which for the standard model is $SU(3) \times SU(2) \times U(1)$. The fundamental fermions are leptons and quarks. There are three generations of fermions, each identical except for mass. The origin of this generational structure, and the breaking of generational symmetry (i.e. the different masses of each generation) remains a mystery. Corresponding to the three generations, there are three leptons with electric charge –1, the electron (e), the muon (μ) and the tau (τ), and three electrically neutral leptons (the neutrinos ν_e, ν_μ and ν_T). Similarly there are three quarks with electric charge +2/3, up (u), charm (c) and top (t), and three with electric charge –1/3, down (d), strange (s) and bottom (b). There is mixing between the three generations of quarks, which in the SM is parametrized (but not explained) by the Cabibbo-Kobayashi-Maskawa (CKM) matrix.

The quarks are triplets of the SU(3) gauge group and so they carry an additional “charge”, referred to as color, which is responsible for their participating in the strong interaction (quantum chromodynamics or QCD). Eight vector gluons mediate this interaction; they carry

color charges themselves, and are thus self-interacting. This implies that the QCD coupling α_S is small for large momentum transfers but large for soft processes, and leads to the confinement of quarks inside color-neutral hadrons (like protons and neutrons). Attempting to free a quark produces a jet of hadrons through quark-antiquark pair production and gluon bremsstrahlung.

In the SM, the SU(2) × U(1) symmetry group, which describes the so-called Electroweak Interaction, is spontaneously broken through the existence of a (postulated) Higgs field with non-zero expectation value. This leads to the emergence of massive vector bosons, the $W^{\pm}$ and the Z, which mediate the weak interaction, while the photon of electromagnetism remains massless. One physical degree of freedom remains in the Higgs sector, which could be manifest most simply as a neutral scalar boson H^0, but which is presently unobserved.

The basics of the standard model were proposed in the 1960's and 1970's. Increasing experimental evidence of the correctness of the model accumulated through the 1970's and 1980's. Deep inelastic scattering experiments at SLAC showed the existence of point-like scattering centers inside nucleons, later identified with quarks. The c and b quarks were observed and neutral weak currents (Z exchange) were identified. Tet structure and three-jet final states (from gluon bremsstrahlung) were observed in e^+e^- and hadron-hadron collisions, and the W and Z were directly observed at the CERN SPS collider. Following these discoveries, the last decade has largely been an era of consolidation. Ever more precise experiments have been carried out at LEP and SLC which have provided verification of the couplings of quarks and leptons at the level of 1-loop radiative corrections — $O(10^{-3})$. The top quark was discovered at Fermilab in 1995, and is found to have an unexpectedly large mass (175 GeV). Only two particles from the Standard Model have yet to be observed: ν_T (whose existence is strongly inferred from Z decays) and the Higgs boson. The latter is most important as it holds the key to the generation of W, Z, quark and lepton masses.

The successes of the Standard Model have drawn increased attention to its limitations. In its simplest version, the SM has 19 parameters — three coupling constants, nine quark and lepton masses, the mass of the Z boson which sets the scale of the weak interaction, four CKM mixing parameters, and one (small) parameter describing the scale of CP violation in the strong interaction. The remaining parameter is associated with the mechanism responsible for the breakdown of the electroweak SU(2) × U(1) symmetry to U(1) of electromagnetism ("electroweak symmetry breaking" or EWSB). This can be taken as the mass of the Higgs boson the couplings of the Higgs are determined once its mass is given. Within the model we have no guidance on the expected mass of the Higgs boson. The current (June 1997) experimental lower bound from LEP2 is about 77 GeV, and the upper limit from global fits to electroweak parameters is about 470 GeV. As its mass increases, the self-couplings of the W and Z grow, and so the mass must be less than about 800 GeV, or the strong dynamics of WW and ZZ interactions will reveal new structure. It is this simple argument that sets the energy scale that must be reached to guarantee that an experiment will be able to provide information on the nature of electroweak symmetry breaking, which is the central goal of the Large Hadron Collider.

The presence of a single elementary scalar boson is distasteful to many theorists. If the theory is part of some more fundamental theory with a larger mass scale (such as the scale of grand unification, or the Planck scale) then radiative corrections will result in the Higgs mass being driven up to this large scale unless some delicate cancellations are engineered. There are two ways out of this problem which both result in new physics on the scale of 1 TeV. New strong dynamics could enter that provide the scale of the W mass or new particles could appear

which would cancel the divergences in the Higgs boson mass. In any of these eventualities — standard model, new dynamics or new particles — something must be discovered at the TeV scale, i.e. at the LHC.

Supersymmetry is an appealing concept for which there is at present no experimental evidence. It offers the only presently known mechanism for incorporating gravity into the quantum theory of particle interactions and provides an elegant cancellation mechanism for the divergences affecting the Higgs mass, while retaining all the successful predictions of the standard model and allowing a unification of the three couplings of the gauge interactions at a high scale. Supersymmetric models postulate the existence of superpartners for all the presently observed particles. There are bosonic superpartners of fermions (squarks and sleptons), and fermionic superpartners of bosons (gluinos and gauginos χ_i^0, $\chi_i^{\pm}$). There are also multiple Higgs bosons: h, H, A and $H^{\pm}$. There is thus a large spectrum of presently unobserved particles, whose exact masses, couplings and decay chains are calculable in the theory given certain parameters. Unfortunately these parameters are unknown; but if supersymmetry has anything to do with EWSB, the masses should be in the region 100 GeV – 1 TeV.

An example of the strong coupling scenario is "technicolor" models based on dynamical symmetry breaking. An elegant implementation of these ideas is lacking. Nonetheless, if the dynamics has anything to do with EWSB, we would expect new states in the region 100 GeV – 1 TeV. Most models predict a large spectrum. At the very least, there must be structure in the WW scattering amplitude at around 1 TeV center of mass energy.

There are also other possibilities for new physics that are not necessarily related to the scale of EWSB. There could be neutral or charged gauge bosons with masses larger than the Z or W. There could be new quarks, charged leptons or massive neutrinos or quarks and leptons might turn out not to be elementary objects. While we have no definite expectations for the masses of such particles, the LHC must be able to search for them over its entire available energy range.

The fundamental physics goal of the CMS detector is then to uncover and explore the physics behind electroweak symmetry breaking. This involves the following specific challenges:

a) Discover or exclude the Standard Model Higgs and/or the multiple Higgs bosons of supersymmetry;
b) Discover or exclude supersymmetry over the entire theoretically allowed mass range;
c) Discover or exclude new dynamics at the electroweak scale.

The energy range opened up by the LHC allows us to search for other, perhaps less well-motivated objects:

a) Discover or exclude any new electroweak gauge bosons with masses below several TeV;
b) Discover or exclude any new quarks or leptons that are kinematically accessible.

CMS will have the possibility of exploiting the enormous production rates for standard model processes for studies such as:

a) The production and decay properties of the top quark, and limits on possible exotic decays;
b) b-physics, particularly that of B-baryons and B_s mesons.

CMS must also have the capability to find the totally unexpected. We can be sure, though, that new phenomena of whatever type will decay into the particles of the standard model. In order to cover the list above, great flexibility is required. The varied physics signatures of these processes require that CMS be able to reconstruct and measure final states involving the

following:

a) charged leptons: electrons, muons and **taus**
b) **jets** coming from high-transverse momentum quarks and gluons
c) **jets** having b-quarks in them
d) **missing transverse energy** (E_T^{miss}) carried off by weakly interacting neutral particles such as neutrinos
e) the electroweak gauge bosons: photons, and Z and W bosons (in both their **dijet** and lepton plus **missing transverse energy** modes)

The CMS detector requires a hadron calorimeter to identify and measure the items noted in boldface above — jets, including those from b-quarks and taus, and missing transverse energy. In the design of CMS, considerable weight has been given to obtaining the best possible performance for muon identification and measurement and for the electromagnetic calorimetry (for photon and electron measurements). Our goal in designing the hadron calorimeter system is then to provide the best possible measurements of jets and missing transverse energy consistent with the chosen emphasis on muons and EM calorimetry, and to carry out an overall optimization of the detector so that the demands and performance of each subsystem match the physics goals of CMS.

In addition to the physics studies carried out with proton-antiproton collisions, CMS will search for the formation of quark - gluon plasma or other new physics in heavy ion collisions. Nuclei as heavy as lead will be collided in the LHC, and jets and muons will be used by CMS to probe the extremely high energy densities in the resulting nuclear matter. Hadronic calorimetry will again be central to such measurements.

1.3 THE CMS RADIATION ENVIRONMENT

1.3.1 Overview

The nominal luminosity of LHC, 10^{34} cm^{-2} s^{-1}, together with the 7 TeV beam energy, will create a very hostile radiation environment which all subdetectors will have to deal with. It has been known since the first LHC pre-studies, that the inner tracker and very forward calorimeters of LHC experiments will be confronted with unprecedented radiation levels. The endcap calorimeters and the muon spectrometer will also suffer from the environment. In CMS, due to the strong solenoidal field and the massive iron yoke, the barrel calorimetry and barrel muon spectrometry are the subsystems least affected by background and radiation damage effects.

We can distinguish three regions with quite different characteristics from the shielding point of view.

1. The main detector, up to $|\eta|$ = 3.0, where we have to deal with the pp-secondaries directly, but also with neutron albedo and hadronic punchthrough.
2. The region $|\eta|$ = 3.0-5.0 is covered by the HF. Cascades developing here affect the HF itself and its electronics, but any leakage would be of concern for the close by endcap muon system also.
3. At pseudorapidities beyond the acceptance of the HF comes the collimator, which protects the superconducting quadrupoles. Cascading in this region is the dominant source of radiation background in the experimental cavern outside of the detector.

Particles with $|\eta| > 7.9$ will not be captured in the experimental area.

1.3.2 Radiation damage

The hostile radiation environment implies that a lot of attention has to be devoted to selecting sufficiently radiation hard technologies. A significant part of LHC related R&D work has in fact concentrated on radiation hardness studies of detectors and electronics.

Silicon devices will be used in essentially all parts of CMS, either as electronic chips, as charged particle detectors or as photodiodes.

Similar dose-related damage effects have been reported for organic and inorganic scintillators, i.e. the $PbWO_4$ crystals of the CMS electromagnetic calorimeter and the plastic scintillators of the CMS central hadron calorimeter. In these cases the light transmission degrades due to the generation of color centers by the ionization (i.e. the plastic becomes less transparent). Thus the degradation of scintillators is also a function of the radiation dose.

Although in most cases significant annealing is observed, some fraction of the damage is never recovered and the detectors continuously degrade with increasing fluence or dose. The annealing effects make radiation damage a complicated function of both time and fluence. For instance, the calibration of a calorimeter might change due to both degradation during irradiation and simultaneous improvement due to annealing. If the annealing is very fast the calorimeter response can become luminosity dependent.

1.3.3 Induced radioactivity

While induced radioactivity is negligible at electron-positron colliders, it will be a major concern at LHC. We can assume that each inelastic hadronic interaction results in a residual nucleus, which can be almost anything below the target mass and charge. This residual can directly end up being stable, but more probably it will be radioactive.

Only some 30% of the interactions lead to formation of long-lived radionuclides, which we would really see as induced activity when entering the area. But this activity decreases relatively slowly after the end of irradiation, so that even long cooling times do not significantly improve the situation. A rough rule of thumb is that the effective half life of the remaining radioactivity is equal to the time which has elapsed after the end of irradiation.

1.3.4 Shielding requirements and materials

Inside of CMS shielding is dictated by the very limited space available. Therefore materials have been selected to provide the most efficient shielding in the smallest amount of space. An equally strong constraint on the choice of shielding strategy arises from the fact that the performance of the detectors cannot be compromised.

Outside the detector, around and beyond the HF, the constraints come mainly from cost and weight, although space restrictions have to be also taken into account for the HF shielding.

At LHC we are confronted with a radiation environment which includes essentially all types of particles. The energy distribution ranges from thermal neutrons up to the typical hadron energy around 1 GeV and ends in a high energy tail which extends to few TeV. This heterogeneous radiation environment implies that no shielding material alone will be the perfect one.

1.3.5 Minimum bias events

The radiation environment simulations are based on minimum bias events obtained from

the DPMJET-II event generator[2]. DPMJET-II is the most recent of the Dual Parton Model generators, which are specially suited for simulation of minimum bias hadronic collisions. As one of the updates with respect to the best-known of its predecessors, the DTUJET93 generator[3], DPMJET-II includes a complete description of charm production.

1.3.6 Radiation transport codes

The radiation simulations are independent of the general detector performance simulations and are performed using simulation packages specially designed for radiation physics. FLUKA[4] is the baseline code for the radiation environment simulations of CMS, but MARS and GCALOR are also used for various dedicated studies.

Although FLUKA does not provide a user friendly geometry interface like GCALOR and is therefore not compatible with CMSIM, its use is motivated by more accurate and up-to-date physics models and the indispensable variance reduction possibilities.

1.3.7 Barrel and endcap calorimeter

Fig. 1. 3 gives an overview of hadron (E>100 keV) fluence and radiation dose in the CMS HB/HE region. At the end of the HE we can see some radiation streaming in the 3.44 cm wide gap, which is caused only by the approximate geometry. This gap is not present in reality and we can see that at large radii it leads to slight overestimation of neutron fluence.

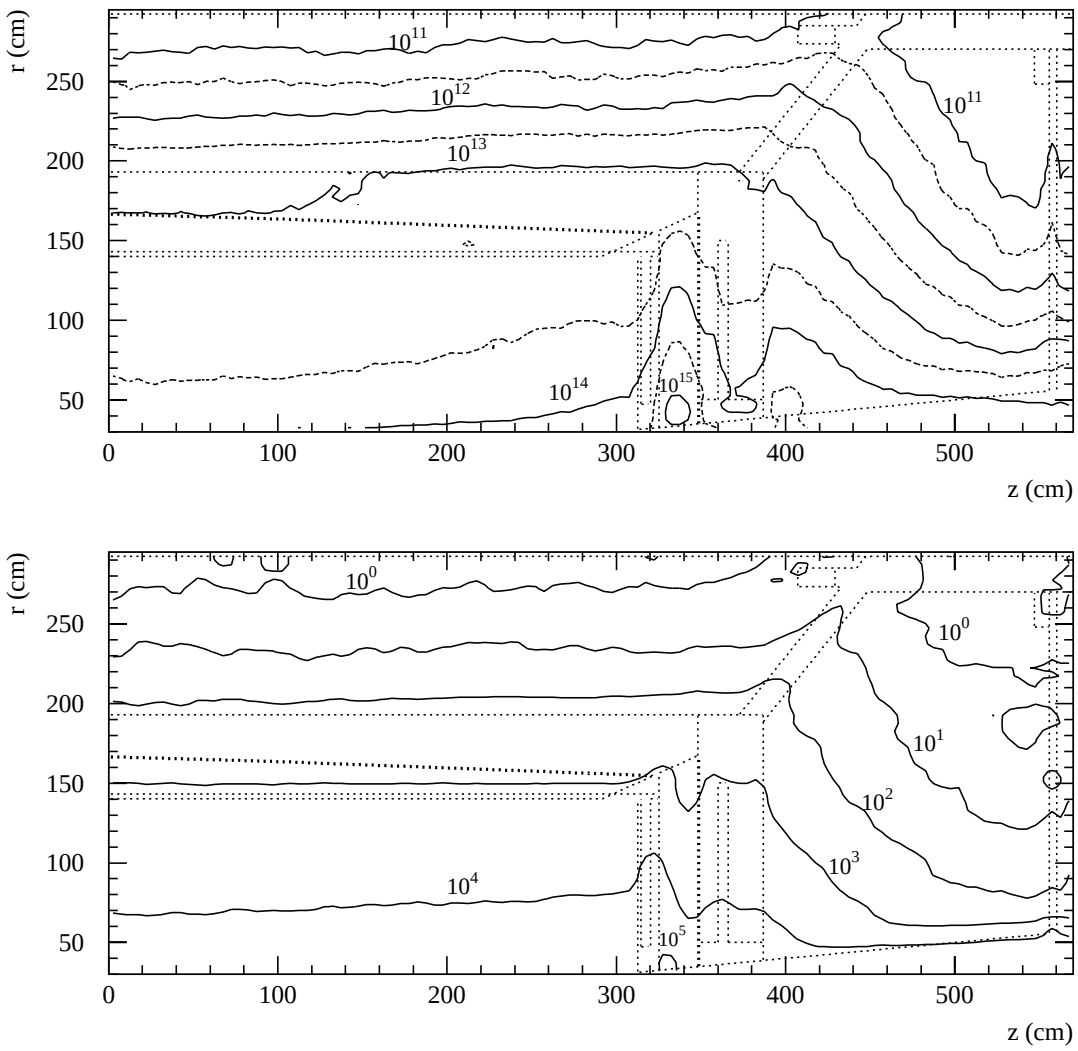

Fig. 1. 3: Fluence of hadrons (E>100 keV) in $cm^{-2}s^{-1}$ (upper plot) and radiation dose in Gy (lower plot) in the HB/HE region. The dose values have been smoothed by taking weighted running averages over neighbouring bins. Values are given for 5×10^5 pb^{-1}. The intermediate (dashed) contours in the fluence plot correspond to 3.16×10^n. The dotted lines indicate the geometry.

While Fig. 1. 3 is based on data obtained with a binning which is much coarser than the internal structure of the calorimeter, Fig. 1. 4 shows the dose in the HE for some fixed radii with a binning fitted to the internal structure. The alternation of absorber and scintillator layers in the HE becomes visible as a strong variation of the dose. This clearly indicates that a dose calculated in average material would underestimate the critical parameter, which is the dose in the plastic scintillators. Because most of the dose increase is due to recoil protons induced by low energy neutrons, simple corrections based on the variation of dE/dx cannot correct for the effect.

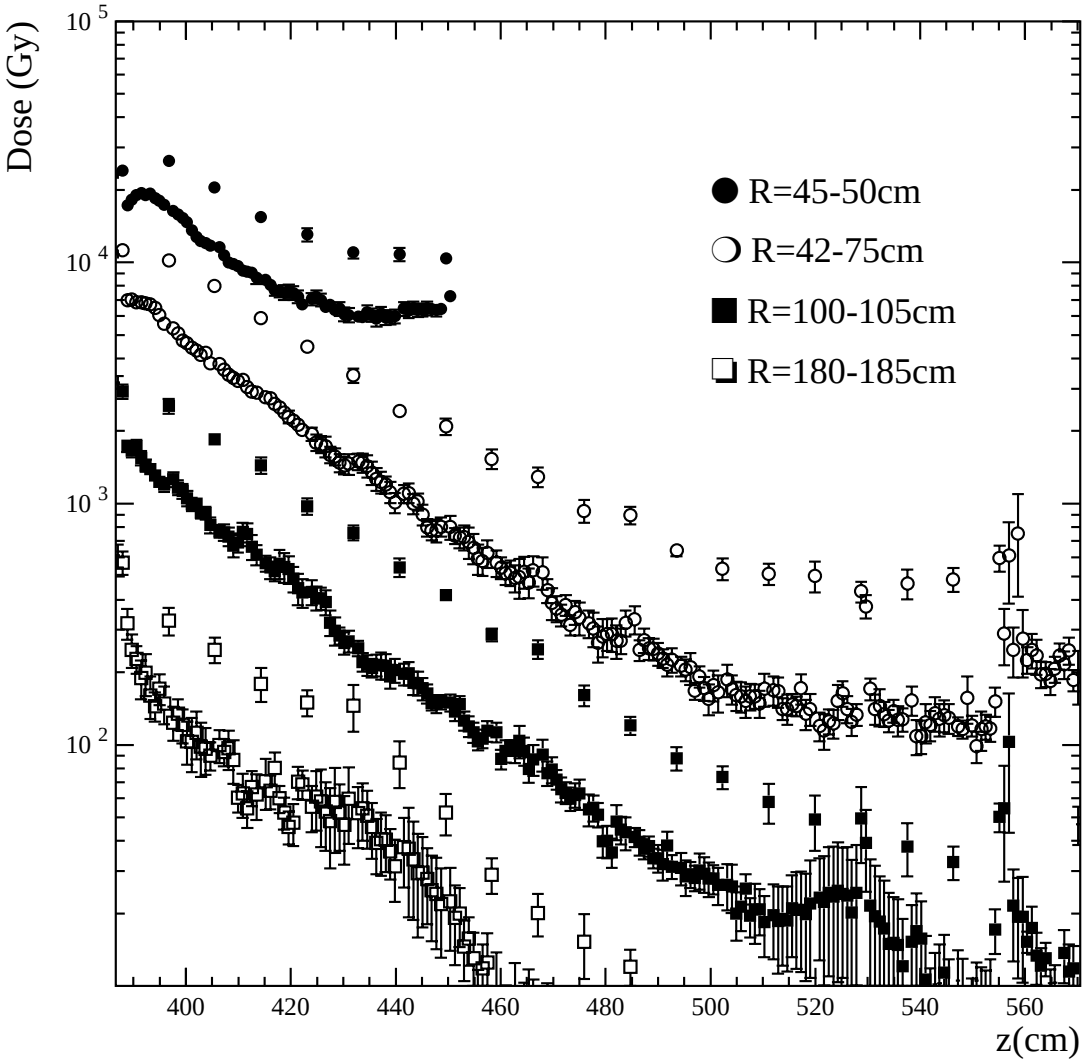

Fig. 1.4: Radiation dose for 5×10^5 pb^{-1} at fixed radii in the endcap HCAL. The error bars indicate only the statistical error of the simulations. The points with higher dose correspond to energy deposition in the scintillator layers.

In Fig. 1. 4 the effect of the calorimeter boundary at $|\eta|=3$ becomes significant at the smallest radii. The increase of dose as a function of depth is due to the particles entering the calorimeter from its $|\eta|=3$ boundary. At the end of the HE the dose increase is caused by the slot for the muon station ME1/1 and the crack left in the simulation model between the HE and the stainless steel back plate.

1.3.8 Forward calorimeter

HF is exposed to the most intense radiation of all CMS subdetectors. This is best seen if we consider that on average 760 GeV per event are incident on the two forward calorimeters, compared to only 100 GeV for the whole main detector. In addition, this energy is not uniformly distributed, but has a pronounced maximum at the highest rapidities.

The quartz fibres themselves can sustain significant radiation doses and hadron fluences. The hadron fluence and dose profiles in the HF are shown in Fig. 1.5. The lower energy cut for plotting the hadron fluence, including neutrons, is 100 keV.

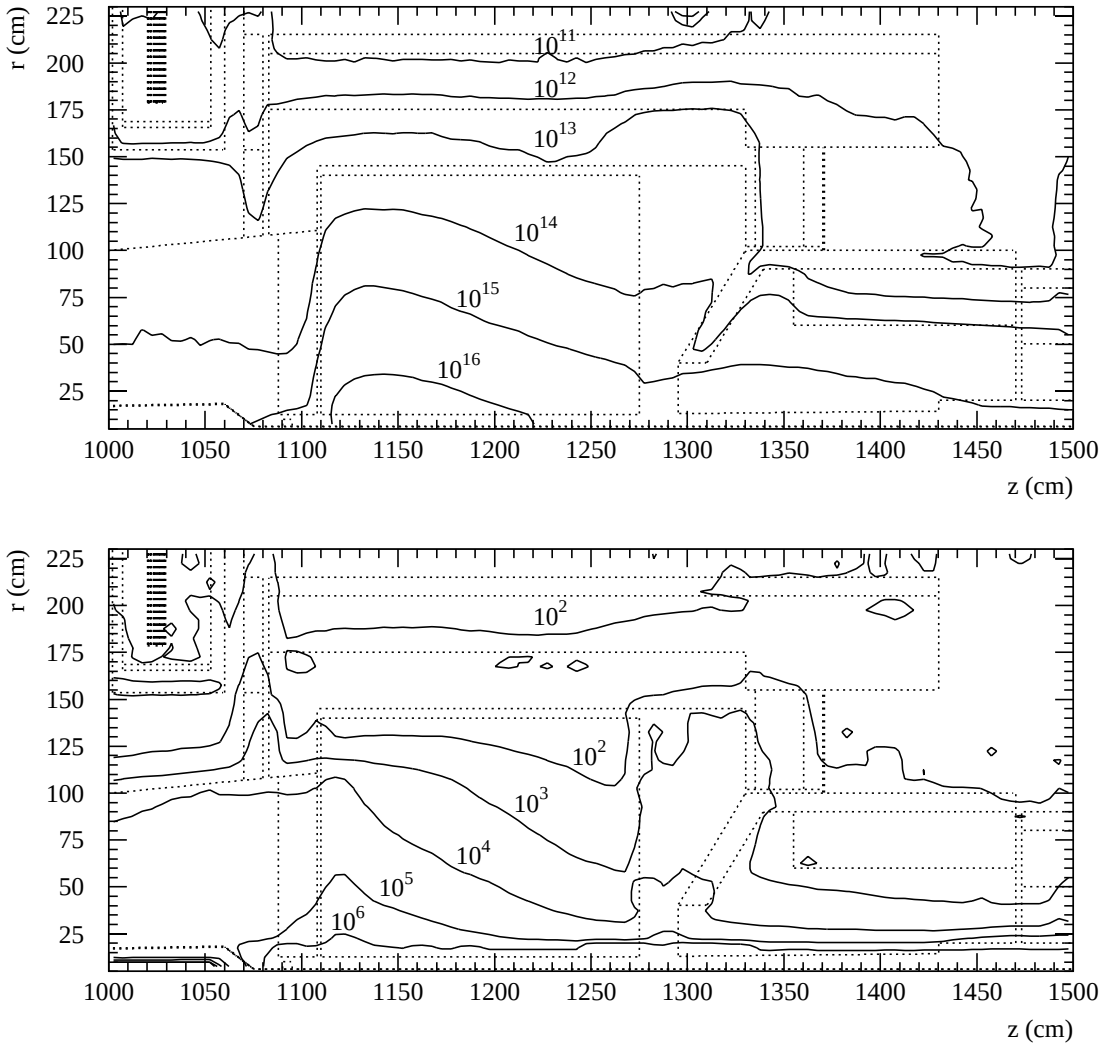

Fig. 1. 5: Fluence of hadrons (E>100 keV) in $cm^{-2}\ s^{-1}$ (upper plot) and radiation dose in Gy (lower plot) in the HF and its surroundings. The dose plot has been smoothed by taking running averages of the values, which slightly masks the dependence of dose on geometry details. Values are given for $5 \times 10^5\ pb^{-1}$.

We can see from Fig. 1.5 that the shielding quite efficiently suppresses the hadron flux, and in particular the optimized interface between the endcap and the HF provides good shielding for the ME4 muon station. The polyethylene/iron layer around the back shielding plug protects the HF photomultipliers. The endplug efficiently suppresses both the dose and the neutron flux at the back of the calorimeter and smoothly joins with the rotating shielding. The shielding around the HF is most important for ME4. We can see that it suppresses neutron fluence and dose below the overall levels in the experimental area.

1.3.9 Radiation levels in scintillators

In Table 1. 1 the dose in the HE scintillators is collected along lines of constant rapidity. The raw data is obtained from equidistant radial bins and the values have been linearly interpolated between two bins. Corresponding data for the HB is shown in

Table 1. 2. It has to be emphasized that the statistical significance of the given dose values

in the outermost corner if the HE, around $|\eta|$=1.5, is relatively poor.

We observe an increase of dose in the last scintillator layer. This is mostly due to the close-by slot for the endcap muon station ME1/1. The maximum dose at η=2.8 is 26 kGy. Going even further up in pseudorapidity, the absolute dose maximum of 37 kGy is found in the second scintillator layer of the HE (after first absorber plate) at a radius of 40-45 cm.

Table 1. 1

Radiation dose (Gy) in the scintillators of the HE for an integrated luminosity of $5 \times 10^5\,\mathrm{pb}^{-1}$.

z (cm)	η=1.5	η=2.0	η=2.8
388	570	3800	24000

Table 1. 2

Radiation dose (Gy) in the scintillators of the HB for an integrated luminosity of $5 = 10^5\,\mathrm{pb}^{-1}$.

Radius (cm)	η=0.1	η=0.6	η=1.1
198	190	250	300

The general "rule of thumb" that in hydrogen-containing regions of CMS the 100 keV threshold roughly splits the total neutron fluence in half, is supported by these HCAL fluences.

Activation and associated photon production are mainly low-energy phenomena, usually occurring only in the thermal regime. It should be understood that the actual thermal neutron fluence is only a small fraction of the difference between the total and the >100 keV fluence. In most parts of the HCAL the thermal neutron fluence is less than one percent of the total. But it should be noted that this low fluence is mostly due to the relatively small range of thermal neutrons in the HCAL material.

1.3.10 Radiation levels in HPD boxes

The HPD boxes were included explicitly in the simulation, although modeled as an annular ring in order to preserve the cylindrical symmetry. Their average density was assumed to be 2.4 $\mathrm{g/cm}^3$. The composition was assumed to be a copper/plastic mixture. The energy spectrum for the HB boxes for photons and neutrons is shown in Fig. 1.6. Table 1. 3 shows the particle fluences and radiation dose in the barrel and endcap HPD boxes.

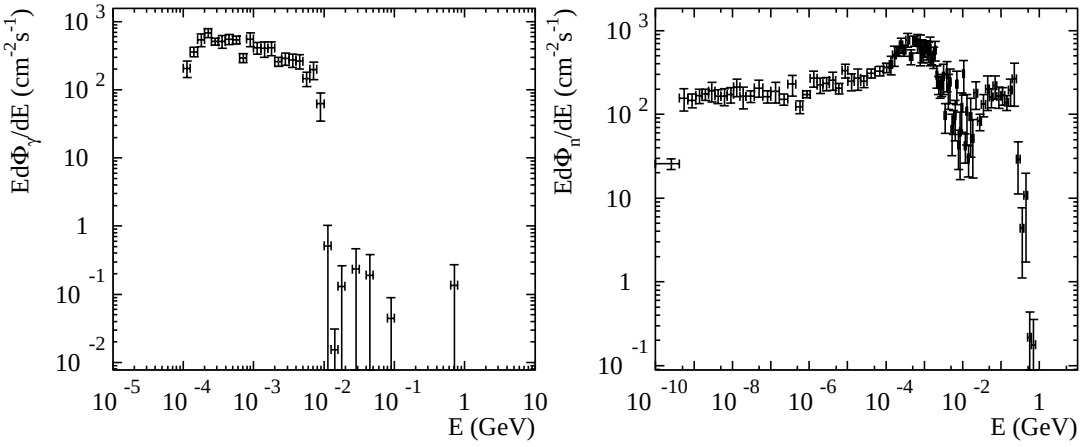

Fig. 1. 6 : Energy spectra of photons and neutrons in the barrel HPD box. Values are for LHC peak luminosity.

Table 1. 3

Particle fluence and dose in the HPD boxes. The hadron fluence is mainly neutrons above 100 keV and is the proper quantity for estimating silicon bulk damage. All fluences are given in 10^{10} cm^{-2} and the dose in Gy. All values are for $5 \times 10^5\, pb^{-1}$.

	Barrel	Endcap
Total neutron fluence	28	7
Hadron fluence	13	2
Photon fluence	9	2
Dose	1.6	0.2

1.4 THE CMS HADRON CALORIMETER DESIGN SUMMARY

1.4.1 Requirements and design constraints

Requirements

The design of the hadron calorimeter requires good hermiticity, good transverse granularity, moderate energy resolution and sufficient depth for hadron shower containment. We have chosen a lateral granularity of $\Delta\eta \times \Delta\phi = 0.087$ for $|\eta| < 2.0$ to match the electromagnetic calorimeter and the muon chamber structure. This granularity is sufficient for good dijet separation and mass resolution. The calorimeter readout must have a dynamic range from 5 Mev to 3 TeV to allow the observation of single muons in a calorimeter tower for calibration and trigger redundancy purposes as well as measure the highest possible particle jet energies that might arise in the search for new phenomena.

The physics program most demanding of good hadronic resolution and segmentation is the detection of narrow states decaying into pair of jets. The dijet mass resolution receives contributions from physics effects such as fragmentation and initial and final state radiation, as well as detector effects such as angular and energy resolution. When the jet p_T is small, mass resolution is dominated by physics effects. High p_T jets may arise from either the decays of boosted light objects or from decays of heavy objects. For the boosted case, angular resolution plays a more important role than energy resolution. Only in the case of back to back high p_T jets

arising from the decay of heavy objects are the physics and angular effects suppressed to the point where energy resolution plays a significant role.The influence of hadron calorimeter transverse segmentation has been studied for hadronic decays of boosted W's and Z's. Segmentation coarser than $\Delta\eta \times \Delta\phi = 0.1 \times 0.1$ significantly degrades the mass resolution, particularly for W/Z p_T > 500 GeV/c, while the energy resolution has relatively little effect.

Test beam studies of the CMS calorimeter layout (including ECAL) indicate $\sigma_E / E = 100\% / \sqrt{E} \oplus 4.5\%$ is achievable between 30 GeV/c and 1 TeV. Detailed simulations of the cracks, dead material, etc of the calorimeter system have been made to obtain energy and missing E_T resolution as a function of η and ϕ.

The HF jet energy resolution and missing transverse energy resolution is well matched to that of the central calorimeter, as has been confirmed by test beam measurements and simulation studies.

Design constraints

The central calorimeters are located inside the CMS solenoid and cryostat. The 4 Tesla field permeates the entire calorimeter structure. The calorimeter support structure must be able to withstand the magnetic forces generated in the unlikely case of a quench of the superconducting solenoid magnet. The response of scintillator to charged particles in high magnetic fields has been measured and understood.

The 25ns time interval between beam crossings sets the scale for the time resolution needed in the calorimeter. The overall event rate of approximately 20 "minimum bias" intractions per crossing at LHC design luminosity sets the scale for unwanted backgrounds. The calorimeter must help distinguish the rare interesting events from this background and must have the granularity and time resolution to suppress multi-event pile up.

The radial depth of the barrel hadron calorimeter is restricted by the inner radius of the solenoid cryostat which limits its thickness to about 100cm. To maximize the number of hadronic intraction lengths in the barrel, a copper alloy is chosen as the absorber material.

1.4.2 The central hadron calorimeter design (HB/HE/HO)

Globally, the hadron calorimeter can be considered in two pieces: (a) a central calorimeter $(|\eta| < 3.0)$ in which we require excellent jet identification and moderate single particle and jet resolution; and, (b) a forward/backward calorimeter $(3.0 < |\eta| < 5.0)$ with modest hadron energy resolution but with good jet identification capability. The forward calorimeter is physically separated from the central calorimeter, its front face being located at ±11m from the interaction point.

The Central Calorimeter consists of the Hadron Barrel (HB) and Hadron Endcap (HE) calorimeters, both located inside the CMS magnet cryostat. An Outer Calorimeter (HO) is required in the barrel and endcap region to measure late shower development and ensure of total shower energy containment.

Structure

The central calorimeter is divided into a central barrel and two endcap calorimeter sections. The central barrel is divided into two half sections, each half section being inserted from either end of the barrel cryostat of the superconducting solenoid hung from rails in the median plane. Because the barrel calorimeter is very rigid compared to the cryostat, a special

Belleville washer (spring) mounting system is used to ensure that the barrel load is distributed evenly along the rails.

A half barrel consists of 18 identical wedges, constructed out of flat absorber plates parallel to the beam axis. The body of the calorimeter is copper but the inner and outer plates are stainless steel. The endcap hadron calorimeter has the same 18 fold segmentation in ϕ. The copper plates are bolted together in a staggered gap/absorber structure to ensure that the calorimeter geometric layout contains no projective dead material for the full radial extent of a wedge. To allow the stacking of such plates without major tolerance build-up, they must be machined to better than 0.3mm in flatness over the entire length of the plate.

To maximize shower energy resolution (after the crystal ECAL) the inner barrel hadron calorimeter is segmented radially (in depth) into two different sampling hadron compartments (HB1 and HB2). There is an initial layer of sampling immediately following the ECAL electronics, and 17 layers of sampling ganged together into a single tower readout. Such an unusual distribution of sampling layers is the result of a response ratio e/h>2 induced by the crystal ECAL for the combined ECAL/HCAL system. The Outer Calorimeter with 2 coarse sampling layers is essential for full containment of hadron showers. Thus there are a total of 19 sampling layers in the barrel, except at $\eta = 0$ where an additional absorber plate is inserted and sampled immediately outside of the magnet cryostat. All active readout scintillator tiles in each layer are divided into segments $\Delta\eta \times \Delta\phi = 0.087 \times 0.087$. This granularity gives good shower resolution and matches the trigger granularity of the electromagnetic calorimeter and of the muon system.

The two layers of scintillator of the Outer Calorimeter are divided into the same granularity of $\Delta\eta \times \Delta\phi = 0.087 \times 0.087$ as the barrel and envelop the entire first layer of the CMS muon iron absorber. This double layer of scintillator has an individual readout for each $\Delta\eta \times \Delta\phi$ segment (HB3). To wrap around the absorber effectively this scintillator double layer has a 12-fold symmetry to match that of the iron absorber. In the region $(0 < |\eta| < 0.4)$ an additional 15cm of steel are placed in front of the muon chambers. In this region The Outer Calorimeter consists of 3 sampling layers, since we must place a sampling layer immediately after the coil and before this additional absorber plate.

The Endcap Calorimeter (HE) is of monolithic construction, consisting of staggered copper plates bolted together into 10 degree sectors. The innermost and outermost plates along the beam direction are made of stainless steel for strength. Each monolith weighs about 300 tonnes. The HE outer radial perimeter is polygonal, corresponding to the 18 fold wedge structure of the barrel. The plates are bolted and then colleted against shear forces, layer by layer. Fig. 1.7 illustrates this structure. When completely assembled, the Endcap Calorimeter module is mounted onto its corresponding muon endcap. The scintillator trays are inserted before mounting.

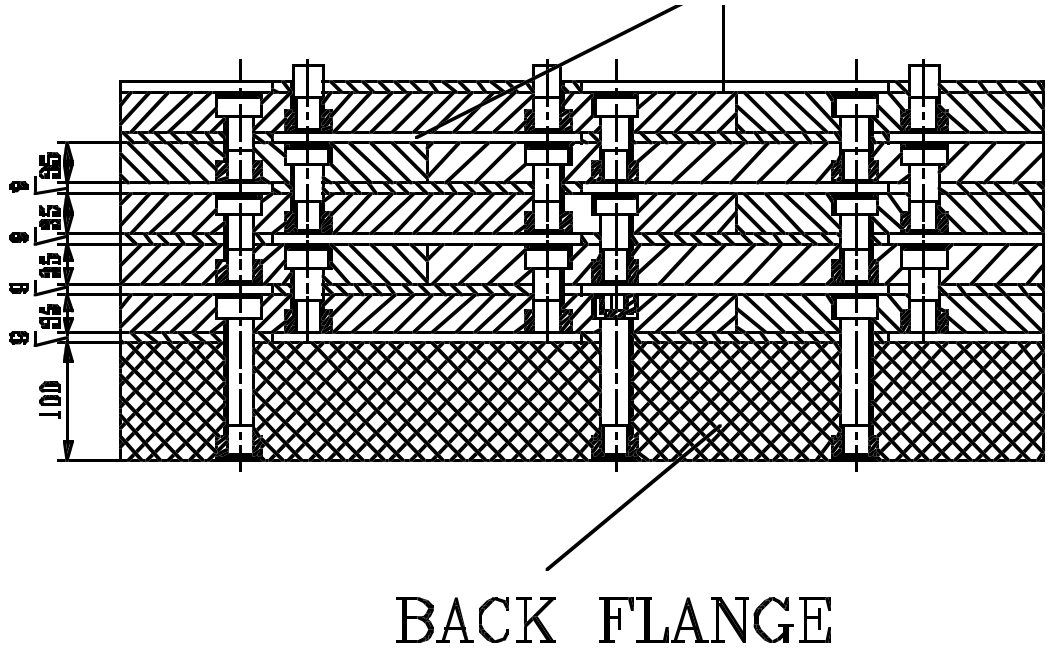

Fig. 1.7: Bolted structure of the HE.

The endcap hadron calorimeter is also segmented in depth into two different sampling compartments (HE1 and HE2) with 80mm copper absorber thickness. Generally, there again is an initial sampling layer, followed by 18 layers ganged together into a single tower. However, the Endcap calorimeter has two special regions. The region at high eta, ($2 < |\eta| < 3$), is a moderately high radiation area. To be able to re-weight the shower profile response as the scintillator response decreases as a result of radiation damage, the HE is divided into three readout sections (HE1, HE2 and HE3) consiting of (1 + 4 + 14) sampling layers. In a later discussion in this chapter we present a detailed discussion of how the HE can tolerate a certain amount of radiation damage by reweighting the scintillator response. Similarly the cable/service gap contains at least 10cm of non-uniformly distributed material, giving a non-uniform response; again, subdividing the readout into three enables one to reconsruct the shower profiles in the two towers shadowed by the cable/service gap and thus better estimate the energy lost in the material in the gap.

In the endcap region, the Outer Calorimeter has only a single sampling layers. It is essential in the barrel/endcap transition region ($1.3 < |\eta| < 1.5$) for full containment of hadron showers. It is embedded behind the first layer of muon chambers and is an integral part of the muon system. Thus there may be a total of 20 sampling layers in the barrel/endcap transition region. All active readout scintillator tiles in each layer are divided into segments of $\Delta\eta \times \Delta\phi = 0.087 \times 0.087$ as in the barrel (except at the highest η region where the η segmentation is made to match the granularity of the crystal calorimeter. This granularity gives good shower resolution and matches the overall trigger granularity of the electromagnetic calorimeter and of the muon system.

The effective barrel absorber thickness increases as the polar angle varies as $1/\sin\theta$. The barrel HCAL absorber thickness varies from 5.15λ at $|\eta| = 0$ to 9.1λ at $|\eta| = 1.3$. It follows that the stochastic resolution term in the barrel due to sampling depends only on the physically relevant variable $E_T = E \sin\theta$. A smooth transition is made to the endcap region at $|\eta| = 1.5$. However, two η segments in this region are traversed by a 100mm gap to provide cable and

fiber paths to the outer detector. The total absorber thickness in the endcap averages about 10.5λ, to allow for the logarithmic increase in depth needed for the higher energy shower containment at fixed E_T. The electromagnetic calorimeter in front of HB/HE adds about 1.1 λ of absorber.

Manufacture, shipping, assembly and installation

To facilitate construction, shipping, assembly and installation the barrel is divided into two halves, each half consisting of 18 identical wedge modules (weighing 27 tonnes each), for a total of 36 identical barrel modules. The absorber modules will be constructed at a site remote from CERN. Each half barrel will be pre-assembled at the manufacturing site to ensure its stacking tolerances. The half-barrel will then be disassembled and each individual wedge module will be shipped to CERN and equipped with scintillator trays in CERN Building 168. The final assembly will be in a horizontal orientation on a structural cradle that will also serve as lowering and installation fixture for each half barrel.

The outer CMS muon detector is divided into 5 barrel sections and 2 endcap sections. The central barrel section supports the solenoid and its cryostat vessel. The cryostat vessel in turn supports all barrel detectors that are mounted inside it (calorimeters and trackers). The remaining four barrel sections consist of the muon iron and the barrel muon chambers. The two CMS endcap sections support all of the endcap detectors (calorimeters, and the endcap muon system). The forward calorimeter is mounted independently.

The barrel hadron calorimeter halves are supported on rails attached to the inside of the cryostat vessel. This rail system is parallel to the beam axis and divides the cryostat vessel into two equal longitudinal sections (the upper section of the calorimeter pressing down on the rail, while the lower part hanging down from it). The barrel electromagnetic calorimeter sits on rails mounted on the lower segments of the barrel calorimeter, while the endcap electromagnetic calorimeter is mounted on the front face of its corresponding hadron endcap. The central tracking system, in turn, is mounted on rails attached to lower regions of the barrel em calorimeter.

Each HCAL half barrel will be transferred from its cradle to its resting position on the rails by pulling on a cable system anchored to the corresponding far end of the cryostat. The entire HB will be inserted into the cryostat for surveying in the surface hall, then removed and lowered into the experimental hall for re-insertion into the cryostat.

1.4.3 The central calorimeter optical system

The hadron calorimeter will consist of a large number of towers (~4300). In the barrel, inside the coil each tower will have 17 layers of scintillator tiles grouped into 2 samplings in depth. Outside the coil cryostat an additional two sampling layers of scintillator will be installed (HB3) around the muon absorber.

In order to limit the number of individual elements, the tiles in a given layer constitute a single mechanical unit called a “megatile”. The eta-phi segmentation in the Barrel region $16(\eta)\times 1(\phi)$ and $16(\eta)\times 2(\phi)$ to match the staggered copper absorber structure of each barrel wedge. These 16 tiles or 32 tiles in one “megatile” layer of a wedge are organized into a single mechanical unit. The separate tiles are cut out of scintillator, the edges painted white, and the tiles are then attached to a plastic substrate with plastic rivets. The light from each tile is collected by a green Wave Length Shifting (WLS) fiber that is placed in a machined groove in the scintillator. After exiting the scintillator the WLS fiber is immediately spliced to a clear fiber

that transports the light to the edge of the megatile. The clear fiber terminates into a multi-fiber optical connector at the megatile boundary. Multi-fiber optical cables carry the light from the megatiles to decoder matrix boxes where the fibers from the different layers comprising a η-φ depth segment are reorganized into towers, and the light from all the tiles making up a tower is optically mixed and sent to an optical transducer. The megatile along with the readout fibers will be packaged into scintillator trays (called "pizza pans") which will be inserted into the calorimeter absorber structure.

The advantage of this scheme is that the scintillator trays can be built and tested remotely from the installation area. Before the calorimeter absorber is lowered into the CMS pit and installed into the solenoid, the trays are rapidly inserted. Another advantage of the tray scheme is that in the unlikely event of catastrophic radiation damage to the scintillator, the trays can be removed and refurbished without removal of the absorber structure. Once in the experimental hall, optical fibers are connected between trays and the photodetectors.

A scintillator tray unit begins with a plastic cover plate of a thickness of 0.5 mm followed by the 4mm scintillator megatile wrapped in thin sheet of Tyvek 1073D (a plastic insulating material) for reflectivity and light tightness. The tiles are grooved to hold the WLS fibers. The top of the megatile is covered with 2mm white polystyrene. This plastic cover is grooved to provide routing for the fibers to the outside of the tray. The fibers rise out of the scintillator into the grooves on top of the white plastic. The white plastic layer is also grooved to accept tubes for the moving radioactive source.

Choice of materials

We require the materials used in the CMS HCAL optical system to have a number of properties. The materials should have good long-term stability, be non-demanding in handling, and easy to machine. They should be able to survive the expected maximum radiation doses up to $|\eta| = 3.0$ (a total of ~ 0.2 Mrad in the barrel, 4 Mrad in the endcap) without the necessity of replacement. The total optical system should produce enough light to easily identify minimum-ionizing tracks penetrating the calorimeter (for use in muon identification as well as calibration/monitoring). Well controlled thickness (of the scintillator) and diameters (of the fibers) are critical to the optimal performance of the calorimeter. Attenuation lengths of the fibers also must be well-controlled.

Our baseline choice of material for the HCAL optical system satisfies these requirements. For the barrel, we will use Kuraray SCSN81 scintillator plastic. This material has been shown to be moderately radiation hard and have good long-term stability. For the WLS fiber, the baseline choice is Kuraray Y-11 double-clad fiber. The double cladding generates good mechanical properties as well as yielding ~ 1.5 times more light. The baseline clear fiber is Kuraray double-clad fiber.

It is well documented that the light yield from scintillator increases when embedded in a magnetic field [5]. Measurements at Fermilab and Florida State indicate that this effect saturates above 2T [6] for SCSN81 scintillator. This intrinsic brightening of scintillator in a magnetic field was confirmed in our 1996 test beam studies.

In addition to this intrinsic scintillator brightening, the CMS 4 Tesla field creates a geometric path length effect for soft electrons if the magnetic field is parallel to the absorber plates (barrel configuration). This increase in path length for soft electrons leads to an additional increase in the scintillator response by as much as 20% for electrons and about 10% for pions.

This effect is well understood and is well simulated by Monte Carlo description of electron showers in high magnetic fields. By studying such simulations we have learned how to reduce such effects for hadrons to the 4% level. This effect is not tracked by any of our monitoring schemes and has to be determined by Monte Carlo calculations and controlled by our manufacturing procedures.

Production issues

To realize the tile/fiber technology, several developments were required. These developments, largely due to the CDF and SDC groups, include fiber splicing, mirroring, optical connectors and cables, and fundamental measurements of the tile-fiber optical system. Some of the results are discussed below.

Fibers are spliced together by controlled melting of the ends inside a restricting tube (thermal fusion). This technique has been optimized for factors such as long-term mechanical stability, strength to withstand repeated flexing, high optical transmission and very small variation in transmission for different splices. The mean value of the transmission through a splice (normalized to the uncut fiber) is measured to 91% with an r.m.s. of 1.8%.

Multi-fiber optical connectors were developed by the CDF collaboration. These connectors allow the optical signals to be treated similarly to electrical signals. The scintillator tile trays can be quickly connected and disconnected to multi-fiber optical cables that look strikingly like multi-conductor electrical cables. The optical connectors are made by precision injection molding of mechanically stable plastic. In this manner, all connectors are identical, and there is no need for pair-matching of the connectors. The reproducibility of the optical connector transmission for many make/break operations has been measured to be 0.6% with a mean transmission of 83% for a single fiber, and an overall variation of ~ 2 to 3 % for all fibers in the connector.

Variation in transverse uniformity of tiles in a tower or variation in tile-to-tile light yield for tiles in a tower will generate a contribution to the constant term in the calorimeter resolution. We have carried out detailed studies to identify the requirements on the optical system so that these variations do not contribute substantially to the constant term. We found that tile-to-tile variation of less than 10% is acceptable (see chapter 6). The CDF plug upgrade calorimeter group has built several thousand tiles. The measured finished tile to tile variation of the light yield from a set of over 16,000 of these tiles is found[7] to be 6.5%. This is adequate for a good hadron calorimeter.

The transverse uniformity of a tile is dominated by the placement of the WLS fiber. Based on knowledge from the CDF group, we expect our transverse non-uniformity to be a few per cent. This non-uniformity will not appreciably affect the resolution constant term.

Quality control

The scintillator trays will be built and tested remotely. The trays, optical cables, and decoder boxes will be shipped to CERN. There they will be installed in each individual wedge in Building 168. At this time, we must verify that all cables are correctly placed, good optical contacts are made, and that there are no broken or damaged components. We will determine this by using an integrated system of moving radioactive sources. This system allows a radioactive source to illuminate each tile in the system individually. By comparing the induced current to that expected, we can verify the integrity of the system.

The moving source system was developed for the CDF and SDC calorimeter projects. It

consists of a set of tubes placed in the scintillator trays plumbed to a "source-mover". The source is inside a long flexible stainless steel tube. The source mover can (via computer control) push the source down any of the tubes and thus expose any of the tiles to the source. The same system will be used for the initial quality control testing at the remote site of the scintillator tray manufacturing. This quality control strategy is the same as used by CDF in their calorimeter upgrade project. Their experience gives us confidence that the strategy will work for CMS as well.

1.4.4 The central calorimeter photodetectors

The HB/HE photodetectors, which convert the optical signal from the fiber bundles corresponding to a tower, are required to have a linear dynamic range of 10^5 and operate in a uniform 4 T magnetic field. For calibration purposes, the detectors must have the capability of measuring the signal generated by a radioactive source as a DC current to a precision of 1%. In addition, the photodetectors are located inside the detector, adjacent to HB or HE itself, where service access is infrequent, thus placing an additional requirement on the mean time to failure. The useful lifetime of the photodetector must correspond to ten years of operation at a luminosity of 10^{34} cm^{-2} s^{-1}. A final requirement on the ratio of the signal to noise follows from the need to measure the signal from a minimum ionizing particle (m.i.p. ~ muon) in a single readout channel.

The proximity focused hybrid photodiode (HPD) is an image intensifier operated in the electron bombardment mode. Photoelectrons emitted from the photocathode are accelerated by an electric field and stopped in a silicon diode target where electron-hole pairs are produced generating the signal. In the device under our consideration, the 10 kV electric potential is uniform and the acceleration gap is 1.5mm to minimize magnetic field effects. Commercial devices are presently available in standard 18mm or 25mm diameter single channel versions. Prototypes have been made in which the diode is subdivided into pixels to make a cost effective multichannel device suitable for reading out fiber bundles corresponding to a number of calorimeter towers.

HPD's exhibit gain that is linear with applied voltage, being about 2000 at 10 kV. The gain has been measured to decrease by only 2% in the axial field of 3 T of the RD-5 magnet. The devices are linear to 2% over the required dynamic range of 10^5 and exhibit a fast response. The outstanding questions for these devices are the use of fiber optic windows, development of non-magnetic packaging, and further reduction of dark current.

The HPD has been chosen as the HB/HE baseline. Several manufacturers are under investigation (DEP and Hamamatsu).

1.4.5 Front end electronics

The electronic readout system of the HCAL will be based on the Fermilab KTeV QIE system for the front end electronics and the CERN FERMI system for readout electronics. The ADC has an effective a dynamic range of 5 MeV to 3 TeV.

The photodetectors and associated HV supplies, as well as their preamplifiers, will reside close to the HCAL detector itself, distributed around the outer radius of the $|\eta| = 1.3$ transition region from barrel to endcap. They would be attached to either the barrel or endcap and would be able to travel along with their own subdetector.

Electronic system specification

The HCAL electronics can be divided into the front end amplification, ADC and readout systems followed by Level I and Level II trigger Digital Signal Processors. High Voltage, Low Voltage and Slow Control systems and monitors are also required.

From the photodetector to the ADC, we require for each HB and HE channel a photodetector (HPD pixel), amplifier (linear 16-bit range, 40 MHz, 2000 electron r.m.s. noise), shaper-range compressor, ADC channel, cable driver, cable, and cable receiver. At Trigger Level I we require an HB1+HB2+HB3 adder, threshold test electronics, muon bit test electronics, DSP to extract energy and crossing time, DSP to transform energy to E_T and a synchronous link to the rest of Level I. At Trigger Level II we require Level I latency pipeline, DSP to correct gain and subtract pedestals, timing and trigger control interface, derandomization of readout buffers, and control synchronization.

Front end requirements

The front end requirements are set by the readout of the second HCAL tower longitudinal compartment (HB2), which contains the largest fraction of the hadron shower (on average). The requirements for the other two compartments (HB1 and HB3) can be less stringent, but for sake of uniformity of the electronics are identical to HB2.

The noise floor of the preamplifier and readout system is set by the requirement to cleanly recognize a muon or minimum ionizing signal. This capability is needed to provide independent and redundant information to the track and range signatures derived and matched to the tracker and external muon system. Taking the mean muon signal to be 10 photoelectrons, a threshold of 4 or more photoelectrons is 99% efficient. If this threshold is at 3 sigma of noise, the probability for a pedestal fluctuation to trigger is reduced to 0.25%. Equivalently, the pedestal r.m.s. should be less than 1 photoelectron (p.e.) for high tagging efficiency and low fake probability (2000 electrons r.m.s. after the HPD).

The upper end of the dynamic range is set by the expected maximum physics signal for the HB2 compartment. Because of the muon identification requirement, HCAL towers must be readout as energy, not transverse energy. Looking at the entire range of pseudorapidity coverage in HB and HE, considering the lateral size of hadron showers versus the actual tower size, longitudinal energy sharing, allowing for energy sharing between jet fragments, etc., we arrive at a target of 3 TeV as the maximum signal for the linear energy response of HB2. At 3 TeV, the constant term is dominant. Taking the constant term to be 5% and requiring the line shape to be valid 2 sigma above mean, sets a dynamic range of 15 bits or 33,000 photoelectrons to 1.

The resolution needed is determined by the constant term in the calorimeter response. Thus 8 bits of precision is more than satisfactory to reduce the quantization error to a negligible level.

The signal generated by a traveling radioactive source over each scintillator tile is a basic part of the calibration system. For the case of the HPD, this source signal is about 15 nA on top of a dark current of 5 nA. Calibration requirements require that a change in this current of better than 1% be measurable.

Charge injection is essential for diagnostics, complete system calibration and long term system monitoring. Stability, linearity and repeatability are all important for the charge injection system. These characteristics are tied to the source calibration requirements and call for a 0.5%

stability.

Cross-talk between readout towers can occur due to unwanted electrical or optical couplings. If such couplings are linear and can be removed, then a 2% ceiling on cross-talk can be tolerated.

Access, maintenance, operations

According to the current design, there is only very limited space to access the electronics for HCAL. Then the question arises: what fraction of dead channels will compromise the physics, especially the missing transverse energy measurement? Since repairs are tedious and lengthy, one has to understand the magnitude of the possible damage caused by dead channels.

We used a parameterized simulation program[8], and generated QCD dijets with partonic p_T greater than 2.5 TeV, as a physics source to estimate the missing transverse energy E_T^{miss}. To assess the effect of damage we randomly drop the energy in a given cell with either a 2% or 5% probability. The total E_T^{miss} is then compared to the case without any dead channels. We find that the impact is very small for 5% or less failures. To look at more "coherent" damage we require 5% or 10% dead channels in the barrel, endcap and the forward calorimeter. In this case we began to see a tail develop at high E_T^{miss} for 10% damage Fig. 1. 8. We conclude that up to 10% dead channels are acceptable.

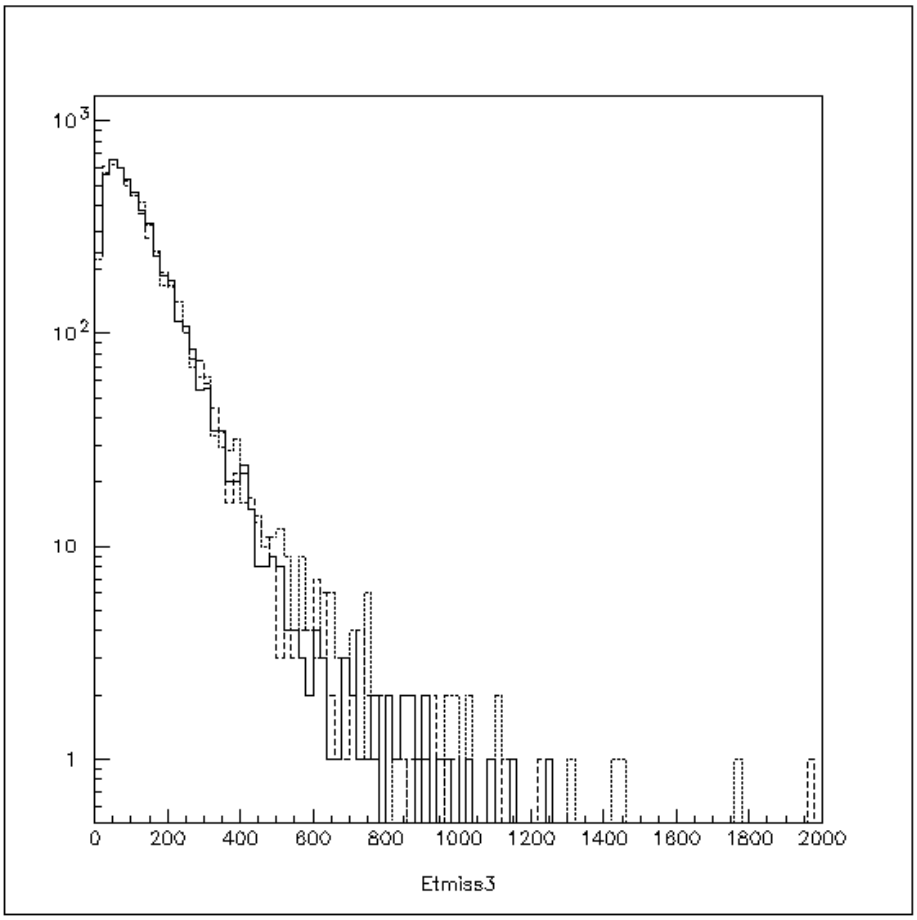

Fig. 1.8: Missing Et distribution for 0% dead channels (solid); 5% dead channels (small dashes); and 10% dead channels (large dashes).

1.4.6 Central calorimeter services

The barrel and endcap are serviced via the 100mm gap between the two subdetectors in the $|\eta| = 1.3$ region. This region also contains cables from the EM calorimeter and the tracking detectors.

Hadron Calorimeter related services include optical cables from the barrel and endcap megatiles and source tubes servicing each of the megatiles. Electronics and an occasional source driver box sit in a region close to the coil and also in the $|\eta| = 1.3$ region for both the endcap and the central barrel. The electronics boxes contain the tower optical mixing elements, photodetectors, the HV and LV distribution panels, tower preamplifiers, flash ADC's and digitizers (all functioning in a 4T magnetic field). The Electronic Boxes and Source Drivers are connected to the outside world via a cable path that snakes around the barrel and to the section around the central outer detector. The digitized photodetector signal, as well as power cables are routed through this path to electronics racks and power racks in the counting house.

1.4.7 Calibration and monitoring

Adequate performance of the hadron calorimeter requires that the response of the detector be uniform and stable in time at the level of few percent. The uniformity of response must, to first order, be assured by the construction and quality control. Experience of SDC and CDF shows that the uniformity of the tile fiber assembly can be maintained at 10% level for a large scale production. The assembly can be monitored by radioactive source and injecting light from UV lamps. Absolute calibration and linearity of the calorimeter will be established by exposing several modules to the hadron test beam. That calibration can be carried over to the CMS detector using radioactive sources. Both the QC/QA function and the transfer of test beam calibrations to other similar towers, imply the incorporation of source tubes crossing every scintillating tile, as in the SDC design. It is envisioned that the source tubes in most layers will be accessible only when the endcaps are withdrawn.

During the life of the experiment the response of the calorimeter may change as a result of radiation damage or aging. An over redundant system to monitor these changes and provide appropriate calibration must be envisaged.

^{137}Cs radioactive sources

All layers of the hadron calorimeter will be equipped with thin 1mm diameter stainless tubes that will route Cs^{137} radioactive sources throughout the system. This is a system similar to the one used by CDF and proposed by SDC. We propose that an absolute calibration between wedges be maintained by the source tube system, without exposing each wedge in a test beam.

A wire with a point-like Cs source will be pushed through these tubes by remotely controlled system of drivers. A DC current induced by the source traversing the tower will provide an accurate measurement of the response of the entire measuring chain. The experience at CDF shows that this measurement can be maintained at the level of 1%. Change of response due to photodetector or electronics will show up as a change of the response of all tiles of a given tower and can be compensated by the adjustment of the overall calibration factor. Change of response due to radiation damage will lead to a change of the measured current that is dependent on the depth in the calorimeter.

A few layers of the barrel and endcap will be monitored during data taking to verify that nothing unexpected has occurred. The primary recalibration of each tile, however, will take

place during long shutdown periods when access to the barrel and endcap source tubes is relatively easy.

Laser light calibration system

The laser light system will be used to monitor the stability of the photodetectors and the associated electronics. It will also be able to monitor the linearity of the pulse height measurement chain and provide control of the timing of each channel. In addition, the laser system will be the primary radiation damage monitor during the data taking phase of the experiment.

The laser calibration system will consist of a triggerable nitrogen laser, a system of neutral density filters covering an adequate dynamic range and a light distribution system delivering the UV light to both the HPD pixel and to the scintillating tiles via quartz fibers. The intensity of the laser pulses will be monitored by directing a part of the light to a block of scintillator and measurement of the resulting light pulses by a PIN diode. The rest of the light will go through a system of neutral density filters covering a dynamic range of 4 orders of magnitude to a cascade of distributor/commutator boxes. To achieve 1% some 10,000 p.e.'s must be detected. The total laser power requirement is ~ $1-10^{-3}$ J taking into account the total number of towers, photodetector efficiency and allowing for reasonable losses of light in the distribution process.

1.4.7.3 Calibration using data

Suitably chosen calibration triggers can be used to monitor the overall stability and/or absolute energy scale of the hadron calorimeter. For example minimum bias events can be utilized to maintain the uniformity of response and its time stability. Vector - boson or photon + jet triggers can be used to provide calibration and the absolute energy scale, as will be discussed later.

1.4.8 Radiation damage

It is assumed that the integrated luminosity over the first ten years of LHC operation will not exceed $5x10^5$ pb^{-1}. The ten year integrated dose is thus estimated to be 0.3 kGy (0.03 Mrad) at the front corner of the HB (see Table 1.2). It is shown later that up to 30% damage in HB will not induce an unacceptable constant term in the energy resolution. In common with most commercial polystyrene based scintillators, SCSN81 together with K27 doped WLS fiber such as Kuraray Y11, suffers a light yield reduction of about 20% at 10 kGy (1 Mrad) and an unacceptable 60% at 50 kGy (5 Mrad). The baseline HB and HE design uses this combination.

The problem of radiation damage to the plastic is most severe in the endcap (HE). In this detector, the radiation field scales approxiamtely as $1/\theta^3$ so the region at low $|\eta|$ is less seriously affected. In the endcap region, up to $|\eta| \leq 2$, our baseline is to use SCSN81 scintillator with Y11 doped fiber and 2 longitudinal segments. In this section the dose is <0.4 Mrad (see Table 1.1).

In the small angle region the dose is <2.4 Mrad (see Table 1.1). The longitudinal distribution of radiation damage has a characteristic length ~ λ, the nuclear interaction length. The total dose at the inner HE boundary is <2.4 Mrad over the lifetime of CMS. This dose falls off both with increasing angle and increasing depth. The energy deposition as a function of depth is shown below in Fig. 1.9. The exponential behavior is clear.

Fig. 1.9: Energy deposit as a function of depth for 30 GeV pions from the H2 test beam.

The loss of light output is related to dose, D , as ~ exp(-D/D_0), where D_0 for the Kuraray scintillator is ~ 3 Mrad. Therefore, a simple model for the radiation induced nonuniformity of HE is possible. Test beam data for 300 GeV pions from the H2 test with individual longitudinal readout is used. The individual layers were weighted by reduced light yields corresponding to different doses of radiation. The induced constant term as a function of dose is shown in Fig. 1.10, under the condition that the mean of the calorimetry is retained by recalibration of the HE1 and HE2 compartments.

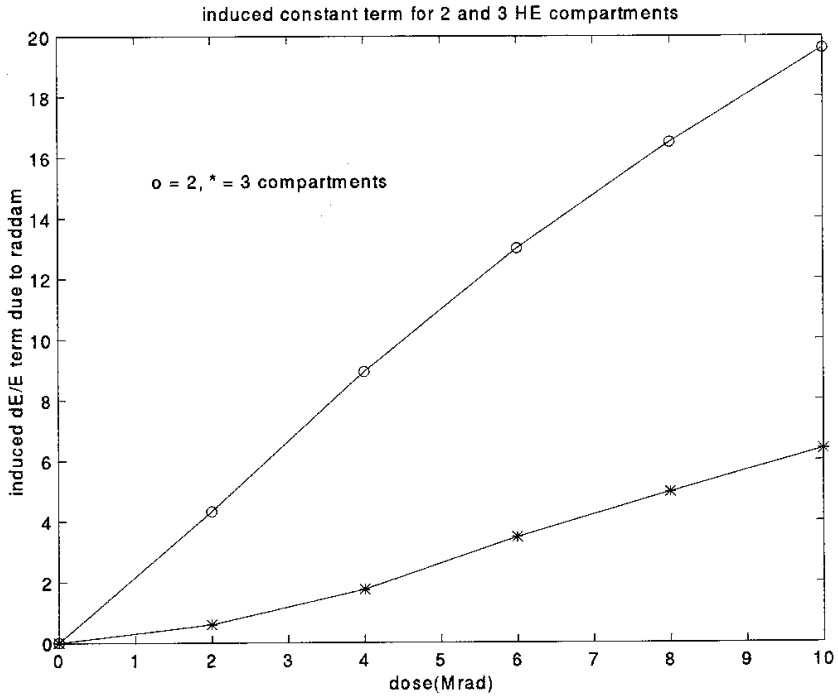

Fig. 1.10: Induced constant term in the energy resolution as a function of dose for 2 and 3

longitudinal compartments.

Clearly, for doses above about 2 Mrad, the induced constant term is comparable or exceeds the intrinsic constant term of the device. Therefore, for $|\eta| < 2$ the two compartments may simply be used for recalibration of the mean. However, for smaller angles in the HE towers a new strategy is needed. Two possible options can be considered. The first is passive, and consists of simply making a photographic mask which reflattens the depth response of the individual layers by throwing away light in the undamaged portion of the HE. A second approach is to further longitudinally segment the HE by adding new independent readouts. This approach does not require access to the detector nor does it require throwing away light, nor does it precluding the masking option.

The second alternative was studied for up to a 10 Mrad dose or a factor 4 worse than estimated as the real dose. A third compartment was added; HE1 a single layer, HE2 was the ensuing layers up to a depth ~ 2 λ in HE, and HE3 consisted of the remaining, largely undamaged layers. In this case the induced constant term at 100 kGy (10 Mrad) could be reduced to 6 % from the 20 % which was observed without extra longitudinal segmentation. Thus, a solution to the radiation damage problem, available at low cost, is to add a third HE segment to the readout in the region of highest damage. This precaution ensures that the HE performance is maintained over the lifetime of CMS.

1.4.9 The forward calorimeter design (HF)

Test beam results

The results of the test beam work with the HF hadronic and electromagnetic prototypes over the past two years forms the basis of the HF design:

a) The electromagnetic energy resolution using a quartz window PMT is $107\%/\sqrt{E}$, where E is the particle energy in GeV and the electromagnetic energy resolution is $137\%/\sqrt{E}$ if a glass window PMT is used.
b) The light yield is 0.87 photoelectrons/GeV for electromagnetic showers in the case of a quartz window PMT, and 0.53 p.e./GeV for a glass window PMT. For hadronic showers, the light yield depends on the energy. For example, 100 GeV pions give on the average 52 photoelectrons. For 1 TeV, the extrapolated data suggest that the average signal will be 610 photoelectrons.
c) The hadronic energy resolution contains an intrinsic component due to the fact that the Cherenkov mechanism responsible for the signal generation essentially selects only the π^o component of the developing showers. This irreducible resolution amounts to 25% at 100 GeV and if extrapolated from the test beam data, at 1 TeV, is 10%.
d) The calorimeter response was found to be dependent on the impact position of the incident particles. In a vertical scan with a narrow electron beam, the period of oscillation was found to correspond to the thickness of the grooved copper plates of which the prototypes were constructed. The effective sampling is slightly different when the particles enter the calorimeter at the position of the fibre (signal maximum), compared to where they enter between two fibres (signal minimum). This effect leads to a constant term in the energy resolution of about 1%.
e) The energy resolution of the quartz calorimeter contains contributions from the following components:
    - Photoelectron statistics: For electromagnetic showers, this contribution scales like $a/\sqrt{E}$ where the coefficient a is determined by the sampling fraction. For the

prototypes this equalled 1.07. This term is almost entirely responsible for the energy resolution. If the sampling fraction is doubled (i.e. 3% fibres in the absorber), then a goes down to $1.07/\sqrt{2} = 0.76$. For hadron showers, the situation is a little bit more complicated because of the non-linear response, but straightforward to calculate.

- Sampling fluctuations: These contribute to the resolution of fibre calorimeters as follows: $\sigma/E = a/\sqrt{E}$, with $a = 0.03 \times \sqrt{d/f}$ in which d is the diameter of the fibres in mm and f is the sampling fraction for minimum ionising particles[3]. For the tested HF prototypes, ($d = 0.3$ mm and $f = 0.00488$), the scaling constant a is thus about 25%. This formula allows to calculate the changes in the sampling fluctuations when the amount of fibre (f) and/or their thickness (d) are changed.
- A constant term, which results from the fact that the characteristic lateral shower dimension is of the same order of magnitude as the fibre pitch. This term can be estimated as follows. Using the measured lateral shower profile, one can determine the fraction of the signal producing shower contained in a cylinder with the fibre pitch as its radius. For hadronic showers in our prototypes, this fraction is 27%. The largest and smallest signal differ by 12% in the fibre matrix arrangement of the prototypes.

Layout

The HF calorimeters, located on both sides of the interaction point at 11.1 meters, cover the pseudorapidity range from 3 to 5. Each HF calorimeter consists of a large copper block that serves as the absorber. The embedded quartz fibers in the copper absorber run parallel to the beam and constitute the active component of the detector. Particles incident on the front face of the HF detectors produce showers in the copper/quartz matrix and a part of this shower (charged particles above the Cherenkov threshold) gives rise to Cherenkov light in the quartz fibers. This light forms the basis of energy measurement. The details of this device are presented in Chapter 5 and here we outline only the distinguishing features of this calorimeter here.

Structure

The HF calorimeters are cylindrically symmetric around the beam line. The radius of the active part of the HF is 1.4 meters. The length, along the beam, is 1.65 m, or about 10 nuclear interaction lengths. This is largely sufficient to longitudinally contain the Cherenkov signal produced by hadrons of up to 1 TeV. The central region is open (25 cm in diameter) to allow for the beam pipe (20 cm in diameter).

In order to optimize for the energy resolution, for E and E_T flows and forward jets, the calorimeter has three segments in depth. This effective multiple segmentation within a monolithic copper absorber is achieved by using three different fiber lengths. We refer to them as Long (or EM, 165 cm long), Medium (or HAD, shorter by 22 cm from the front of the module) and Short (or TC, inserted 30 cm from the back face). Fig. 1.11 schematically shows one of the quadrants of the HF where only the top fiber layer is exposed.

The fibers are arranged into towers such that transverse dimensions are 5×5 cm^2 in the inner part ($|\eta| > 4$) of the HF, and 10×10 cm^2 in the outer region ($|\eta| < 4$), to maximize the forward jet detection and reconstruction capability over a huge pile-up background. The Short fibers serve as the active material of the tail catcher (TC) section and they are arranged in a coarser tower structure, 20×20 cm^2.

Manufacture, shipping, assembly and installation

The HF calorimeters are constructed using a few relatively small size modules. Four different sizes of modules are envisioned to be the basic building blocks of the calorimeter. They have the following dimensions; ($w \times h \times l$) $600 \times 300 \times 1650$ mm^3 (32 units), $500 \times 300 \times 1650$ mm^3 (32 units), $300 \times 300 \times 1650$ mm^3 (16 units) and $600 \times 200 \times 1650$ mm^3 (8 units). These modules are constructed from copper plates with grooves and these plates are stacked together by diffusion welding such that the modules are self-supporting and mechanically sound. The quartz fibers are inserted into the holes (grooves) after a quadrant fabrication is mechanically completed. Each quadrant (as shown in Fig. 1.11) is composed of 11 basic modules that are mounted on a steel shell which provides structural support in assembly, installation and shipping. It also serves as a part of radiation shielding components when installed in the beam position.

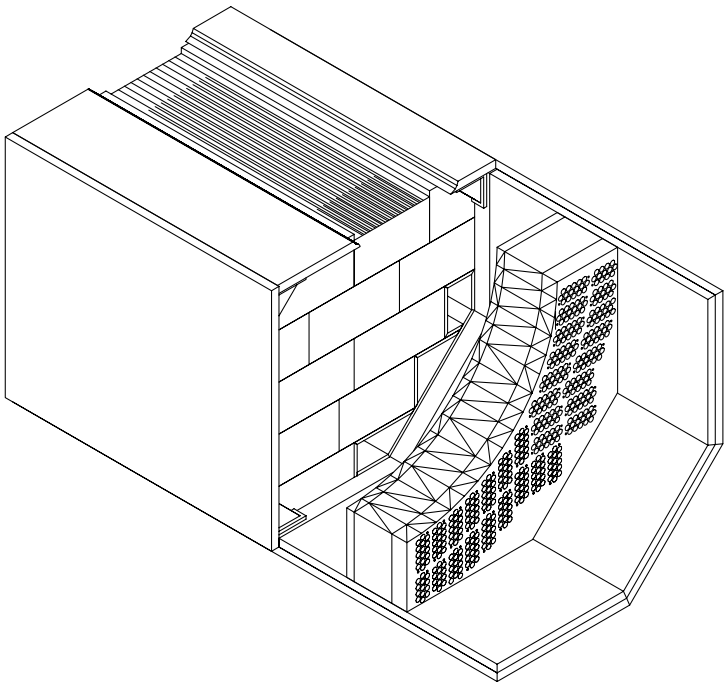

Fig. 1.11: An HF quadrant above shows that it is constructed from 11 modules. A top and a side steel plates are used during transportation and as a part of the assembly procedure. A cut-out of one of the top modules shows three different lengths of fibers inside the absorber that represent EM, HAD and TC sections. The PMT boxes are mounted on the right of the shielding where the PMT foot-prints are shown.

The HF shipments are brought about a quadrant at a time, proceeding each stage of assembly completion. First, the absorber modules are put together in a structural steel shell in quadrants, tested and transported. This is followed by the insertion of quartz fibers into the holes and fiber bundling into towers, and shipped again in quadrants to the assembly site at CERN where the photodetectors and the other auxiliary components are mounted. Quadrants are assembled into halves (1/2 of HF arm) and then to full detectors in the same area (Building 168). Entire test assembly with the transporter platforms and the shielding blocks is also fulfilled in the assembly area before shipment to the CMS surface hall and installation in the experimental hall.

1.5 DESIGN PERFORMANCE (TEST BEAMS, LAB TESTS, SIMULATIONS)

During the R&D period of 1994 through 1996 considerable data was taken and a variety of tests were made for HB, HE and HF. Test beams of electrons, pions, protons, and muons were used in the H2 and H4 beamlines. In particular, the H2 data were taken at fields up to 3T in strength and in both "barrel" and "endcap" configurations. The combined CMS calorimetric system of ECAL+HCAL was tested in 1996. In addition to the beam tests, laboratory tests of the scintillator "brightening" phenomenon were made as were continuing radiation damage studies.

The HCAL group has attempted to also mount a complete set of simulations. Their purpose is both to assess the possible adverse impact of HCAL performance on physics searches in CMS and to serve as a method to allow extrapolations from test beam results to the HCAL baseline design.

A new effect was uncovered in the 1996 data taking period. In the barrel configuration, the effective e/π response ratio of the HCAL sampling calorimeter is a function of magnetic field. The effect is well understood, and the GCALOR Monte Carlo program gives a good representation of the data. Note that in the endcap this effect does not exist. In HE only scintillator brightening is observed to occur. The magnitude of the effect is tracked by both radioactive sources and muons. In HF there is no magnetic field so that the problem is localized to HB.

The existence of this effect has modified our calibration scheme somewhat, since it cannot be tracked at zero field. Hence, a plan to use in situ calibration using Z + jet final states and others is needed in order to establish the absolute calibration of the HCAL system. Since the sensitivity of the HCAL mean pion energy to space in the sampling gap is ~ 4%/mm, a QC plan to fix the scintillator package at a fixed location has also been adopted.

In summary, we have measured the relevant parameters of HCAL in test beams. In concert with an extensive Monte Carlo program, a good understanding of the response of HCAL exists, giving confidence that the performance of HCAL can be accurately predicted. Using the test beam results, we have explored a wide variety of Physics processes embodying new Physics beyond the standard model. For example, we do not find that the calorimetric performance degrades searches for SUSY, but that CMS is dominated by real backgrounds containing neutrinos.

1.5.1 Overview of physics performance

As explained earlier, the goals of the hadron calorimeter subsystem are to identify and measure hadronic jets and missing transverse energy. Physics processes for which these final state signatures are crucial include:

a) High mass (~ 1 TeV) standard model Higgs searches in llνν, lljj and lνjj modes.
b) Forward tagging jets for high mass Higgs production and strong WW scattering processes.
c) Supersymmetric Higgs searches in H and A $\rightarrow \tau\tau$ modes, h $\rightarrow$ bb (produced by A $\rightarrow$ Zh or H $\rightarrow$ hh), and t $\rightarrow$ b $H^{\pm}$ with $H^{\pm} \rightarrow \tau\nu$.
d) Searches for supersymmetric particle production, which generally involve signatures consisting of missing transverse energy (arising from the escape of the lighest supersymmetric particle from the detector) plus jets and leptons.
e) Determination of the mass spectrum of supersymmetric particles will require reconstruction of invariant masses from combinations of jets (possibly b-tagged or anti-tagged) and missing

transverse energy.

f) Discovery of technicolor states may require reconstruction of invariant masses of multijet systems such as $\rho_T \rightarrow jj$ or $\omega_T \rightarrow \gamma jj$.

g) Discovery of compositeness would require the accurate determination of the cross section for high transverse momentum jets up to several TeV in E_T, and measurement of their center of mass angular distribution.

Many of these processes were investigated for the Technical Proposal[1]. Since that time, the physics performance of the CMS hadron calorimeter has been investigated both as part of ongoing studies within the physics group and as part of the effort to optimize the detector.

We have considered two performance benchmarks. For **missing transverse energy**, E_T^{miss}, we take the ability to discover and characterize supersymmetry as our benchmark. There is an unavoidable background to E_T^{miss} signals which results from the mismeasurement of QCD jets, and the production of heavy flavor within them (this dominates at relatively low E_T^{miss}, below about 100 – 200 GeV) and from the production of top and vector bosons, whose decays produce high-p_T neutrinos (which tends to dominate at higher E_T^{miss}). The background component from real neutrinos is irreducible and sets the scale for the measurement precision which is required to see new physics.

The finite pseudorapidity coverage of the detector introduces a mismeasurement of E_T^{miss}, as shown in Fig. 1.12; if the calorimeter coverage is reduced significantly below $|\eta| < 5$ then the rate for E_T^{miss} begins to substantially exceed the unavoidable background. For this reason, the CMS hadron calorimeter is designed to cover the whole range $|\eta| < 5$.

For the LHCC SUSY workshop held at CERN in October 1996, a number of studies were carried out using the fast parametrised Monte Carlo simulation CMSJET[9]. This simulation smears the energy of incoming particles according to assumed resolutions; for single hadrons in the HCAL these were $\sigma/E = 70\%/\sqrt{E(GeV)} \oplus 9.5\%$ (at $\eta = 0$), and in the HF, $\sigma/E = 172\%/\sqrt{E(GeV)} \oplus 9\ \%$. On the basis of these studies, we concluded that:

a) the CMS detector could discover squarks and gluinos up to masses of ~ 2 TeV, using a single charged lepton plus jets and E_T^{miss} signature. (This final state gives a greater reach than a pure E_T^{miss} or E_T^{miss} +jets search). Such masses are well above the maximum at which SUSY at the electroweak scale is felt to be reasonable.

b) CMS could observe sleptons, in leptons + E_T^{miss} final states, above the standard model and SUSY backgrounds up to masses of about 340 GeV;

c) CMS could observe chargino and neutralino production in leptons + E_T^{miss} final states, if nature lies in the region of parameter space where production cross section and branching ratio to leptons are significant. The lepton spectrum can be used to measure some of the neutralino masses.

A summary of the parameter space accessible to CMS is shown to Fig. 1.13.

The only concern is that the parametrized simulation may not provide a realistic model of the detector performance, particularly as far as E_T^{miss} is concerned. We have therefore evaluated[10] a number of very pessimistic scenarios for HCAL performance. As a baseline, we considered HCAL single-particle resolutions similar to those quoted in the Technical Proposal: $\sigma/E = 65\%/\sqrt{E(GeV)} \oplus 5\%$ (at $\eta = 0$), $\sigma/E = 83\%/\sqrt{E(GeV)} \oplus 5\%$ (in the endcaps), and in the HF, $\sigma/E = 100\%/\sqrt{E(GeV)} \oplus 5\ \%$. We then degraded this performance in the following ways:

a) increased sampling terms in the resolution: $100\%\sqrt{E(GeV)}$ in the barrel, $150\%\sqrt{E(GeV)}$ in

the endcap and 200%$\sqrt{E(GeV)} \oplus 10\%$ in the HF;

b) assumed no measurement of electromagnetic energy takes place for $1.5 \leq |\eta| \leq 1.6$ (an unsampled crack in the EM calorimeter);
c) assumed no measurement of any energy takes place for $3.0 \leq |\eta| \leq 3.1$ (an unsampled crack between the HCAL endcap and the Forward Calorimeter HF);
d) degraded the HCAL response function to model 0.6 λ of material between the rear of the ECAL crystals and the front face of the HCAL, which introduces a low-side tail to the hadronic response with probability of losing an energy E_{loss}, $P(E_{loss}|E) \sim \exp(-E_{loss}/0.067E)$.
e) an alternative parametrization of a non-Gaussian low-side tail was also considered, chosen as a worst-case based on test beam data: 0.2% of events were shifted to the tail, and E_{loss} was distributed uniformly between zero and the incident energy.

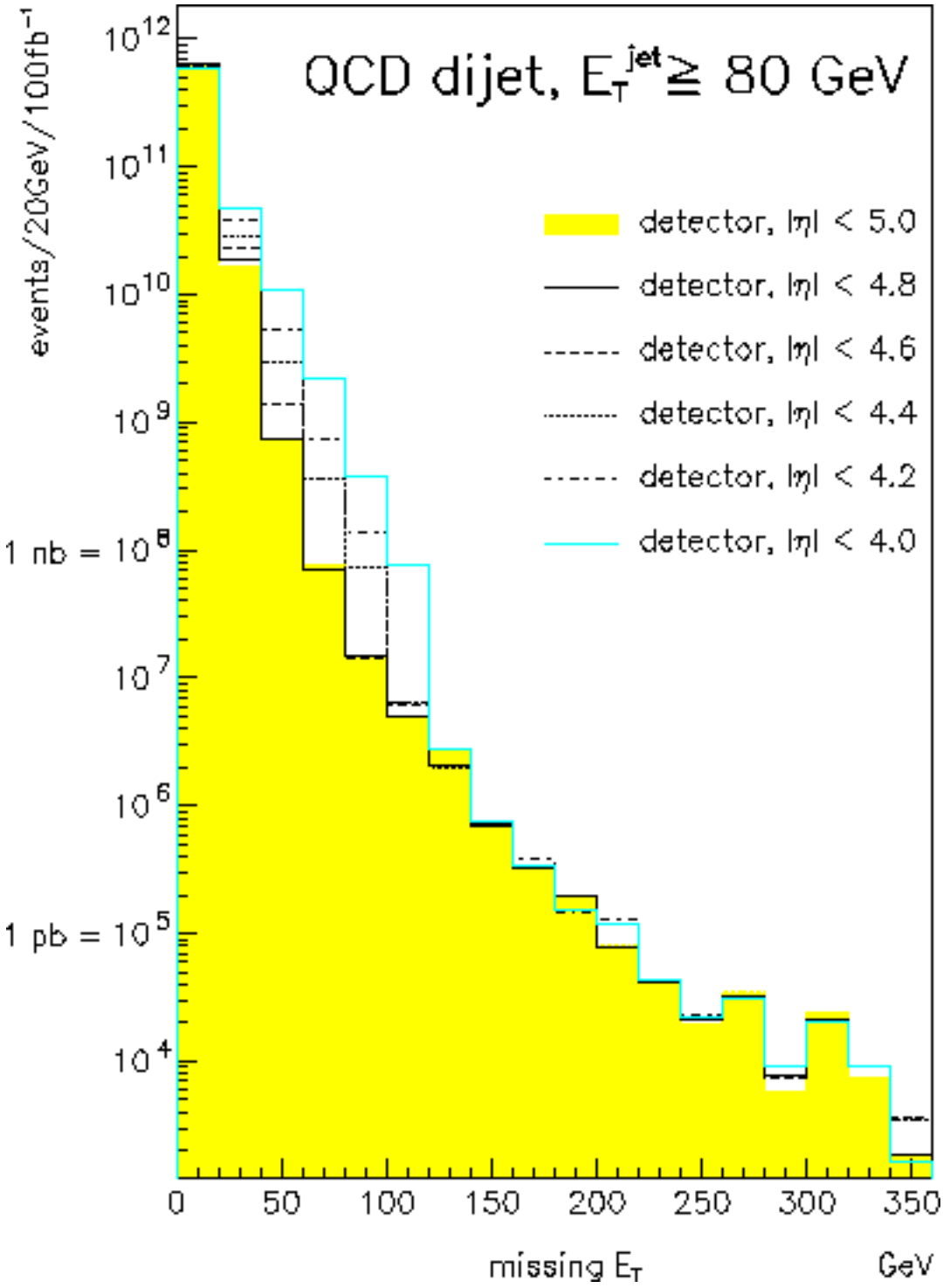

Fig. 1.12: Cross section at the generator level for E_T^{miss} from QCD dijet events, with E_T^{jet} > 80 GeV, showing the effect of varying pseudorapidity coverage.

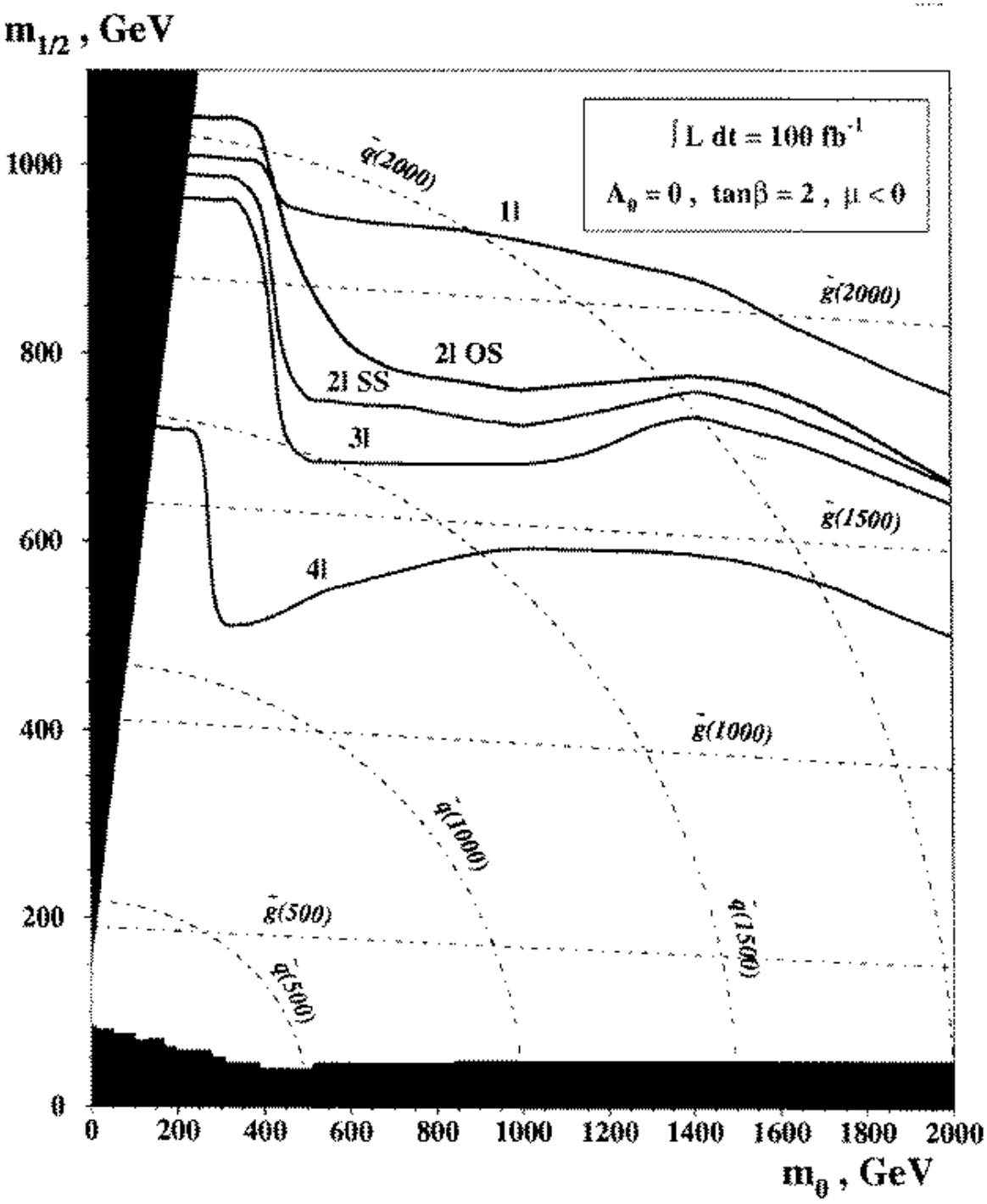

Fig. 1.13: Parameter space of the supergravity-inspired minimal supersymmetric standard model, m_0 vs $m_{1/2}$, with lines showing the 5σ discovery reach for the CMS detector with 100 fb^{-1} of data. The searches required missing transverse energy, jets, and one lepton (1l), two leptons of same sign (2l SS) or opposite sign (2l OS), three (3l) or four (4l) leptons. Dashed lines are contours of constant squark and gluino masses, showing the CMS reach to be up to ~ 2 TeV, well beyond theoretical expectations for supersymmetry at the electroweak scale.[11]

We evaluated the effect of these scenarios on the observability of supersymmetry at CMS in the E_T^{miss} + jets channel. All of them are far worse than the performance we actually expect from CMS, yet none would actually prevent the discovery of supersymmetry. All tend to

increase the background most at low values of E_T^{miss}, because this is the region dominated by mismeasurements of jets. The worsened, but still Gaussian, calorimeter resolutions would increase the luminosity required for an observation of SUSY by a factor of about 1.5. The pessimistically-modelled cracks have somewhat more serious effect, but by far the greatest impact comes from introducing non-Gaussian response functions. (The first parametrization considered increases the QCD background at $E_T^{miss} \sim 150$ GeV by two orders of magnitude). In the optimization of the HCAL detector, we have therefore placed considerable stress on the elimination of sources of non-Gaussian response, such as unsampled material between the rear of the ECAL and the front face of the HCAL.

We have also verified that the performance indicated by the HCAL test beam data is adequate for E_T^{miss}. In Fig. 1.14, we compare the cross section for QCD jet events as a function of E_T^{miss}, for the technical-proposal-like resolutions used as a baseline in the studies described above, and the result of a parametrization to the resolutions actually obtained from test beam data. The test beam performance is not quite as good as the earlier simulations, increasing the E_T^{miss} cross section by a factor of about two at moderate E_T^{miss}, this will not have a serious impact on the physics capabilities of the detector. As stated earlier, we have worked hard to remove sources of non-Gaussian response rather than striving to obtain the best possible resolution, since the impact on physics of a non-Gaussian response is much more severe.

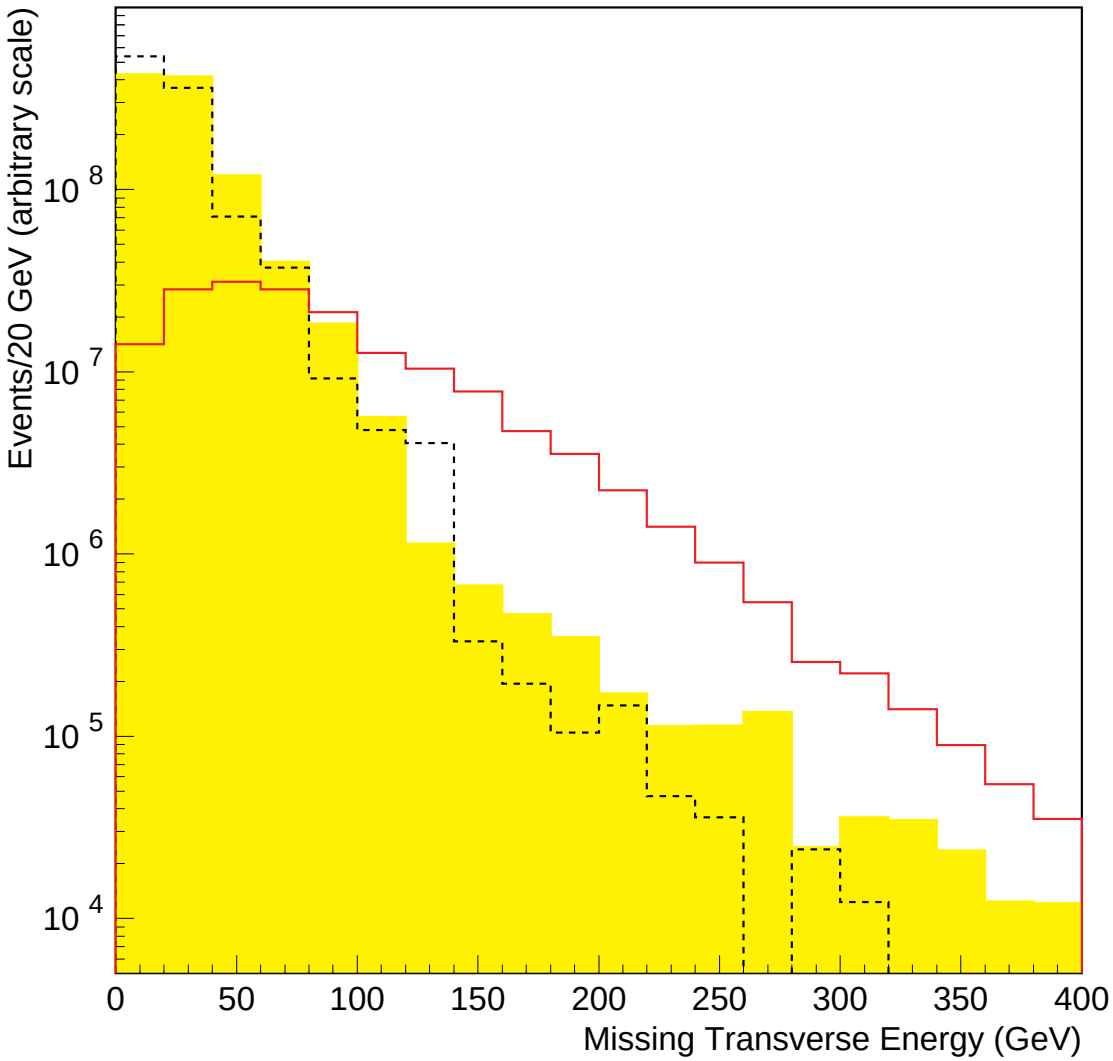

Fig. 1.14: Cross section for measured E_T^{miss} from QCD dijet events in CMS. The shaded histogram shows the result using single-particle resolutions taken from the test beam, while the open histogram is the technical-proposal single particle resolution. The second open histogram represents real physics background sources of neutrinos from W, Z and t decays. At least three jets were required, with E_T > 100, 80 and 60 GeV, and the E_T^{miss} was required to have an azimuthal angle from the leading jet between 20° and 160° to reduce the effect of mismeasurements. The physics backgrounds dominate for E_T > 75 GeV.

For **jet resolutions**, our performance benchmark is the ability to reconstruct the dijet decays of W and Z vector bosons. We have investigated this both in the context of a high-mass Higgs search, $H \rightarrow WW \rightarrow l\nu jj$, and in top decays ($t \rightarrow Wb \rightarrow jjb$). The latter process may be of interest as a calibration channel as well as for physics.

In the Higgs search[12] the W has significant transverse momentum. The $W \rightarrow jj$ decay was therefore reconstructed from the calorimeter lego plot by finding a single large cluster (a cone of radius R = 0.8) containing two smaller jets (with a cone size of R = 0.15). The mass of the W was then estimated as the invariant mass of the whole large cluster, without attempting to assign energy between the two small jets. A requirement that the two jets have $(E_1 - E_2)/(E_1 + E_2) < 0.7$ reduces the W+jets background to the lνjj final state. Good resolution is obtained, with a FWHM of ~ 20 (30) GeV for m_H = 800 GeV without (with) minimum bias pileup. Since

the dijet resolution is broadened by many unavoidable effects, such as out-of-cone showering, gluon bremsstrahlung, and combinatorics, our goal has merely been to avoid detector effects further degrading it. One example of such an effect would be the smearing introduced by the finite tower size of the calorimeter. Our studies indicate that, provided the tower size is smaller than about $\Delta\eta \times \Delta\phi = 0.1 \times 0.1$, the dijet resolution is not affected.

The top study[13] is complementary because the W is produced with lower transverse momentum and so two discrete jets are observed. Test-beam derived single particle resolutions were used. The simulation required between two and six jets with $E_T > 20$ GeV. The jets used to form the W were required to be more than R = 0.6 from either b-quark direction and to have an opening angle between 0.25 and 1.5 radians. They were then combined with one of the b-quarks to form a three-jet mass, which was required to be consistent with m_T (This last requirement gives a clean W for calibration purposes but would obviously not be appropriate for some top physics studies). Fig. 1.13 shows the resulting reconstructed m_W distribution, without minimum bias pileup; again, the FWHM is about 20 GeV. If minimum bias pileup events are included, this degrades to about 30 GeV as before.

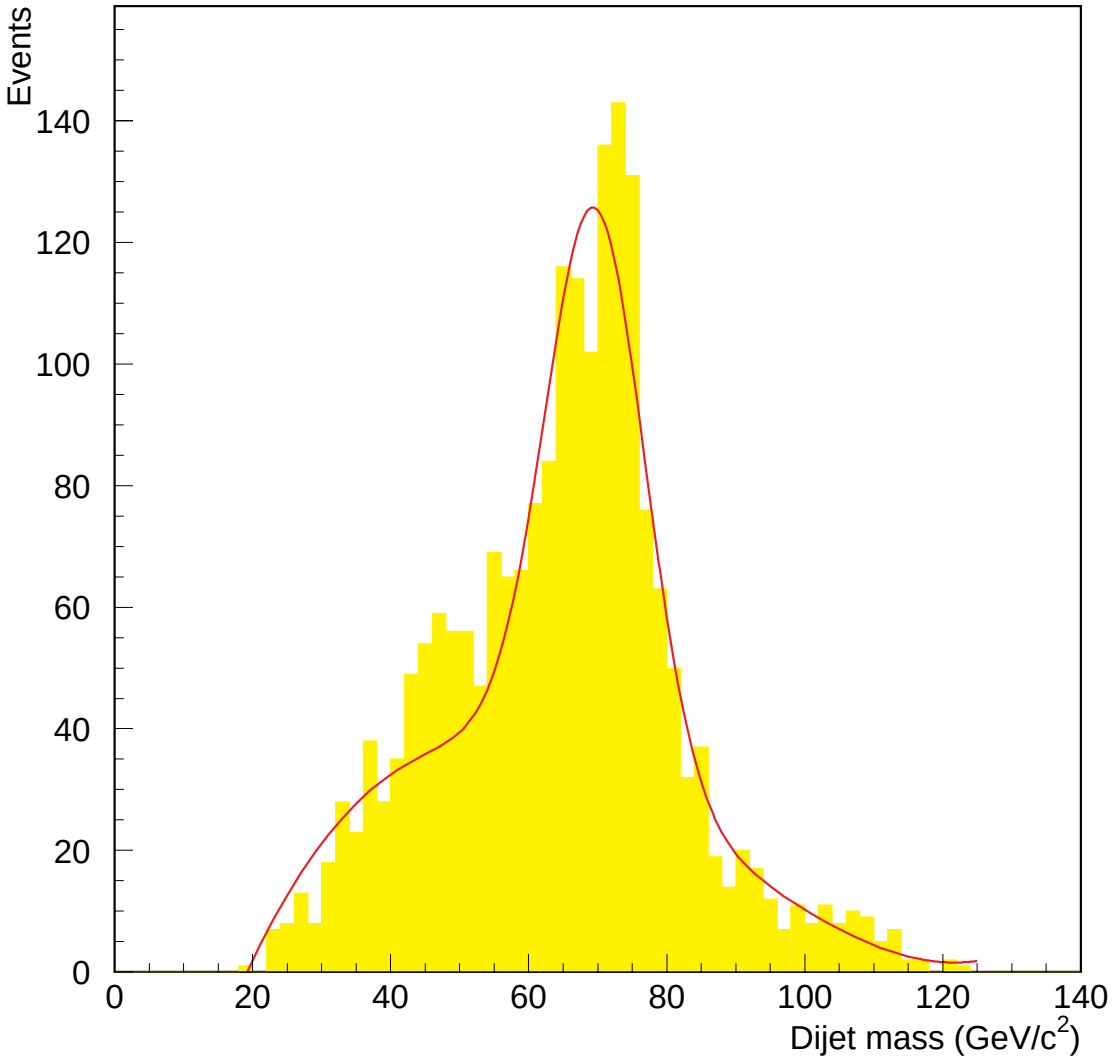

Fig. 1.15: Reconstructed dijet mass distribution from top decays showing the W peak. A jet cone size of R = 0.4 was used with no minimum bias pileup events.

In summary we believe that the HCAL design presented here can meet the physics goals of the CMS detector and is well-matched to the tasks required of it.

1.5.2 HB/HE test beam results

The CMS HCAL group has tested the performance of prototype HB sampling calorimeters with copper absorber/scintillator tiles and optical readout system using wave length shifter (WLS) fibers[14]. Each sampling layer of the HCAL colorimeter was read out separately, allowing for an simulation of variety of absorber configurations. The group has also in the same period tested HE and HF prototypes. The HF results are discussed in the next section.

During May 1995[15,16] we tested the prototype calorimeters in the CERN H2 beamline with the detector placed inside a large 3 Tesla magnet. The orientation of the magnetic field, with field lines perpendicular to the scintillator planes, corresponded to the Hadron Endcap (HE) configuration as shown in Fig. 1.16. In September 1995, we tested[17] the HCAL prototype in the H4 beamline (with no magnetic field present) with an ECAL detector consisting of a matrix of 7×7 $PbWO_4$ crystals. The CMS combined calorimetric system of ECAL+HCAL was tested[18] in 1996 at the H2 beamline. This time, the 3 Tesla magnet was oriented in such a way that B field lines were parallel to the scintillator planes, corresponding to the CMS HCAL Barrel configuration. The H2 (1996) setup is shown in Fig. 1.17.

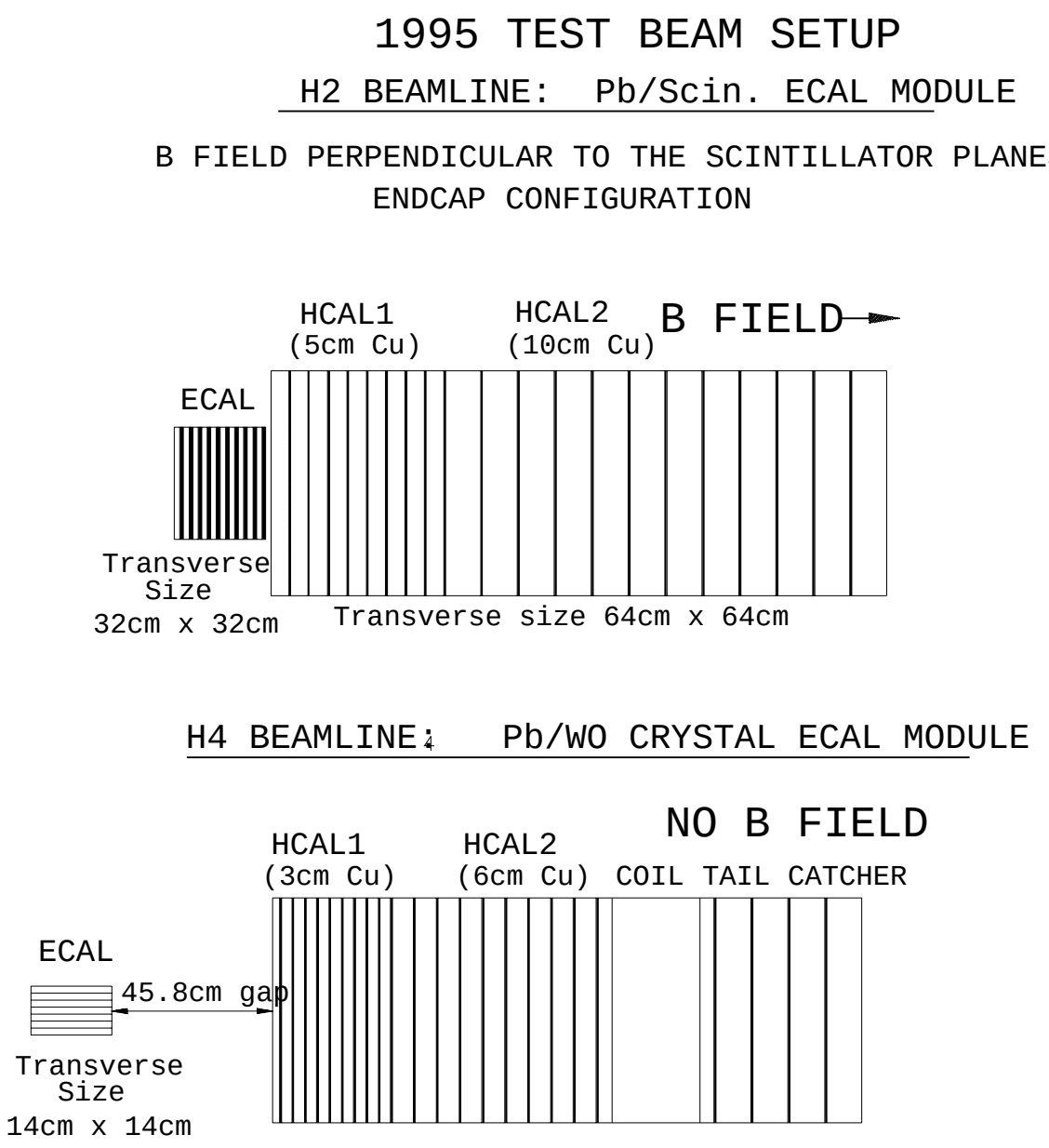

Fig. 1.16: 1995 H2 and H4 test beam setup.

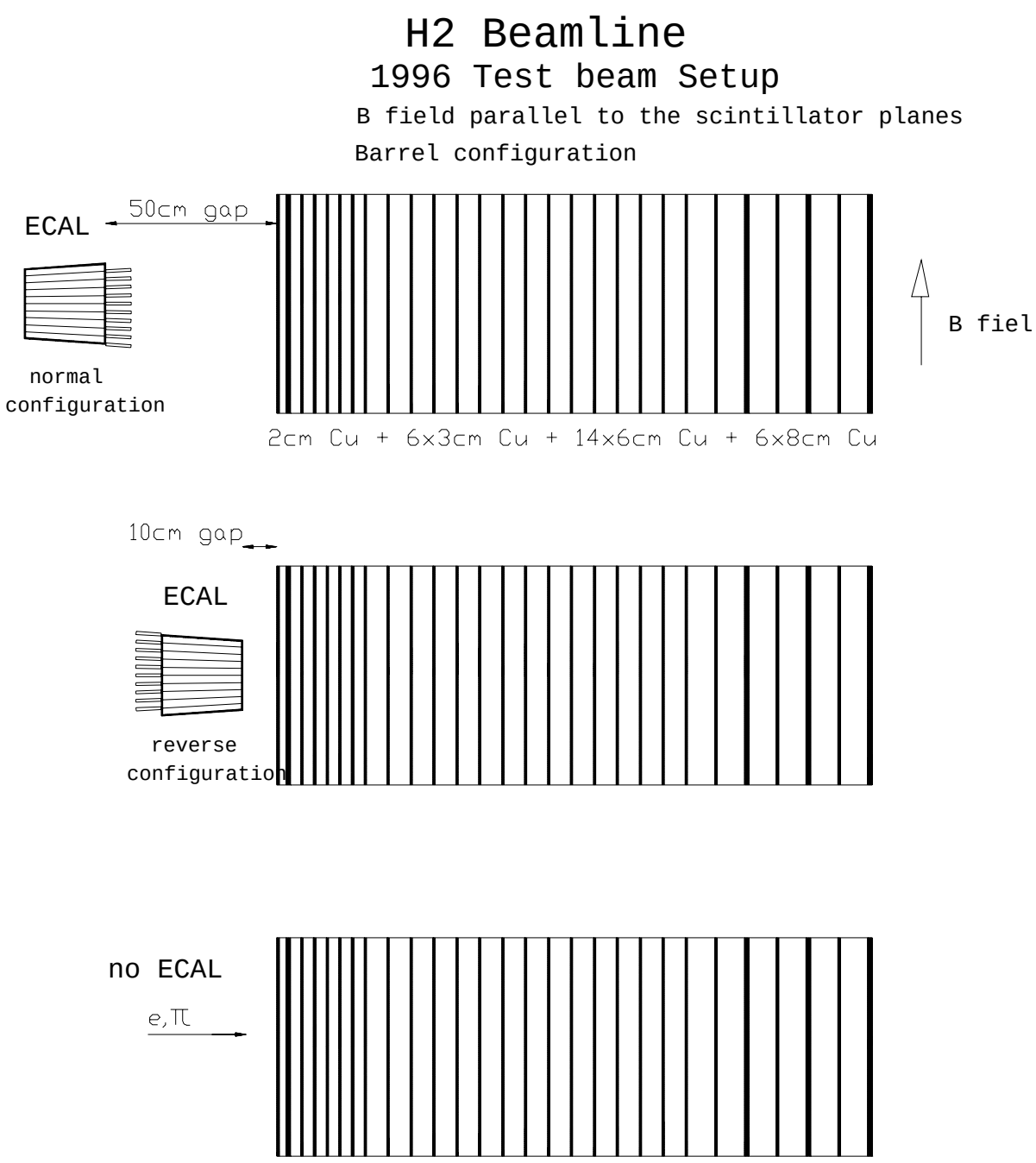

Fig. 1.17: 1996 H2 test beam setup.

In the following we summarize the results of HCAL Test Beam studies.

HCAL absorber depth studies

The ECAL detector consisted of a 7×7 matrix of 2cm×2cm $PbWO_4$ crystals. Approximately 95% of electron electron energy was contained inside a 3×3 crystal sum. The linearity of the ECAL response to electrons is shown in Fig. 1.18 while the electron energy resolution of ECAL is shown in Fig. 1.19. The resolution is well described by a 6% stochastic term (due to crystal photostatistics), 0.5% constant term (due to relative crystal-to-crystal calibrations) and 100 MeV/crystal incoherent electronic noise term. Note that this performance

is not the ultimate achievable for ECAL. It was simply made sufficient as to have no impact on the HCAL data.

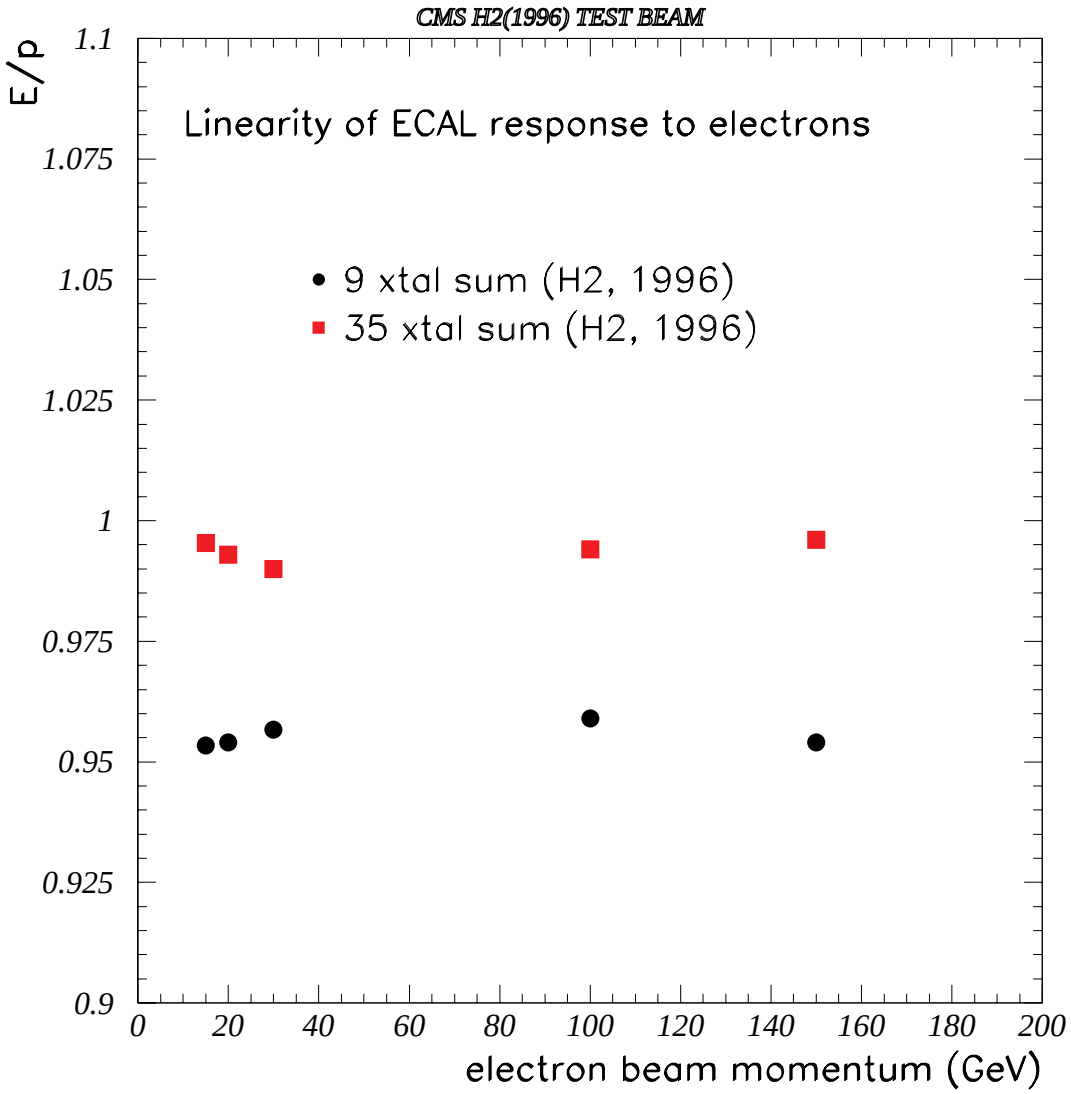

Fig. 1.18: Linearity of ECAL crystal detector to electrons.

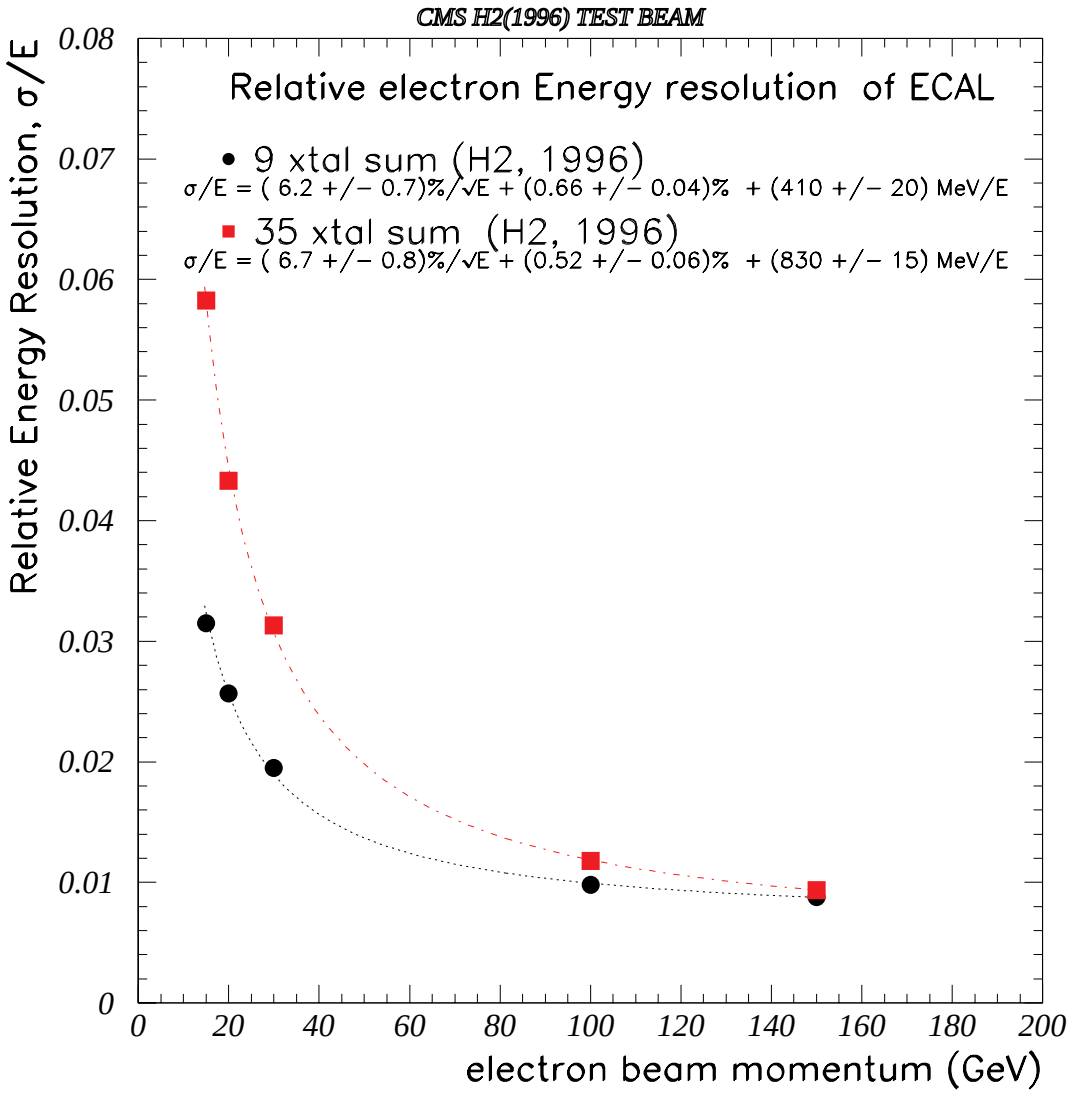

Fig. 1.19: Electron energy resolution of the ECAL detector.

The HCAL calorimeter was segmented into 27 layers, each read out independently by a photomultiplier. Relative calibration of individual HCAL layers was performed by equalizing the response of each layer to minimum ionizing particles. An average muon deposited approximately 4 GeV of energy in HCAL.

Fig. 1.20 shows the various sampling configurations simulated with the Test Beam apparatus. The "all layers" configuration corresponded to the case when all available samplings were included in the energy sum. A "baseline" HCAL configuration (assuming the inner HCAL radius of 1930 mm) used fourteen 6cm Cu samplings inside the magnetic coil, with a total equivalent of 5.2 interaction lengths inside the coil.

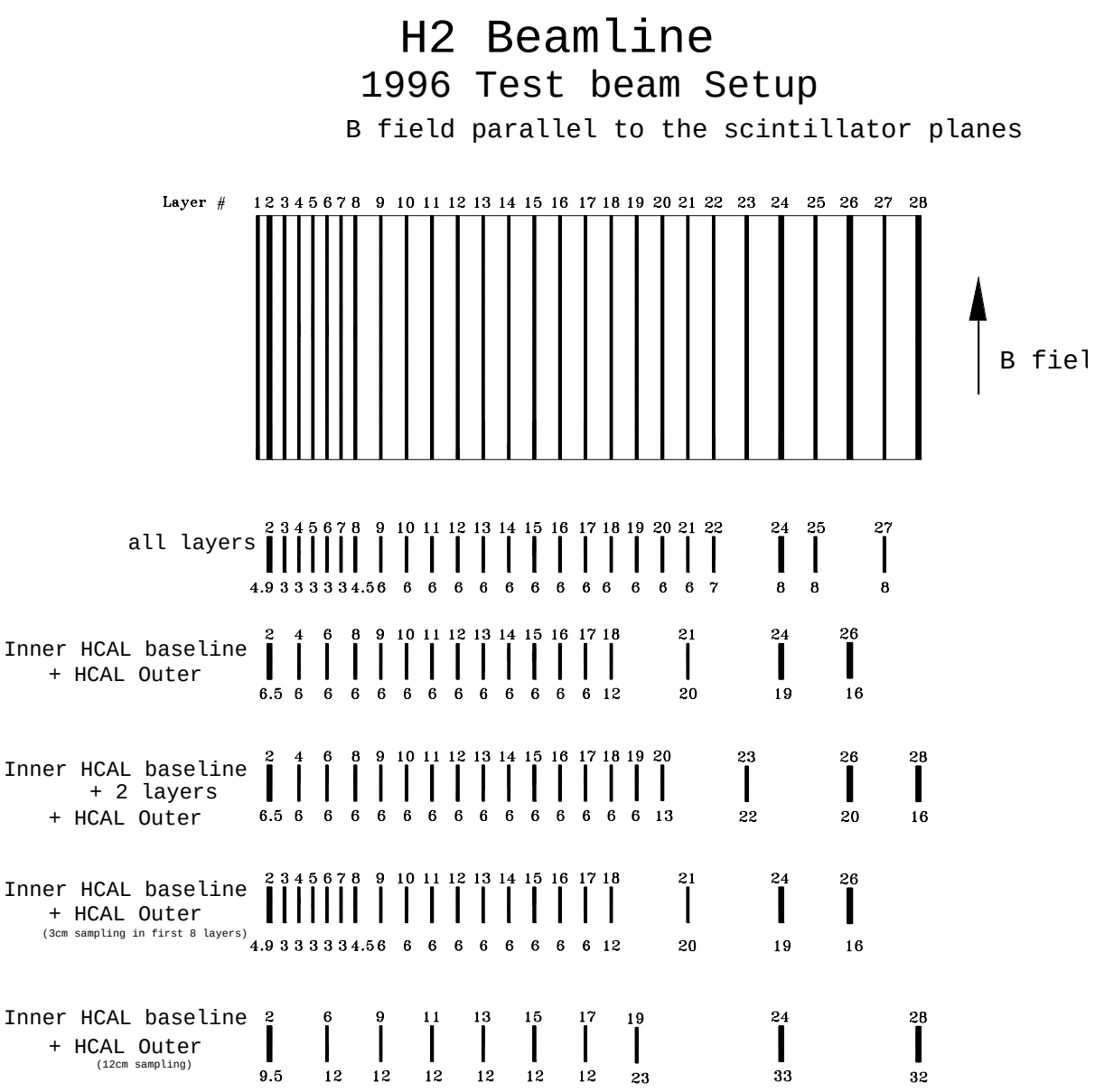

Fig. 1.20: Various sampling configurations simulated with the Test Beam apparatus.

Fig. 1.21 shows the average 50, 100, 150 and 300 GeV pion shower profiles as a function of calorimeter absorber depth. As shown in the figure, the average pion shower profiles extend significantly beyond 5.2 λ. In order to avoid the large energy tails of pions not fully contained by the HCAL inside the magnetic coil, we have added a HCAL Outer (HO) compartment. Note that the baseline of 5.15 λ HCAL + 1.1 l ECAL has $e^{-6.2}$ = 1/493 or a ~0.2% probability to not enteract in HB at all. The HO consists of 2 readout layers (3 in low eta region) and would sample energy immediately after the magnetic coil and between the iron plates of the Muon system.

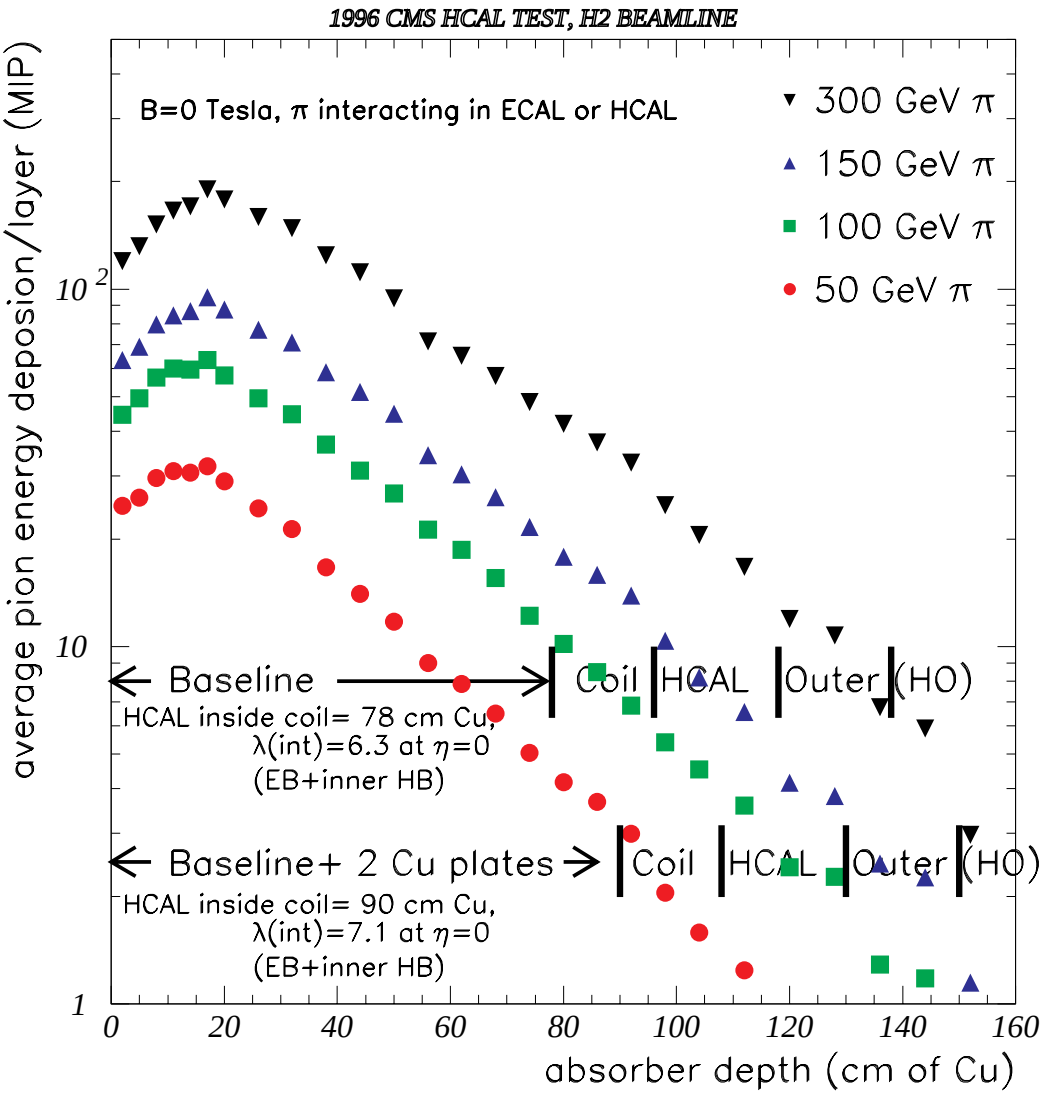

Fig. 1.21: Average 50, 100, 150 and 300 GeV pion shower profiles as a function of calorimeter absorber depth.

If an additional 2 layers of 6 cm Cu plates were added to the baseline HCAL design, the total depth of the HCAL inside the coil would increase to 5.9 λ. Fig. 1.22 shows the energy measured for 300 GeV pions for different HCAL sampling configurations: Baseline Inner HCAL, Baseline + 2 plates, Baseline + HO, and Baseline + 2 plates + HO. Adding the HO reduces the gaussian width as well as the non-gaussian low energy "leakage" tails in the energy distributions.

Fig. 1.23 shows the fraction of 300 GeV pions with energy reconstructed below 200 GeV (approximately 3 sigma below the mean). The fraction reduces from approximately 4% for the Baseline HCAL inside coil (total 5.2 λ), to less than 2% for the case of HCAL with 2 additional plates and HO (total 9.8 λ).

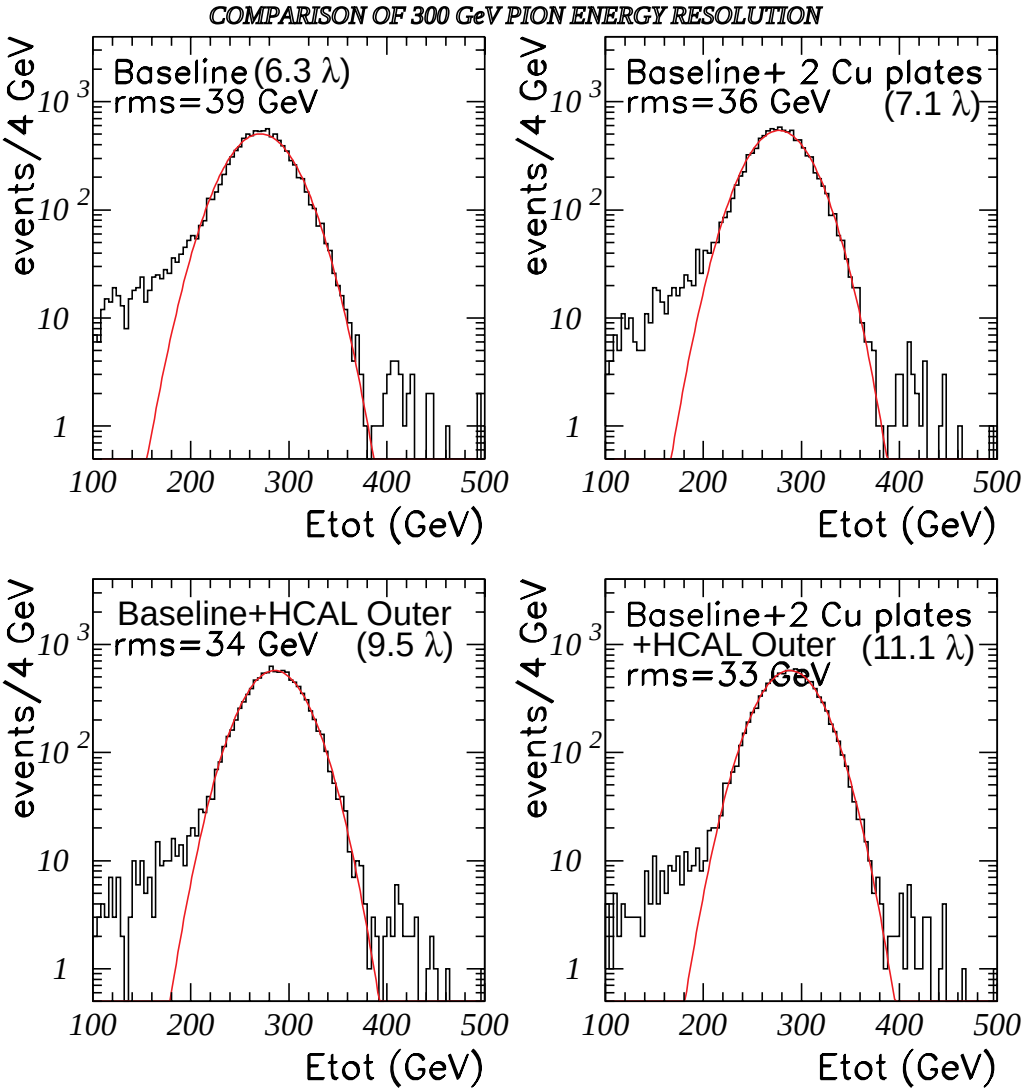

Fig. 1.22: Comparison of energy resolution (rms) for 300 GeV pions for different HCAL sampling configurations: Baseline Inner HCAL, Baseline Inner HCAL +2 plates, Baseline Inner HCAL + HO, and Baseline Inner HCAL + 2 plates + HO.

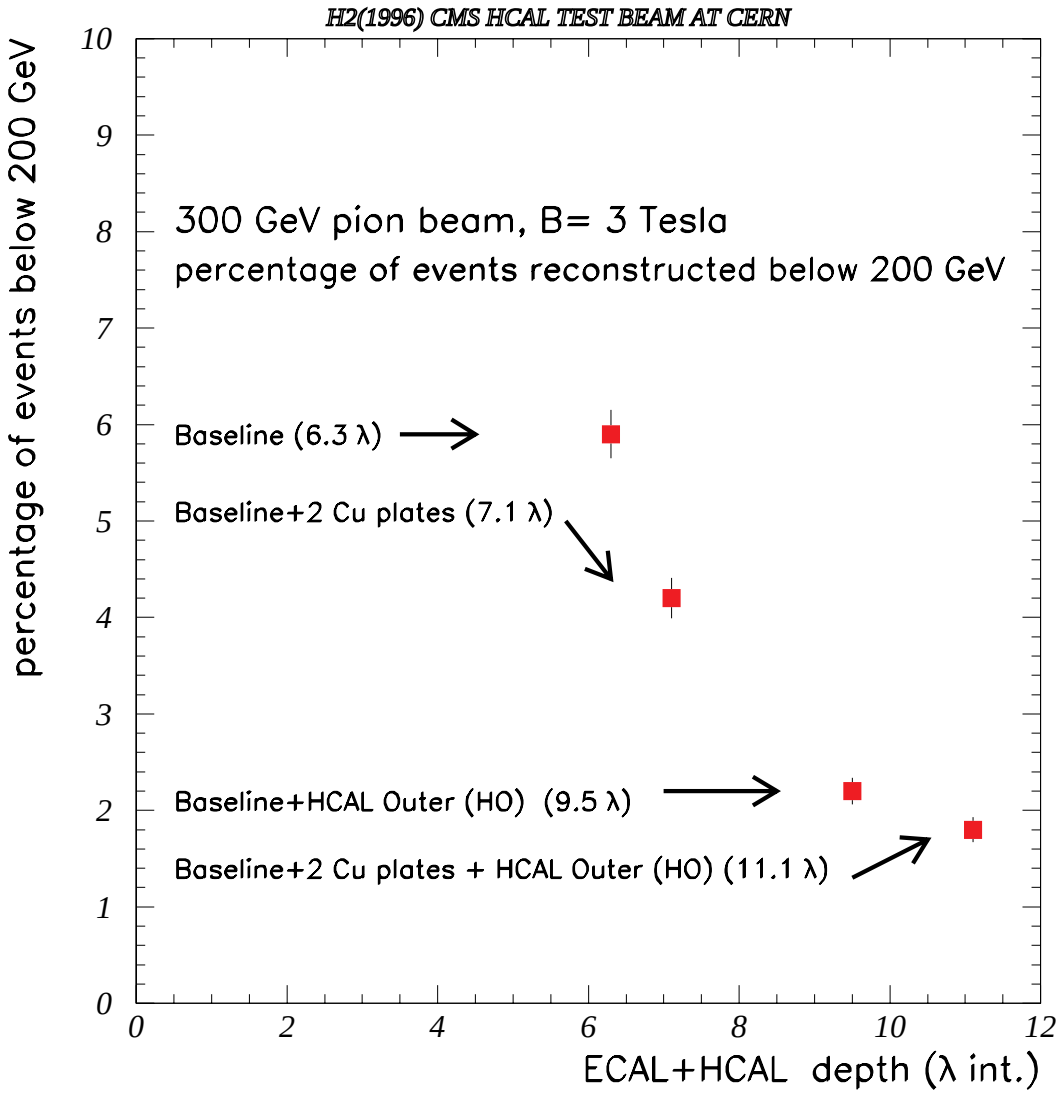

Fig. 1.23: Fraction of 300 GeV pions with reconstructed energy less than 200 GeV (approximately 3 sigma below the mean).

Longitudinal segmentation studies

Fig. 1.24 shows the linearity of HCAL response to pions. The HCAL readout corresponded to Baseline Inner HCAL + HO. The absolute energy scale of ECAL was set using 50 GeV electrons. The absolute energy scale of HCAL was set using 50 GeV pions interacting only in the HCAL. For pions interacting in the HCAL, with a minimum-ionizing signal in the ECAL (circle symbols), the residual non-linearity of response of HCAL for data points between 20 and 300 GeV is less than 10%. However for pions interacting in either ECAL or HCAL (square symbols), the non-linearity is much larger.

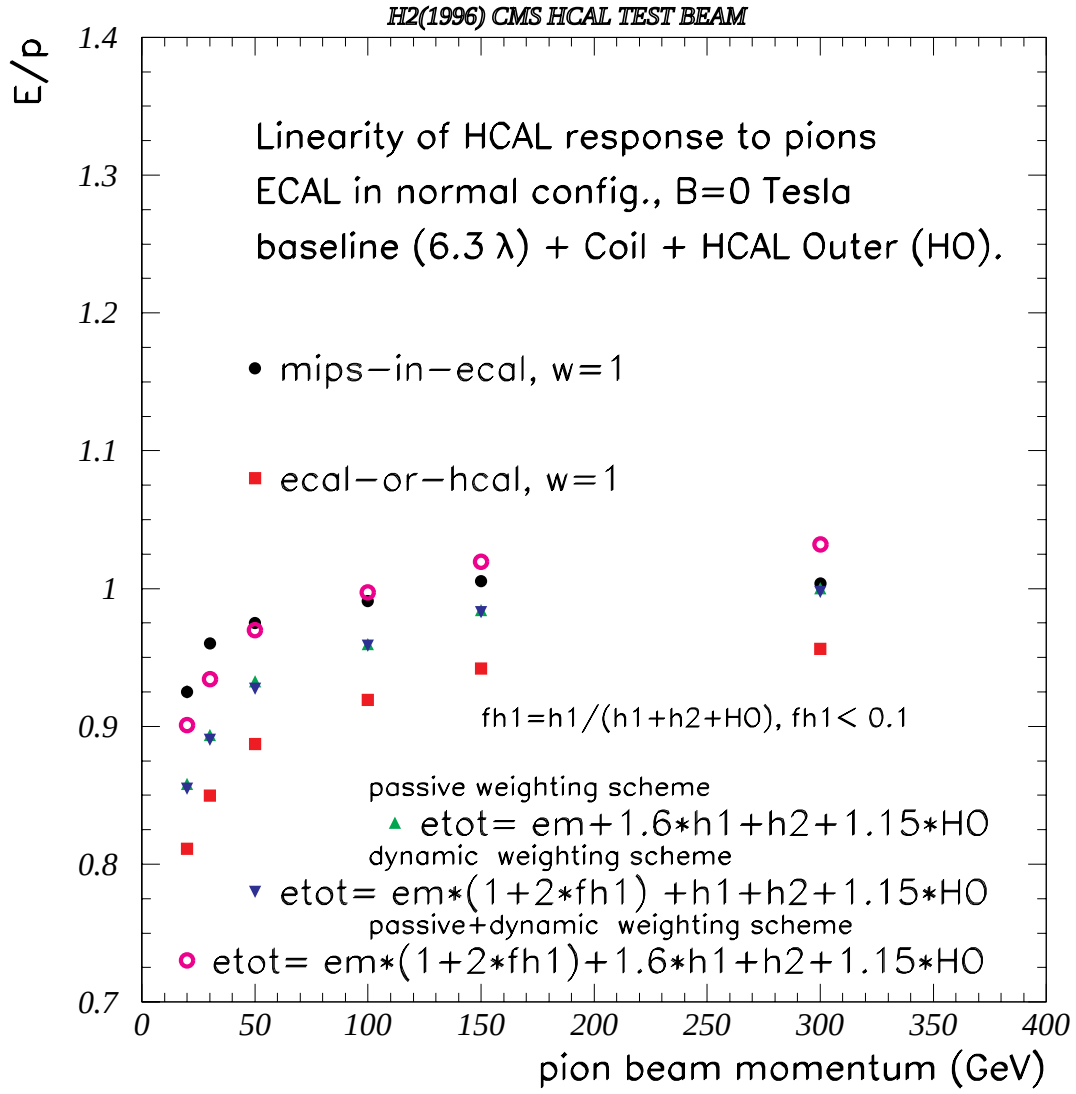

Fig. 1.24: Linearity of HCAL response to pions. The HCAL readout corresponded to Baseline Inner HCAL + HO. The absolute energy scale of ECAL was set using 50 GeV electrons. The absolute energy scale of HCAL was set using 50 GeV pions interacting only in the HCAL.

Fig. 1.25 shows the pion energy resolution of HCAL. For pions interacting only in the HCAL, with minimum ionizing signal in the ECAL, the energy resolution can be parametrized by a stochastic term of 91% and a constant term of approximately 4%. However for pions interacting in either ECAL or HCAL, due to the large e/h of the crystal ECAL, the energy resolution is significantly degraded: The stochastic term increases to 124%.

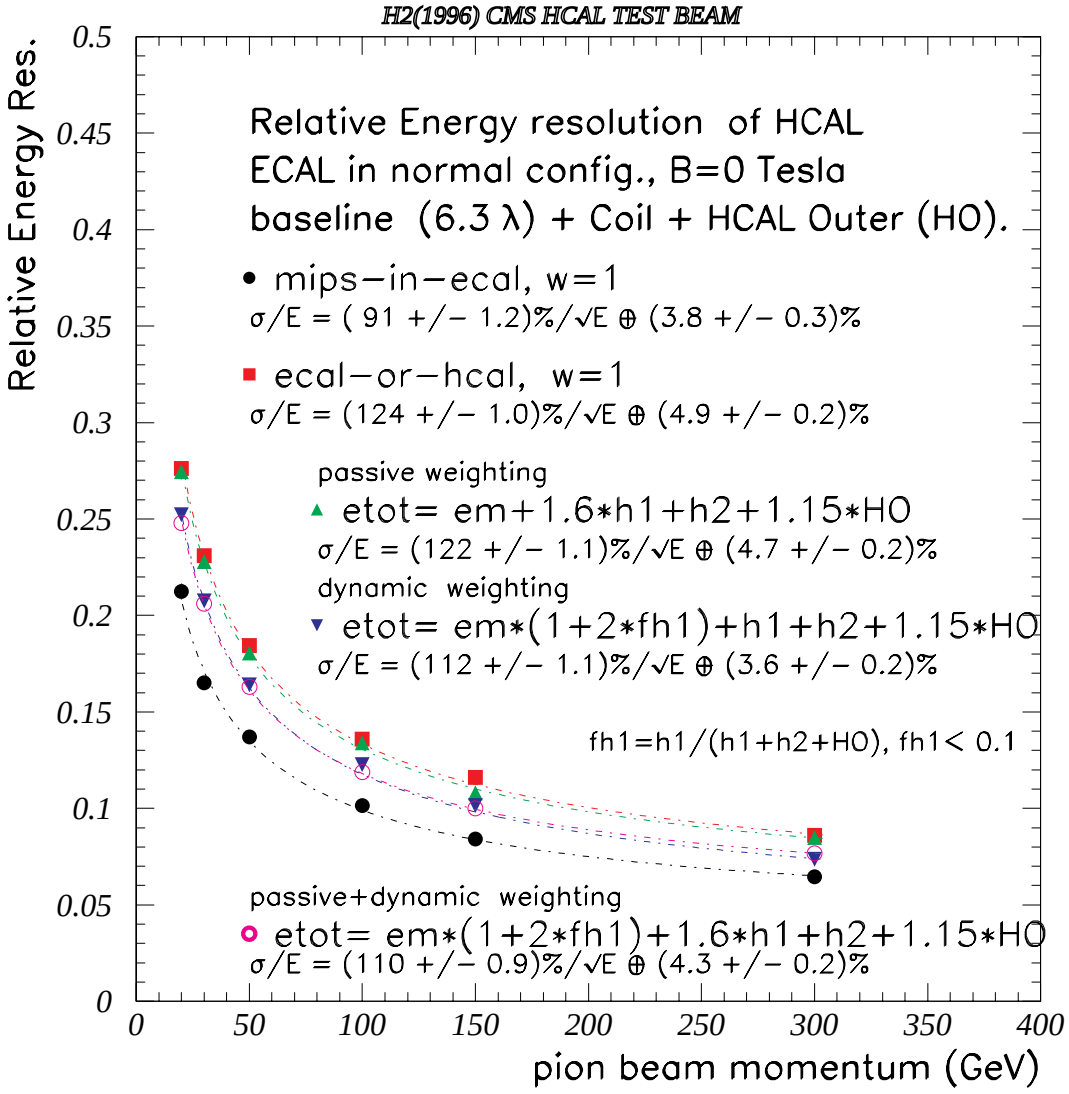

Fig. 1.25: Pion energy resolution of HCAL. The HCAL readout corresponded to Baseline Inner HCAL + HO. The absolute energy scale of ECAL was set using 50 GeV electrons. The absolute energy scale of HCAL was set using 50 GeV pions interacting only in the HCAL.

The Barrel HCAL calorimeter segment inside the CMS solenoid has two distinct longitudinal readouts H1 and H2. In studies done prior to the 1996 H2 beamline tests, no compelling argument to set the optimal partition between H1 and H2 was available. However, the 1996 Test Beam data showed that the optimal partition was that which was most useful in correcting for the large e/h response of the ECAL crystal calorimeter. The present baseline is to have the H1 compartment rather thin, while H2 constitutes the bulk of the inner HB. The reason for this choice is the following. The large e/h of ECAL means that, for hadrons interacting in ECAL, the ECAL response should be increased relative to the electron beam calibration of ECAL. However, this would mismeasure the electromagnetic energy of a jet of particles. Thus, one uses a thin H1 compartment just downstream of ECAL to estimate the energy deposit in ECAL for hadrons and weights it heavily. Thus, the basic function of H1 is to measure the low hadron response of ECAL and correct for it.

We have tested two possible approaches to correct the performance of the combined

ECAL+HCAL calorimeters. In the first approach, called passive weighting, we reduce the non-linearity of energy response and the energy resolution by increasing the weight (α) of the first (H1) HCAL segment. Fig. 1.26 shows the dependence of E/p and σ_E/E as a function of the weight α. Clearly an overweighted H1, $\alpha \sim 1.6$, is optimal.

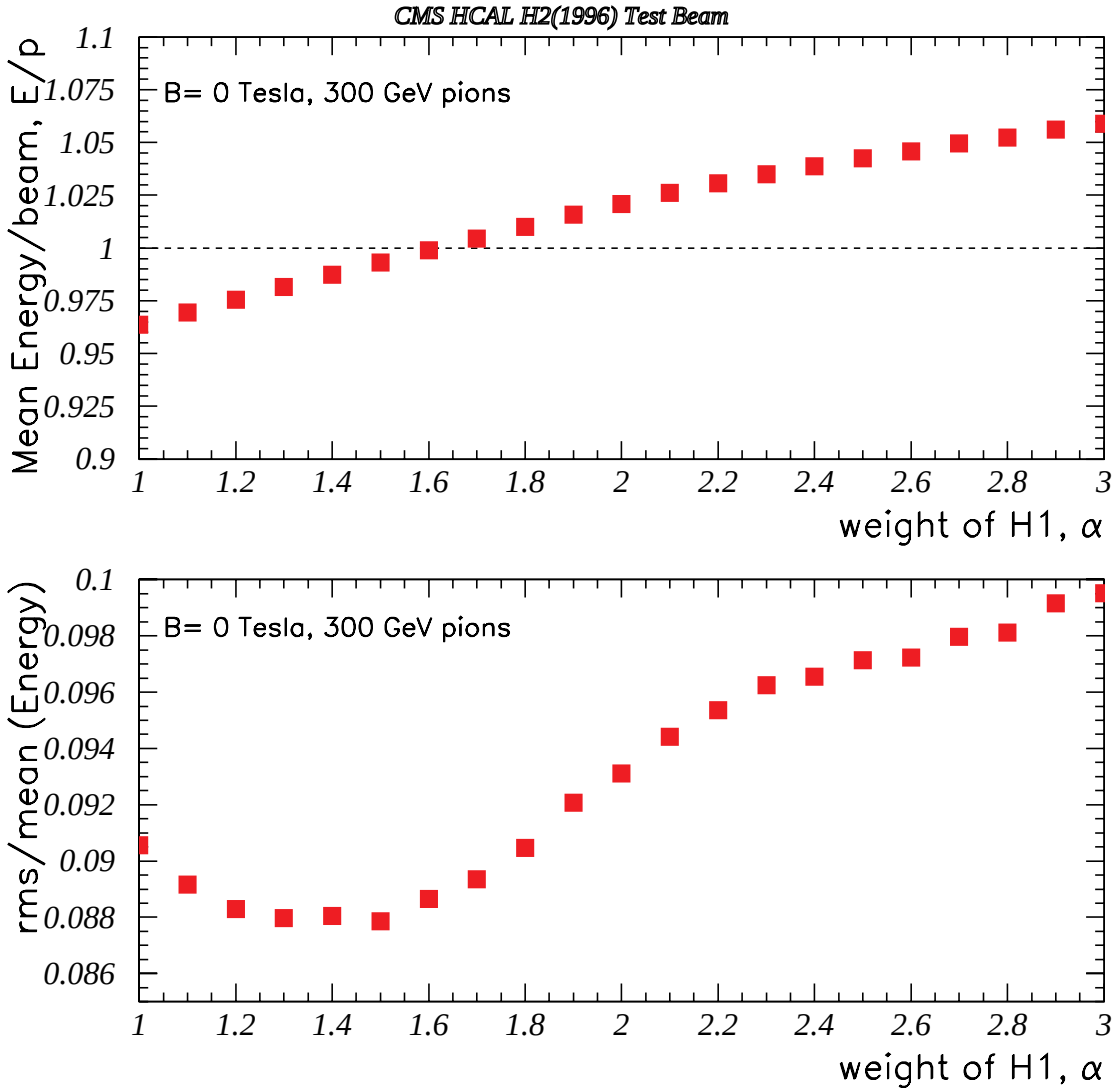

Fig. 1.26: Dependence of the E/p and rms (E)/E as a function of α, the weight assigned to the first HCAL compartment.

In the second approach we use a dynamic (event-by-event) correction. The energy ratio f(H1)=E(H1)/(E(H1)+E(H2)+E(HO)) effectively allows one to correct for the low ECAL response to pions interacting in ECAL. The correlation of total mean energy and f(H1) is shown in Fig. 1.27. Clearly, event by event improvements are indicated. The overall system response to pions can then be represented as the sum in quadrature of a 110% stochastic coefficient and a 5% constant term. One also finds a residual energy nonlinearity of only 10% for pions with energy between 30 and 300 GeV.

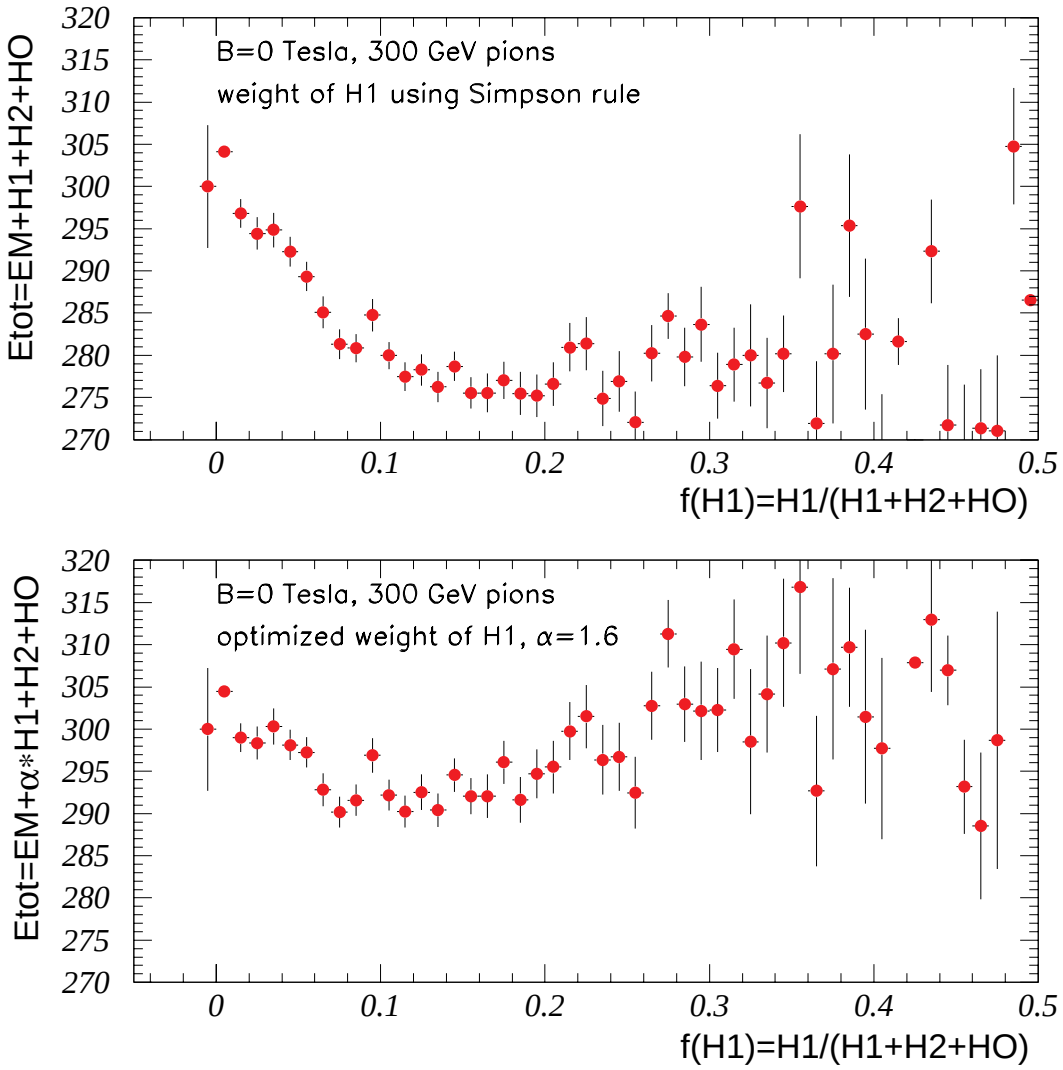

Fig. 1.27: Correlation between the total reconstructed energy, Etot and f(H1)=E(H1)/ E(H1)+E(H2)+E(HO)).

Monte Carlo simulation of the test beam results

Having optimized the depth and longitudinal segmentation of HCAL, it is important to establish a Monte Carlo model of HCAL which will then allow us to extrapolate and to explore other configurations not directly measured in the test beam.

GEANT simulations have been performed for various Test Beam setups. Several hadron shower generators are available in the GEANT framework and have been used in various studies for evaluating calorimeter design in CMS. In order to verify those simulations and to understand their limitations we used GCALOR to simulate the latest 1996 H2 Test Beam setup and take it as a reference to other generators. In the GCALOR simulation, details of ECAL and HCAL Test Beam geometry were implemented. Electronic noise and photo-statistics effects were simulated based on measured distributions of pedestals and electron and muon signals. Energy cut values in the GEANT simulation were set at its default values, 1 MeV for electrons and 10 MeV for hadrons.

The comparison of Test Beam data with GCALOR Monte Carlo simulations illustrates a

good agreement. Fig. 1.28 shows the comparison of average longitudinal profile of 50 GeV pions.

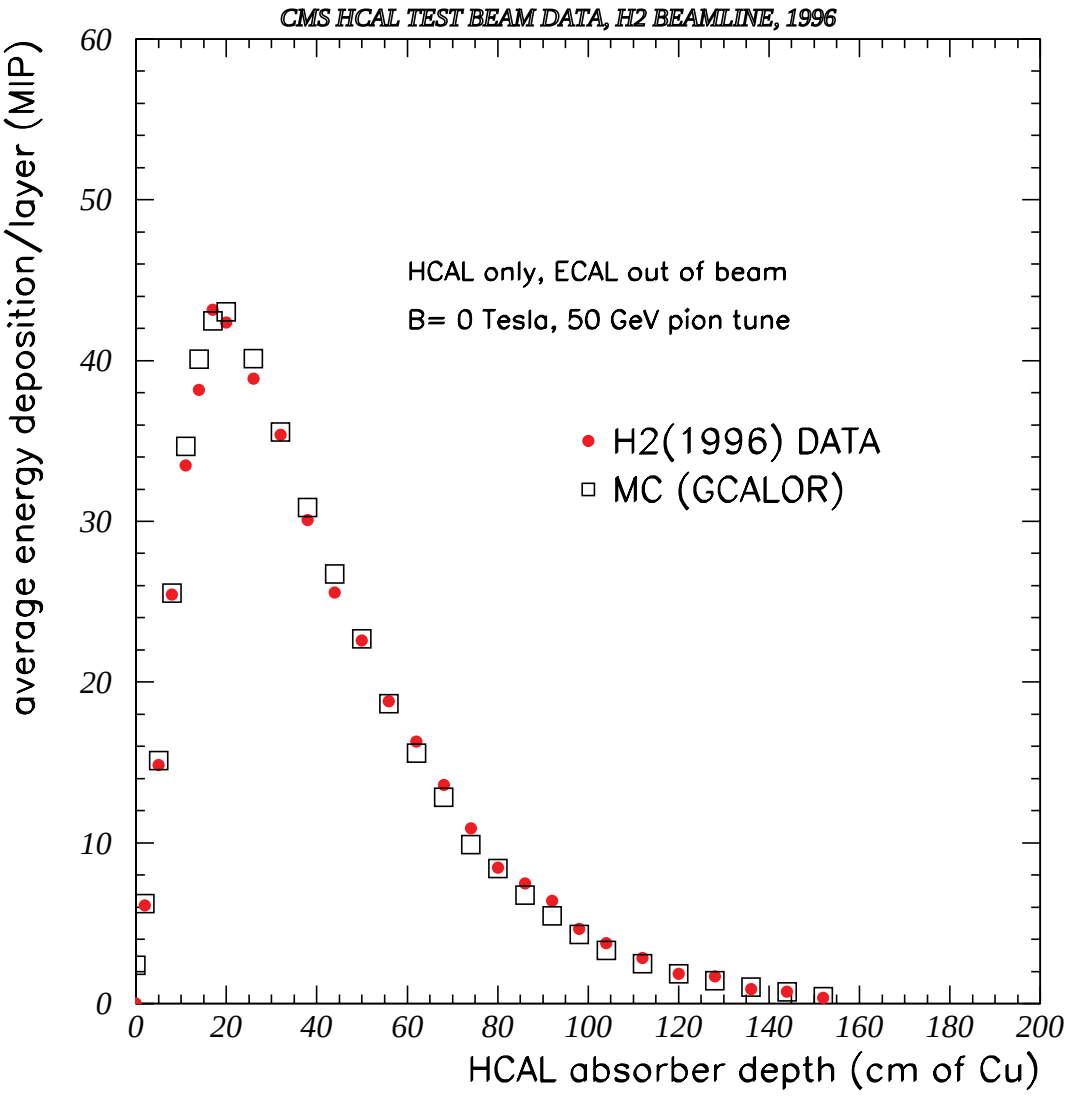

Fig. 1.28: Data vs GEANT comparison of average longitudinal profile of 50 GeV pions.

Fig. 1.29 shows the comparison of linearity of the combined ECAL+HCAL response to pions. Fig. 1.30 shows the comparison between the relative pion energy resolutions of the combined ECAL+HCAL system, after including all experimental effects. The simulated results are in good agreement with Test Beam data.

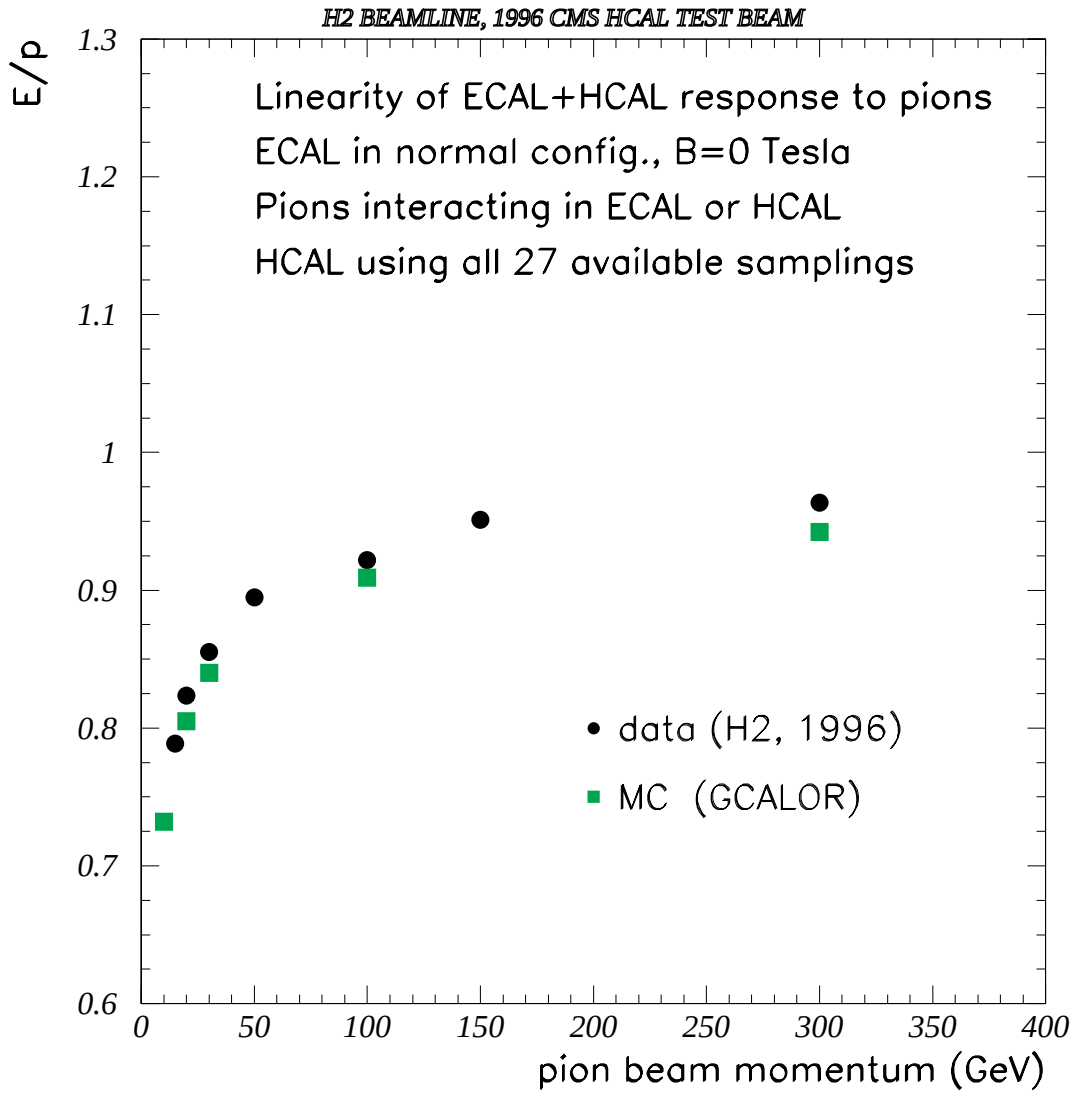

Fig. 1.29: Linearity of pion energy response in HCAL+ECAL combined system (pions interacting in ECAL or HCAL) and comparison with MC simulation.

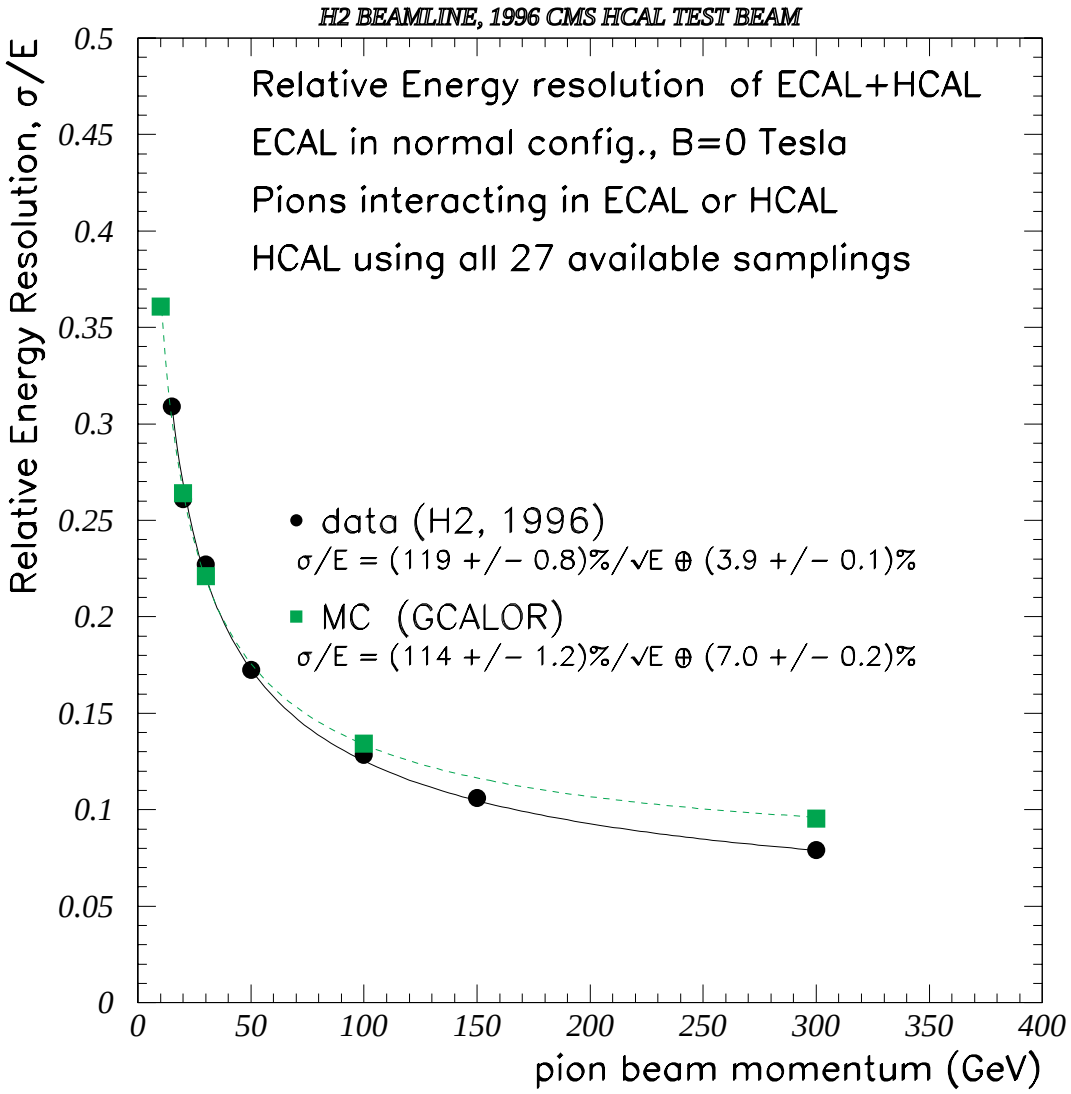

Fig. 1.30: Energy resolution of pions in HCAL+ECAL combined system (pions interacting in ECAL or HCAL and comparison with MC simulation.

Comparison between GCALOR simulation and other GEANT hadron simulators are shown in Fig. 1.31. GHEISHA was used in many of the following studies and gives a somewhat pessimistic resolution, while FLUKA and MICAP show much more optimistic resolution than GCALOR.

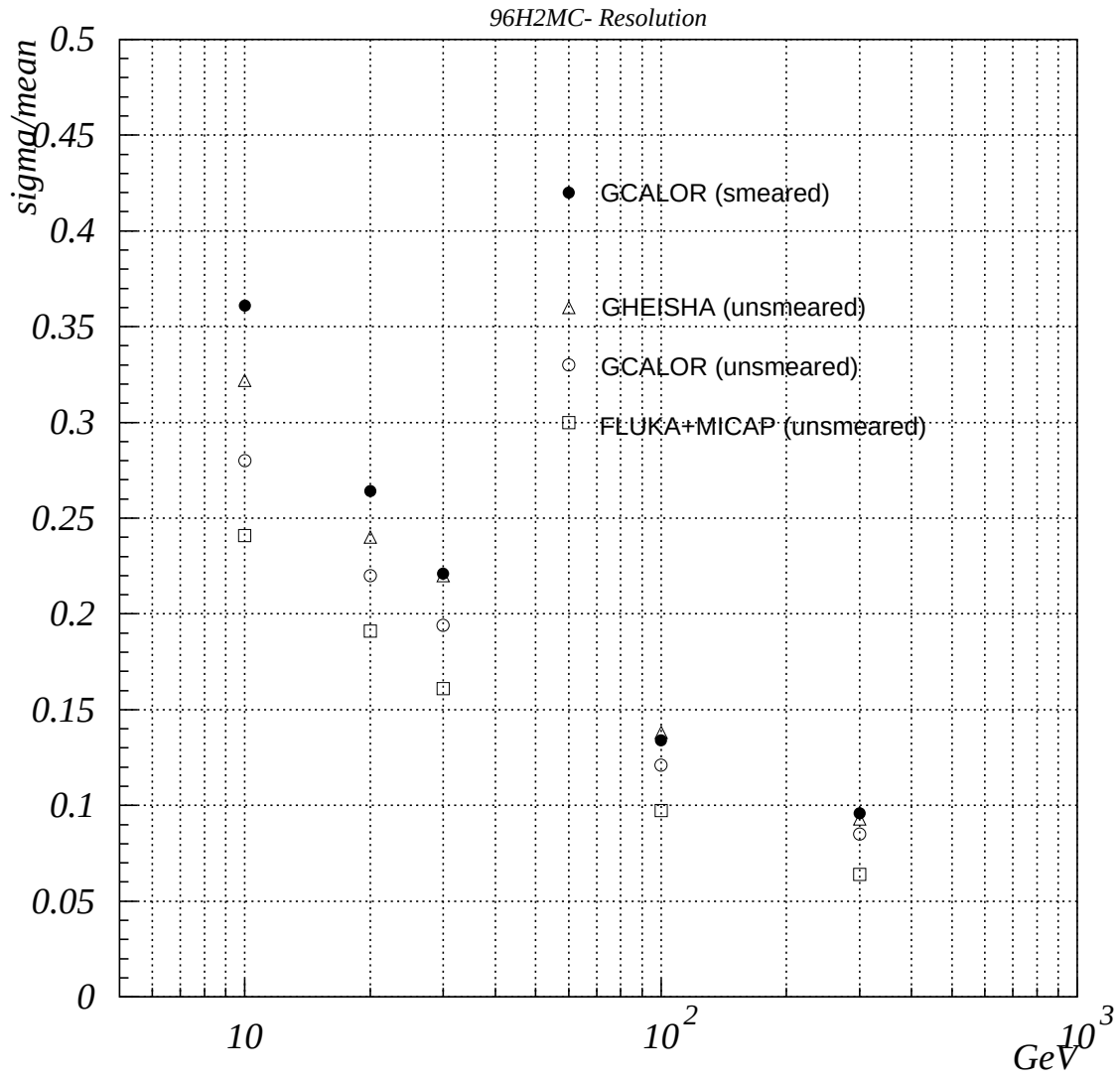

Fig. 1.31: Comparison of GEANT simulation of pion energy resolution of ECAL+HCAL, using various MC simulations (GHEISHA, GCALOR, and FLUKA-MICAP).

Effect of magnetic field on the HCAL performance

The magnetic field changes the light yield of scintillator and affects the particle shower development. This latter effect depends on the field orientation. For a typical collider geometry, the axial magnetic field is parallel to calorimeter plates for the central part of the detector (Hadron Barrel or HB configuration) and is perpendicular to calorimeter plates in the large $|\eta|$ region (Hadron End Cap or HE configuration). One of the primary objectives of the HCAL Test Beam studies was to measure the dependence of calorimeter performance in the presence of perpendicular and parallel magnetic fields.

For the case of the magnetic field lines perpendicular to the scintillator planes (Endcap configuration), we observe an increase of the intrinsic light yield of scintillator of approximately 5%, relative to the case with no magnetic field. This scintillator brightening effect leads to an overall increased response of the calorimeter to muons, electrons and pions and can be well tracked by radioactive γ sources (wire sources). Fig. 1.32 shows the response ratio, relative to B=0 Tesla, of HCAL to pions, electrons and γ source as a function of field perpendicular to the

scintillator planes.

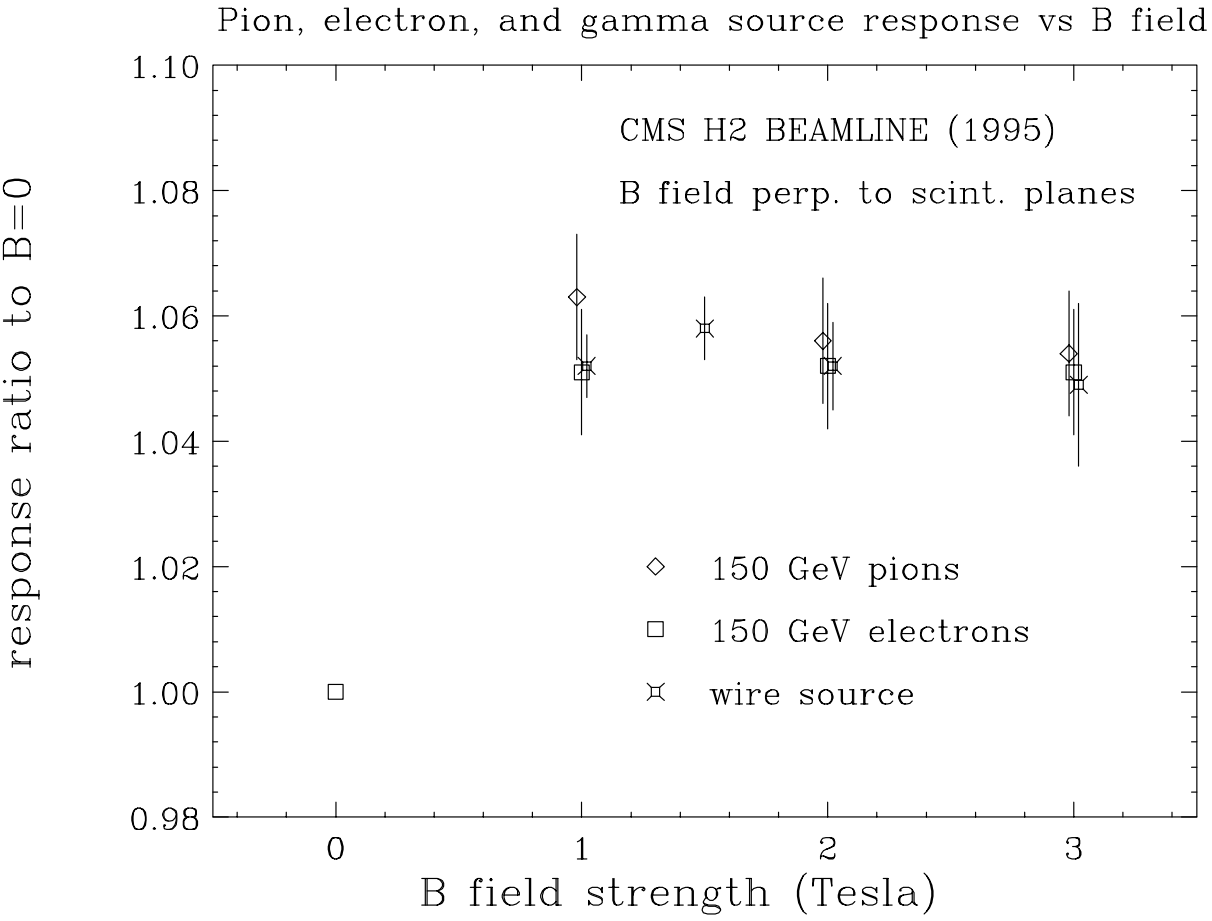

Fig. 1.32: Effect of B field on the average energy response of the tile/fiber calorimeter to pions, electrons (H2 data) and a calibration source. B field lines were perpendicular to the scintillator plates (HE Configuration).

Thus this configuration (B field perpendicular to scintillator planes) causes only increased scintillator light yield (~5%) and does not affect the shape of pion showers.

However, in the case of magnetic field lines parallel to the scintillator planes, an additional geometric effect leads to an increase of response of calorimeter to electromagnetic showers. Fig. 1.33 shows a comparison of average 50 GeV pion shower profiles, as a function of absorber depth. In the beginning of shower development, for pions in a B=3 Tesla field, the scintillator planes have an increased response relative to B=0 Tesla.

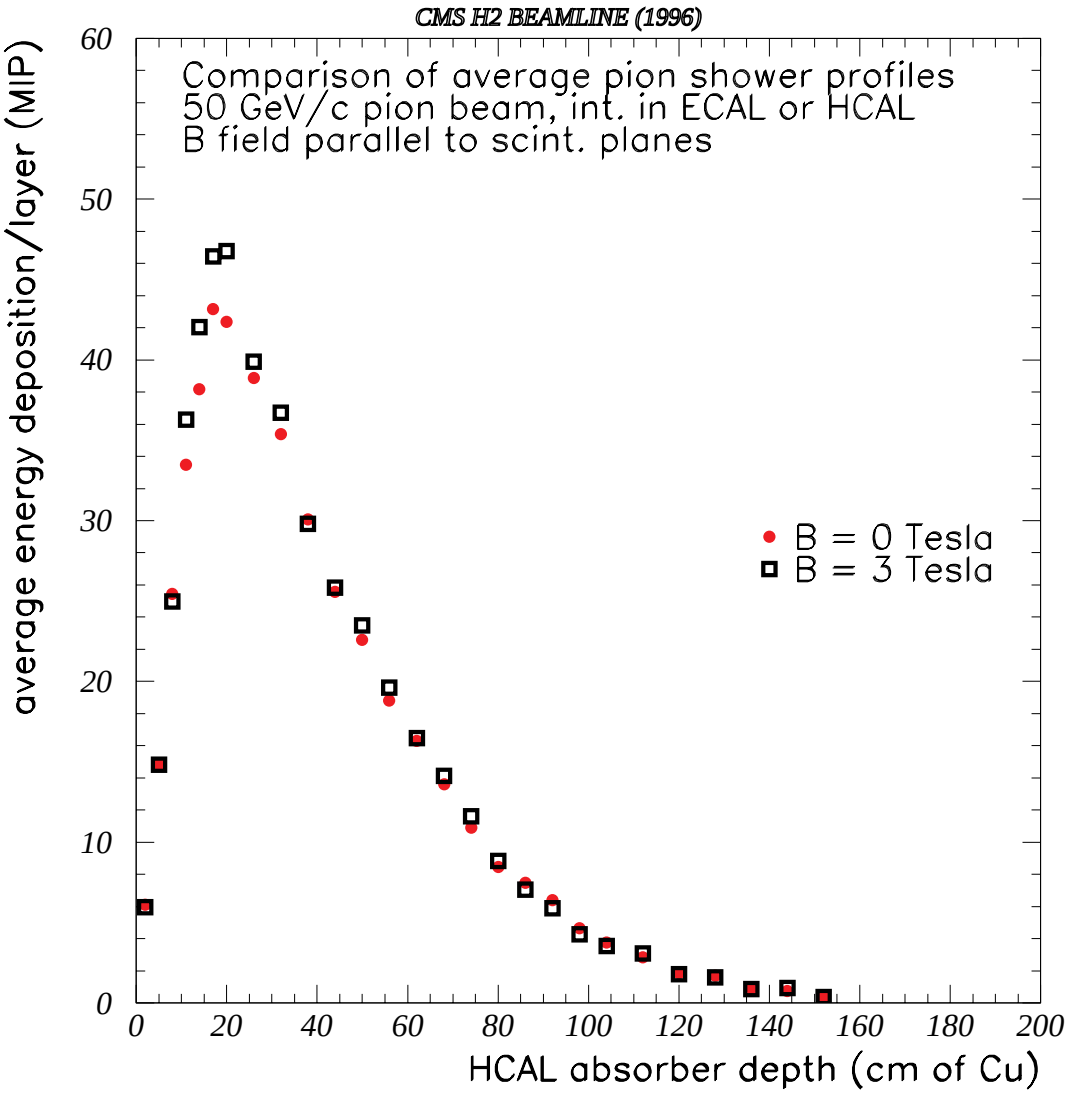

Fig. 1.33: Comparison of 50 GeV pion shower profiles with B=0 and B=3 Tesla magnetic field, with B field lines parallel to the scintillator plates (Barrel configuration).

The average increase of HCAL electron and pion response normalized to muons, as a function of B field, normalized to B=0 Tesla, is shown in Fig. 1.34. The 5% scintillator brightening effect cancels out since is has same effect on electrons, pions and muons.

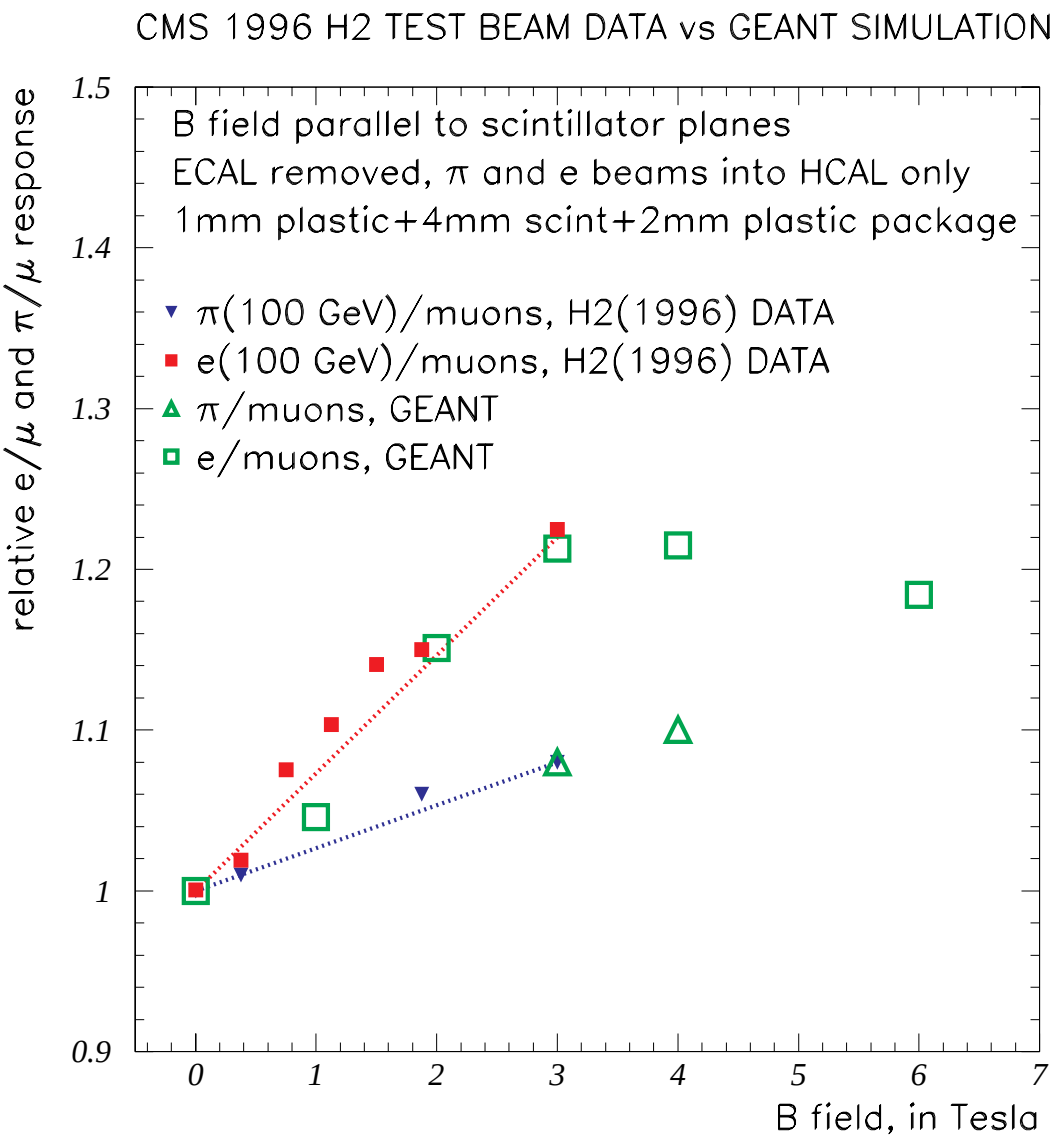

Fig. 1.34: Effect of B field on the average energy response of the tile/fiber calorimeter to pions, electrons (H2 data) (normalized to the muon response) and comparison with GEANT predictions. The ratio of hadrons to muons (lower curve) shows a smaller increase thus indicating the effect is a function of the electromagnetic fraction in the shower.

Subsequent simulation confirmed that this effect was due to the change of path length of low momentum electrons (between 1 and 10 MeV/c) through scintillator layer in a strong field and that only the electomagnetic components in hadronic showers contributed to this effect. Fig. 1. 35 shows a Monte Carlo study of dependence of this effect on the distance between the upstream absorbers and the scintillator packages placed in 9mm gaps between absorbers. The scintillator package consists of a 2mm plastic front cover plate, a 4mm scintillator and a 1mm plastic back cover plate. To set the scale, the radius of electron trajectory in a 4 Tesla field is ~0.8mm per 1MeV/c. Therefore as the scintillator moves away from the upstream absorber, in field parallel to the scintillator plane, low momentum electrons (a few MeV/c) no longer reach the scintillator.

This effect introduces a requirement for placement of scintillator package in gap between absorbers in HB. Since calibration data will be taken in the calibration beam line without a

magnetic field, it will be very desirable to have minimal extrapolation from the calibration beam data (in 0 Tesla) to the CMS HB data (in 4 Tesla). In additon, gravity may push down the scintillator packages toward the front in absorber gaps at the top of HB and increase the HB response, while at the bottom of HB, it would push them toward the back and thus decrease the response. First we choose the tile orientation with the thicker plastic plate (2 mm thick) in front giving a larger distance between scintillator and front absorber. Then by forcing the package toward the back, we can limit the B field effect in HB to less than 2%.

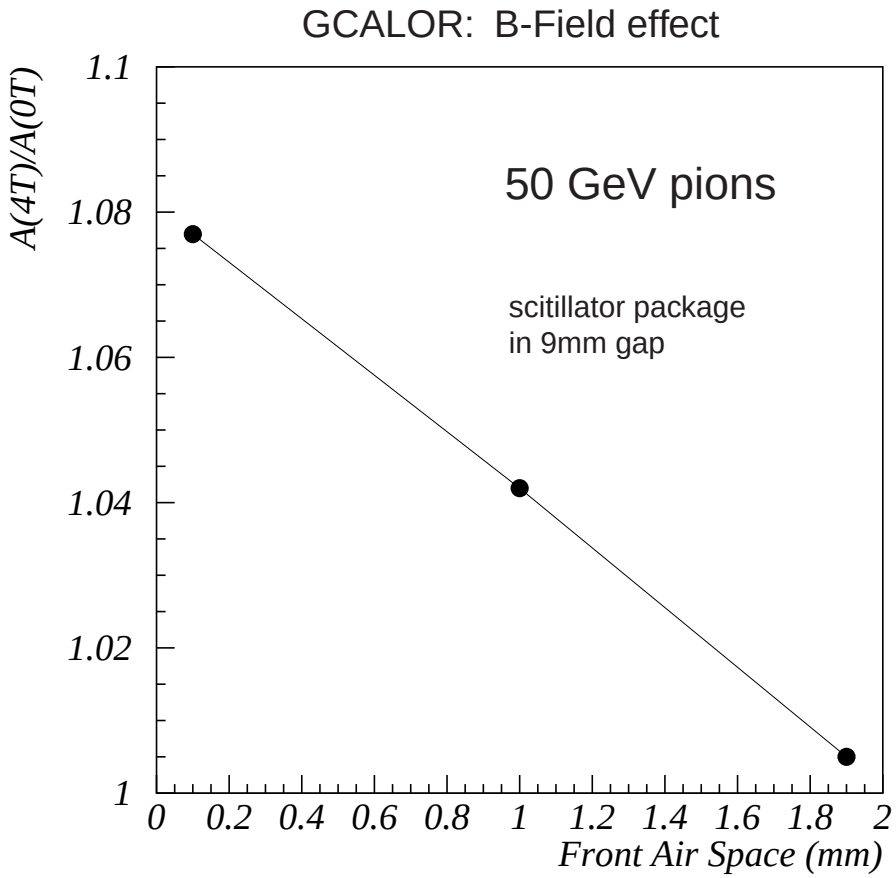

Fig. 1.35: Monte Carlo study on response of HB to 50 GeV pions in 4 Tesla field relative to response in 0 Tesla field with different air space between upstream absorber and scintillator package placed in 9mm gap between absorbers. The scintillator package consists of a 2mm plastic front cover plate, a 4mm scintillator and a 1mm plastic back cover plate.

1.5.3 HF test beam results

Description of HF prototypes

The HCAL group has built and tested two prototype modules for the forward calorimeter (HF). The first, a hadronic detector module, was 135 cm (8.5 nuclear interaction lengths) deep, with an instrumented lateral cross section of about 16×16 cm^2. This area was subdivided into 9 square towers, Fig. 1.36. A tenth tower (T10), neighboring the central row of three, was also instrumented. In total, this module contained about 6000 fibers, with a total length of about 10 km. This calorimeter module was extensively tested in the CERN H4 test beam in 1995. The

results have been submitted for publication in Nuclear Instruments and Methods.[19]

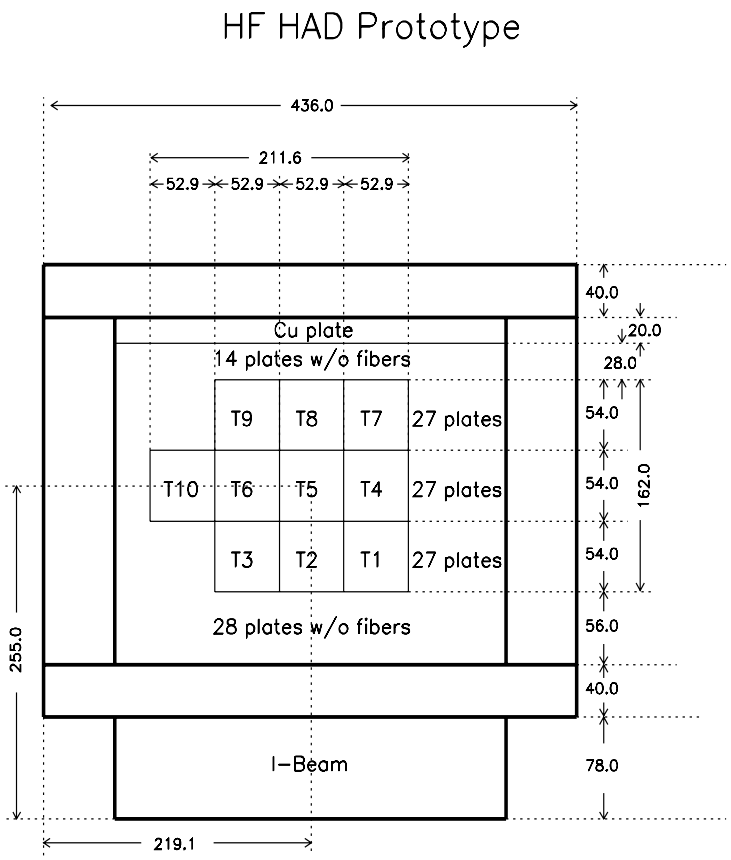

Fig. 1.36: Schematic end view of the HF hadronic prototype. All dimensions are in millimeters. The quartz fibers are embedded in copper absorber. By volume, quartz fibers constituted 1.5% of the detector.

The second, electromagnetic module had the same lateral structure as the hadronic module. It was about 34 cm (~23 radiation lengths) deep. The fibers emerged from the front face (towards the beam) and were aluminized at the open, downstream end. By mounting the readout in front of this detector, it could be joined flush to the hadronic module. This calorimeter was also tested, in the same H4 beam in 1996, both in stand-alone mode and in combination with the hadronic module. Some of the results are presented in the following.

During the beam tests, the calorimeter modules were exposed to electrons, pions, protons and muons of various energies, ranging from 8 GeV to 375 GeV. Dedicated tests were done to study various options for the location of the photomultiplier tubes, and to study pickup and cross talk in the fiber bundles emerging upstream from the electromagnetic module.

HF hadronic prototype results

The light yield of this type of calorimeter is extremely small. We measured it to be less than 1 photoelectron per GeV. Fluctuations in the number of photoelectrons constituting the signals completely determine the electromagnetic energy resolution. In Fig. 1.37, this resolution is shown as a function of energy, for electrons from 8 GeV to 250 GeV. The data show no measurable constant term. When the calorimeter was read out by our standard PMT's (Philips

XP2020), the resolution was found to be: $\sigma(E) = 1.37\sqrt{E}$, commensurate with a light yield of 0.53 photoelectrons per GeV. When the same type of PMT was equipped with a quartz window, the signal increased by about 65%, to 0.87 pe/GeV, due to the larger fraction of the Cerenkov light that was detected. The energy resolution improved to $1.07\sqrt{E}$, reflecting smaller fluctuations in the larger number of photoelectrons.

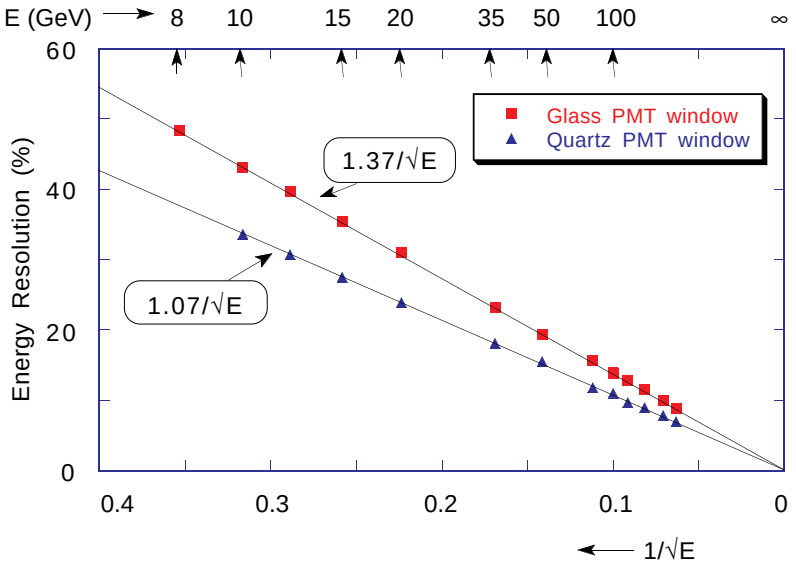

Fig. 1.37: The energy resolution for electrons as a function of electron energy, for readout with a XP2020 PMT (glass window) and with a XP2020Q (quartz window).

Although the light yield is extremely small, it is not a limiting factor for the resolution of the objects for which this calorimeter is intended: jets and energy flow at the 1 TeV level. With regular glass PMT's (the UV component of the signal is vulnerable to radiation and therefore will not be used in practice), we expect signals of about 500 photoelectrons at 1 TeV. Statistical fluctuations in that number amount to 4.5%, which is only a small contribution to the observed single particle resolution (10-12%) and is well below the intrinsic jet resolution.

The energy resolution for hadrons is shown in Fig. 1.38. Because of the asymmetric response function, the rms standard deviations are given, as opposed to the electron data which represent the results of Gaussian fits. The full circles show the energy resolution for pions, as a function of energy. The contribution from photoelectron statistics to these resolutions is represented by the triangles, and the *intrinsic resolution* (the squares) denotes the experimental resolution obtained after subtracting the contribution of photoelectron statistics in quadrature.

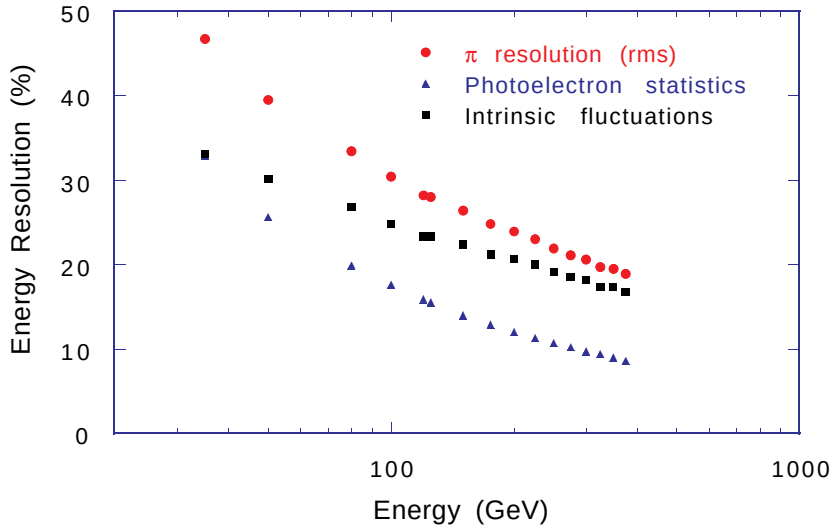

Fig. 1.38: The hadronic energy resolution (σ_{rms}) as a function of energy. The circles represent the raw data, the triangles the contribution of fluctuations in the number of photoelectrons, and the squares are the contributions from other sources.

These results show that the contribution of photoelectron statistics, although substantial in the low energy regime, rapidly diminishes at high energy and that therefore a large increase in the number of fibers would only have a miniscule effect on the energy resolution in the TeV regime. The results also show that the intrinsic resolution scales with the logarithm of the energy.[20]

The hadronic signals from this type of calorimeter are strongly dominated by the electromagnetic shower core. Apart from the asymmetric line shape already mentioned, this has several other consequences. First, the energy dependence of the average energy fraction carried by the EM shower component makes the hadronic response intrinsically non-linear. Second, the shower profiles derived from the Cerenkov signals are much narrower and also shallower than the profiles from detectors based on a measurements of *dE/dx*. This reflects the fact that the EM shower component is concentrated in a narrow core around the shower axis and that π^0 production is limited to the first 4-5 interaction lengths in shower depth.

The signal for pions was measured relative to electrons and results are shown in Fig. 1.39. Since the available electron energies were less then 250 GeV, we extrapolated the electron energy dependence for higher energies. The intrinsic e/π of HF is rather nonlinear. We will use the relative normalizations of the longitudinal segments to require e/π = 1 at 1 TeV.

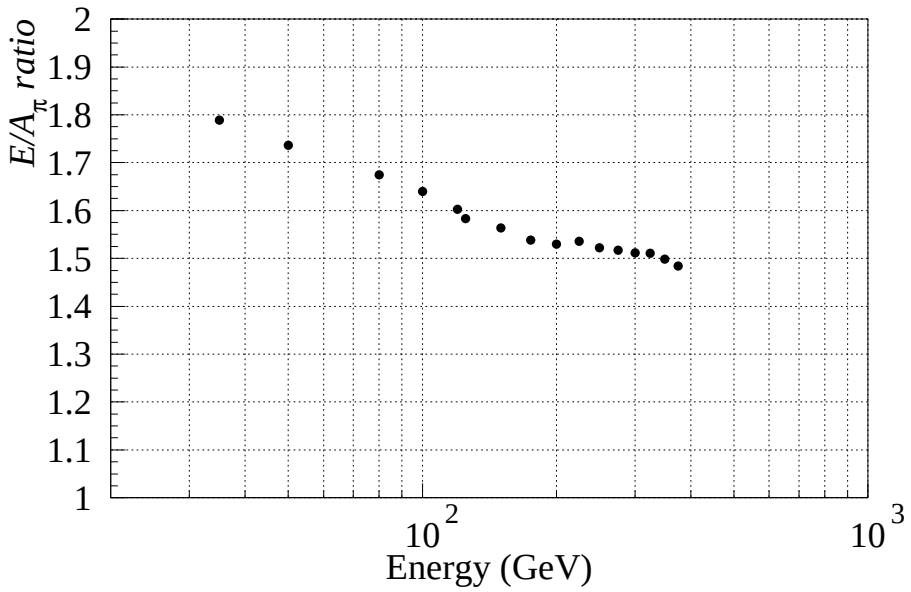

Fig. 1.39: e/π ratio of the hadronic module.

As with all fiber calorimeters, this detector is intrinsically very hermetic. There are no discontinuities in the calorimeter response at the boundaries between the towers. This is illustrated in Fig. 1.40, which shows the results from a scan with a narrow particle beam (80 GeV electrons) across the surface of the calorimeter. The response is uniform to within a few percent over the entire calorimeter surface. This figure also gives a good impression of the narrow lateral profiles of the showers in this calorimeter.

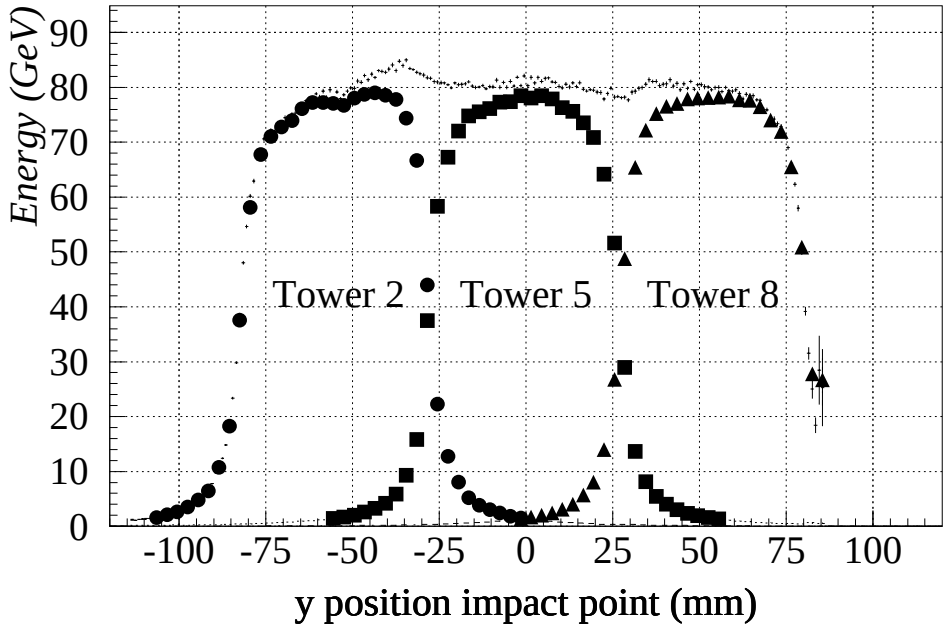

Fig. 1.40: The average calorimeter response to 80 GeV electrons as a function of their impact point. The results of a vertical scan in steps of 0.4 mm across the face of the detector. Shown are the average total calorimeter signal and the average signal in three individual towers as a function of electron impact position.

HF hadronic and electromagnetic prototype results

The energy resolution for electrons was found to be $\sigma/E = (155 \pm 1)\%/\sqrt{E} + 6 \pm 0.2\%$. The larger constant term has its origins in a reflection non-uniformity of the mirrored ends of the electromagnetic section which was about ± 10%. The hadronic energy resolution is compatible with that of the single hadronic section at high energies (E > 300 GeV).

HF signal timing measurements

We measured the time structure of the calorimeter signals, Fig. 1.41. This calorimeter is an extremely fast device. The entire charge produced by the Cerenkov photons is collected in about 5 ns, and this time is limited only by the transit time of the PMT. Typically 85% of the light, is reflected if the far end of the fibers are mirrored.

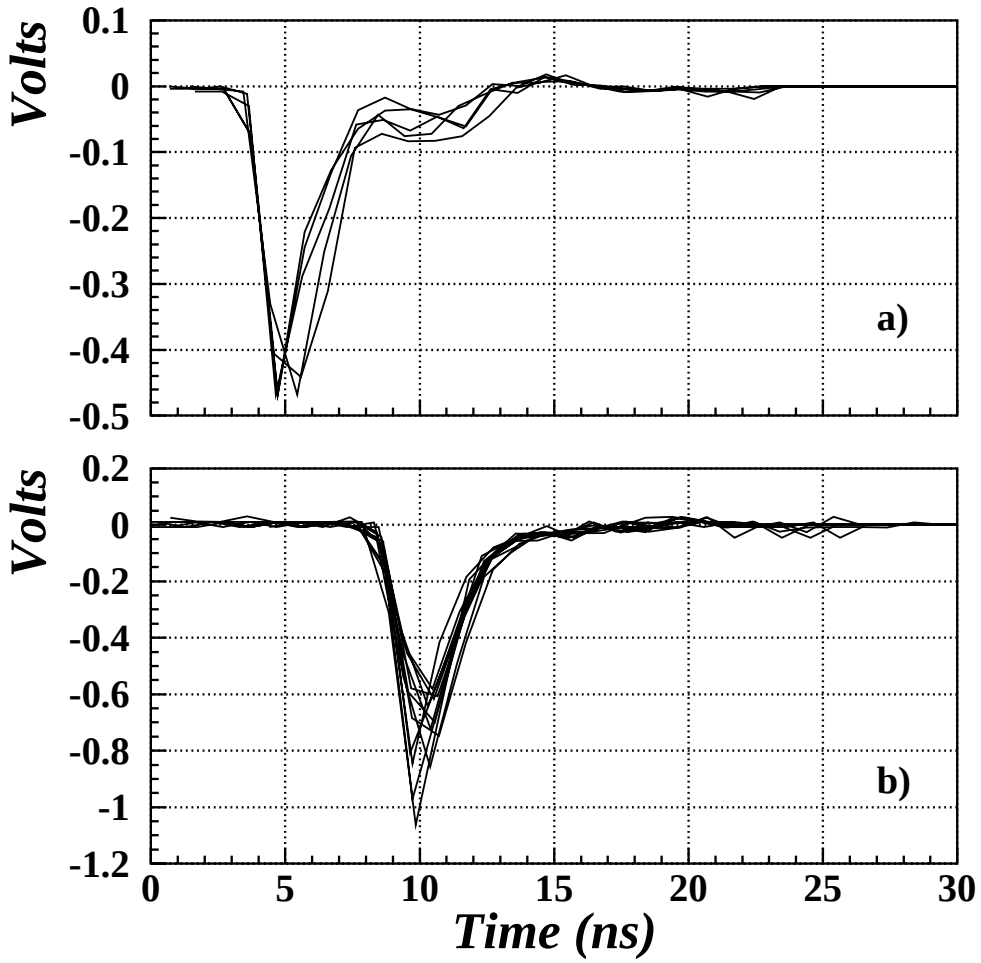

Fig. 1.41: The time structure of a typical electromagnetic shower detected in the detector before a) and after b) the mirrors were removed from the open end of the fibers. Two components in the top plot represent the Cerenkov light emitted in the forward and backward directions, respectively.

Quartz fiber attenuation length measurements

The longitudinal uniformity of the hadronic prototype equipped with quartz core and flourine doped clad fibers was measured with 80 GeV electrons entering the detector sideways (90 degrees) at various positions. In this way, the light attenuation in the fibers can be

measured. In these measurements, the signal observed from the front and from the back of the detector differed typically by less that 5%. The attenuation length in these fibers is thus very long, at least 15 m.

Optical pickup measurements

The expected rate of charged particles, with β greater than β_{min} and arriving at the HF front face may range from 0.1 to 1 per cm^2 and crossing.

Our earlier designs called for a configuration where the EM section would have its fibre bundles emerge from the front (close to the interaction point). During the 1996 test beam periods we tested this readout scheme by exposing straight bundles of fibers at different angles (90 and 45 degrees) behind various absorbers (air, polyethylene and iron).

Using GEANT we have simulated the experimental setup and found that, on average, about 1.6 charged particles (electrons and positrons) per event come with β greater than β_{min} and forming an angle of 45 ± 10 degrees with the bundle. This is equivalent to 0.02 cm^{-2} "Cerenkov particles", which is about an order of magnitude lower than the expected fluence at the HF entry face, per crossing, for the nominal LHC luminosity. Notice that, when traversing the bundle, each particle crosses, in average, 21 fibres.

Therefore, in our current design all the fibers are situated in the back of the copper absorber ($\approx 10\ \lambda$) and are bundled only (to minimize the cross section) at the entrance of the air core light guides, near the PMTs, at a space location where the expected charged particle flux is several orders of magnitude smaller than at the HF front face.

1.5.4 HB/HE Simulation

Test beam data have been extensively used to study a response of the combined ECAL and HCAL system to single particles with various HCAL configurations in order to optimize the configuration. Normalized to this test beam data, GEANT simulations with detailed descriptions of the CMS detector geometry have been performed to extend the study to the CMS environment for further design optimization.

For good jet and missing E_T measurements the calorimeter has to be as hermetic as possible. Any holes due to cracks and dead material, or lack of stopping power i.e. insufficient depth for showers seriously spoil the measurements. We have made special attempts to reduce the energy leakage and keep a uniform response in the hadron calorimetry over a wide range of rapidity. In the following we will describe our GEANT[21] simulation and results from the simulations on shower leakage and the calorimeter response to single hadrons and jets in the rapidity range $|\eta|<3$.

Simulation Program

The hadron calorimetry simulation was performed within the framework of the CMS general simulation program CMSIM. In addition to detector simulation with GEANT, CMSIM has interfaces to physics event generators and event reconstruction programs including a clustering code for jet finding.

The geometries used for the studies reported here are shown in Fig. 1. 42. TDR-0 corresponds to the baseline design and TDR-2 corresponds to the baseline plus two additional layers in HB. The ECAL consists of 23cm long crystals followed by a 2cm aluminum plate, a 4cm aluminum layer and a 2cm steel plates which represent respectively the crystal support

structure, cooling, electronics, cables and a back plane in the ECAL mechanical structure. The HCAL consists of layers of a 5.0cm (7.9cm in endcaps) copper absorber followed by a gap with a scintillator package. The first and last absorbers are made of 7cm steel plates. Outside the solenoid two layers of HO are implemented in the muon system. The gap between HB and HE is 12cm wide and filled with 'cable material' (density 1.88g/cm3) for the cables and pipes of the inner detector. In the endcap a preshower detector, made of 1.68cm lead with sampling Si layers, is placed in front of the ECAL. GHEISHA is used for hadron shower generation and energy cut values in GEANT are set to 1MeV for electrons and photons, and 10MeV for hadrons.

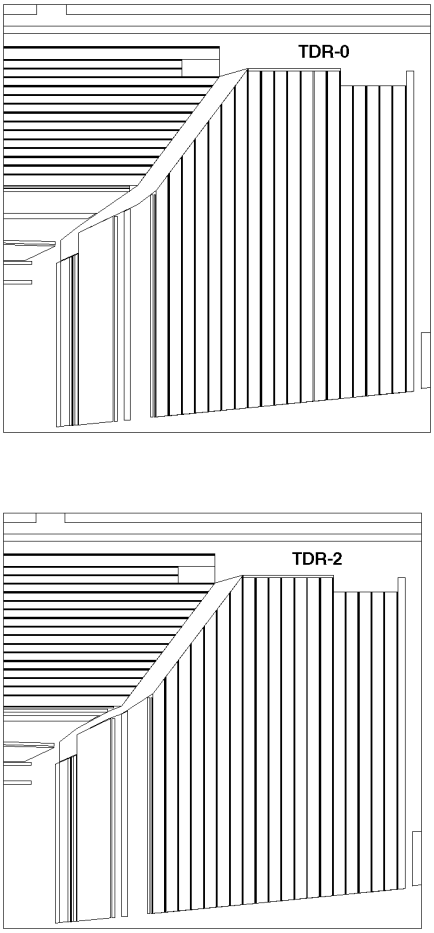

Fig. 1.42: Geometries in GEANT simulation: the baseline (TDR-0) and the baseline plus two layers in HB (TDR-2).

To study the response to jets we created shower libraries. A shower library stored the calorimeter system (ECAL+HCAL) response to single particles in 18-rapidity × 6-energy bins for each HCAL configuration. Three thousand events were generated in each bin.

Single particle response

The expected resolution in measurements of single pions energies between 4 and 300 GeV is shown in Fig. 1.43 for TDR-0. At a given incident energy the resolutions vary very

little (<5% at 4GeV and <2% at 300GeV) in a wide rapidity range up to 2.8 and degrade beyond $|\eta|=2.8$ rapidly because of shower leakage through the inner edge of HE. (Note that the forward calorimeter (HF) was not included in this study.) Around the boundary between HB and HE at $|\eta|=1.3\sim1.4$ the resolution degrades by 1-2% due to energy loss in the 'cable' material in the crack region, and energy leakage through the relatively thin part of the calorimeter in the region of the crack. In the thinner or in the cracks region main issue is however not the Gaussian resolution but rather the population of the low energy tail. Overall, the single particle resolution is, by design, rather flat over the entire region $|\eta|<3$.

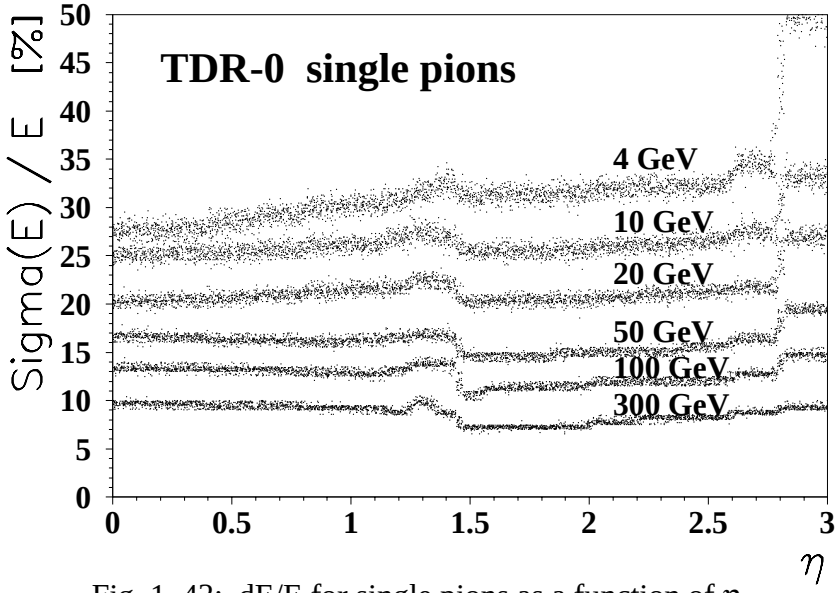

Fig. 1. 43: dE/E for single pions as a function of η.

The resolution for TDR-2 can be inferred from test beam data. At the GEANT simulation level the Gaussian resolution for TDR-1 is nearly identical to TDR-0. The simulated energy distributions for TDR-0 and TDR-2 are compared in Fig. 1.44 for 300 GeV single pions. Low energy tails are small in both cases and with two additional layers (TDR-2) an improvement can be seen in the central region η~0.0-0.3 and in the crack region η=1.3-1.4.

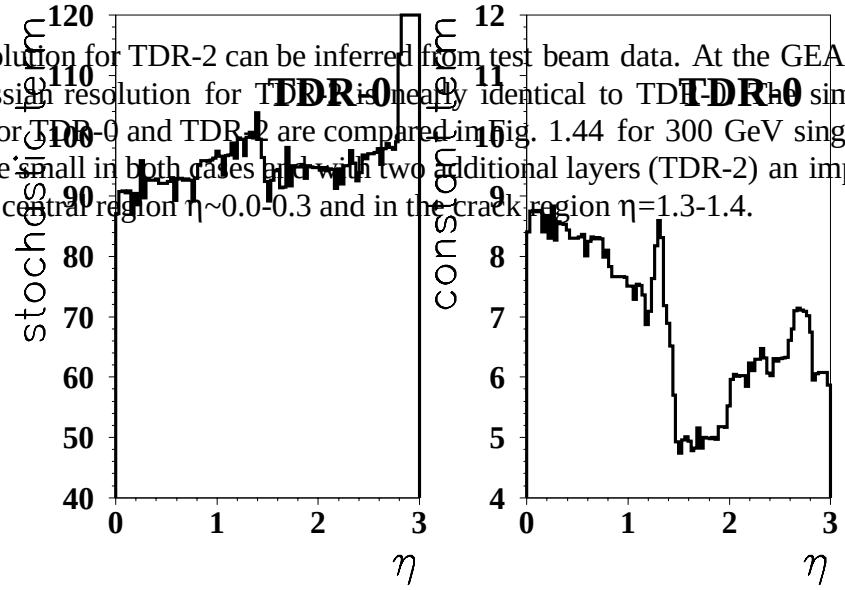

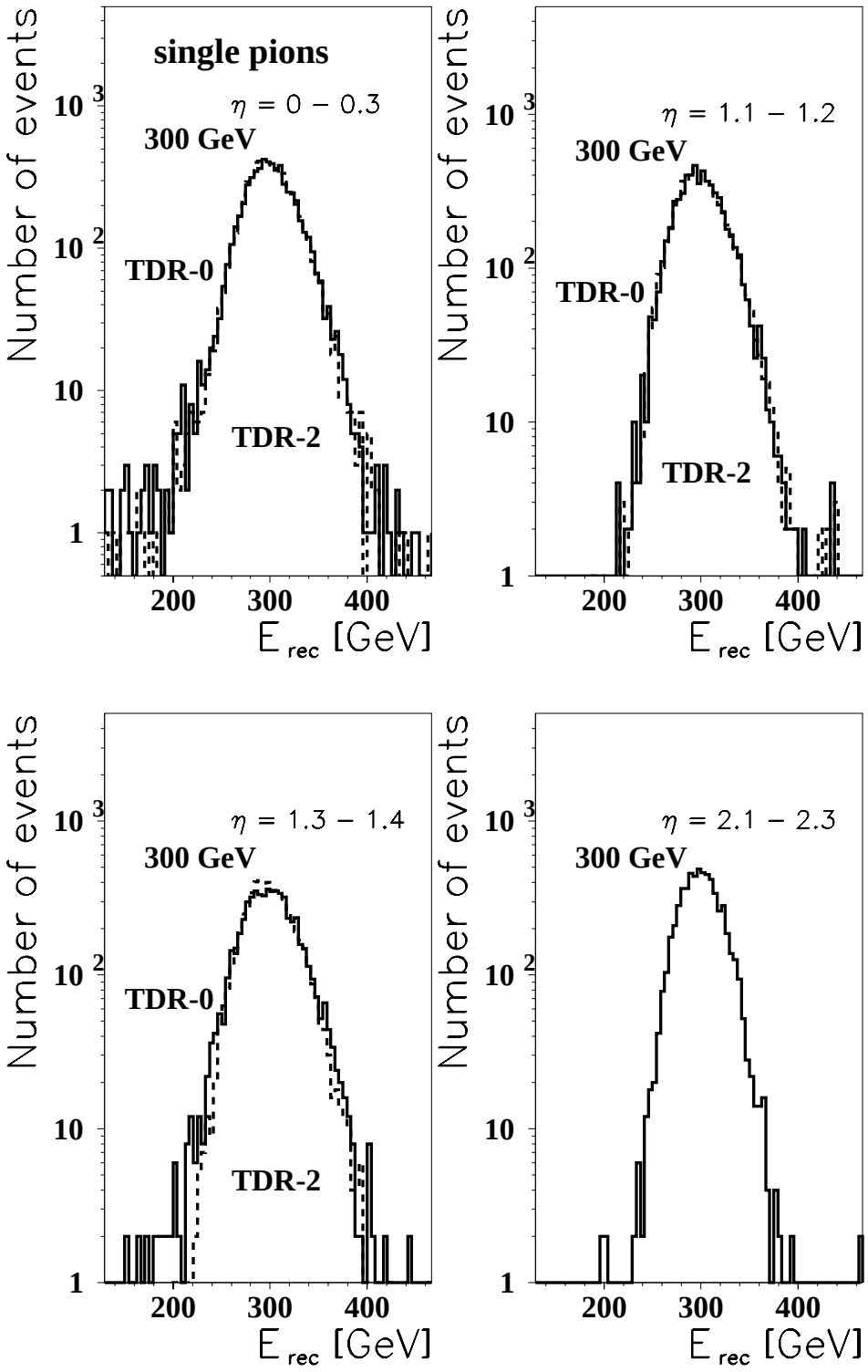

Fig. 1.44: Reconstructed energy distributions for 300 GeV pions.

Jet response

The expected Gaussian resolution for jet E_T measurement fitted over the E_T 30 to 300 GeV range with a fixed cone size of $d\eta \times d\phi = 0.74^2$ is shown in Fig. 1.45 for TDR-0. The degradation at the HB-HE boundary is less than 1%, and again the resolution is smooth and monotonic for $|\eta| < 3$.

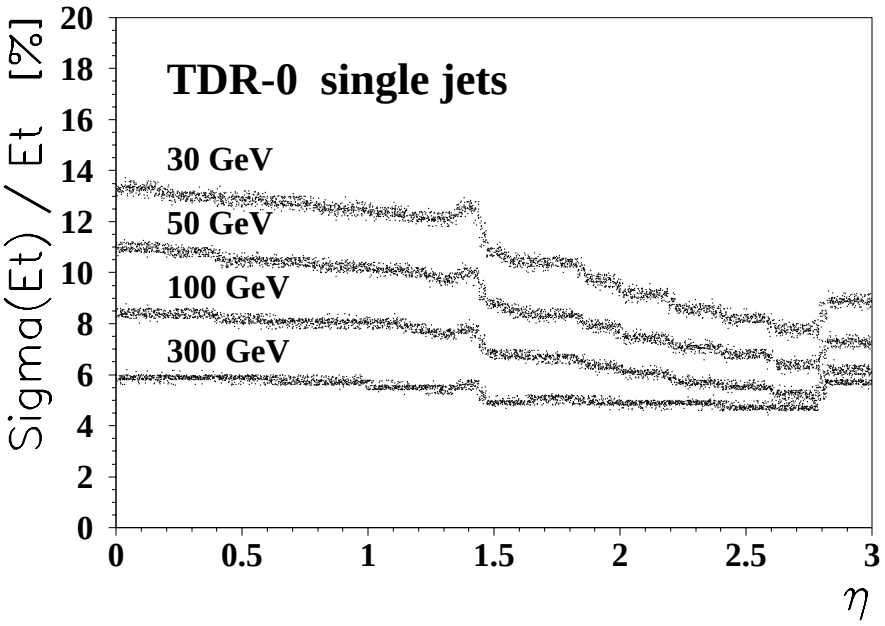

Fig. 1. 45: Jet energy resolution of HB and HE.

Reconstructed jet E_T distributions are shown in Fig. 1. 46 in the central part at η =0.1 for TDR-0 and TDR-2. Fig. 1. 47 shows reconstructed E_T distributions for E_T = 300GeV at four different rapidities.

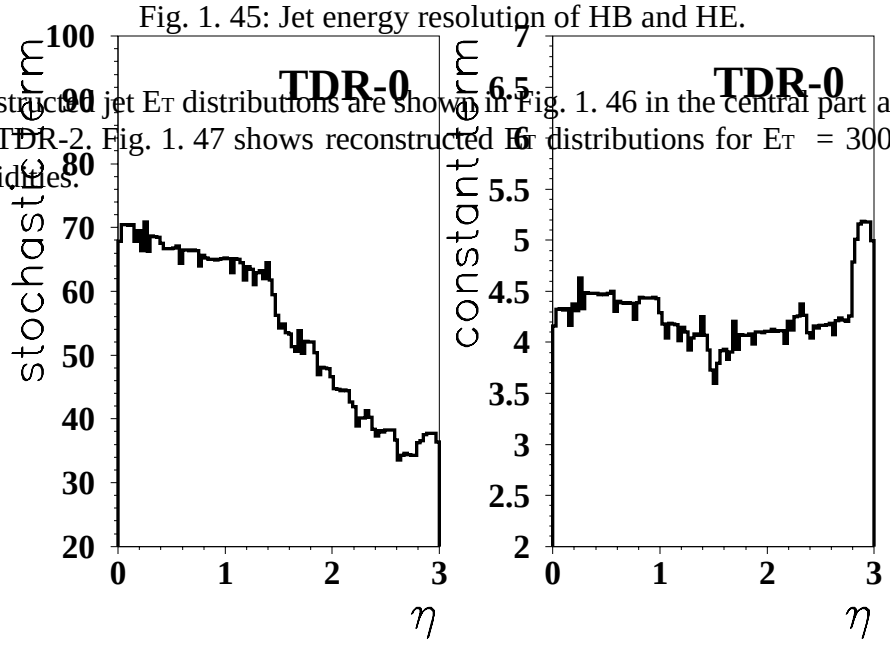

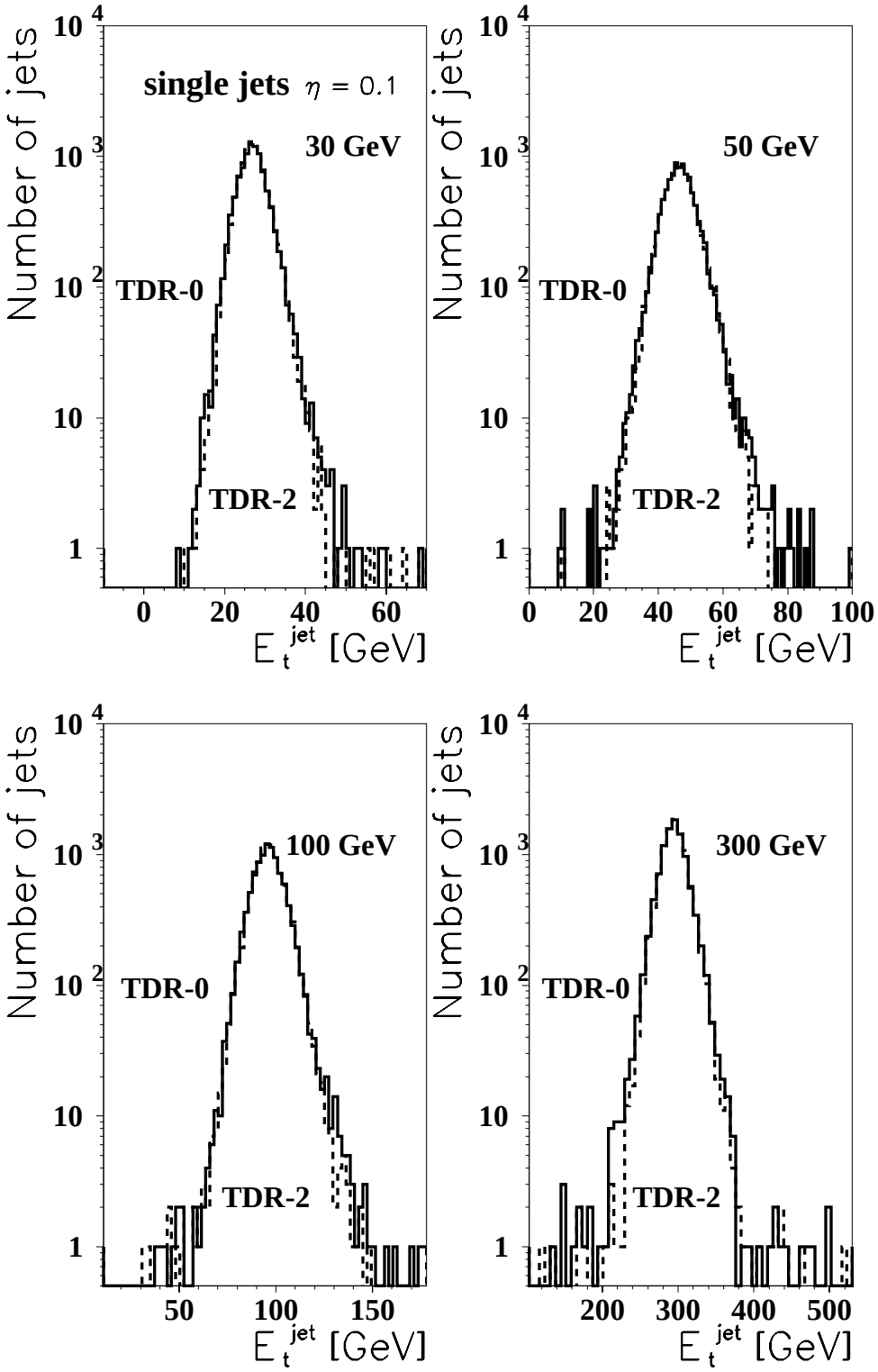

Fig. 1. 46: Jet energy measurements at η = 0.1 for different E_T.

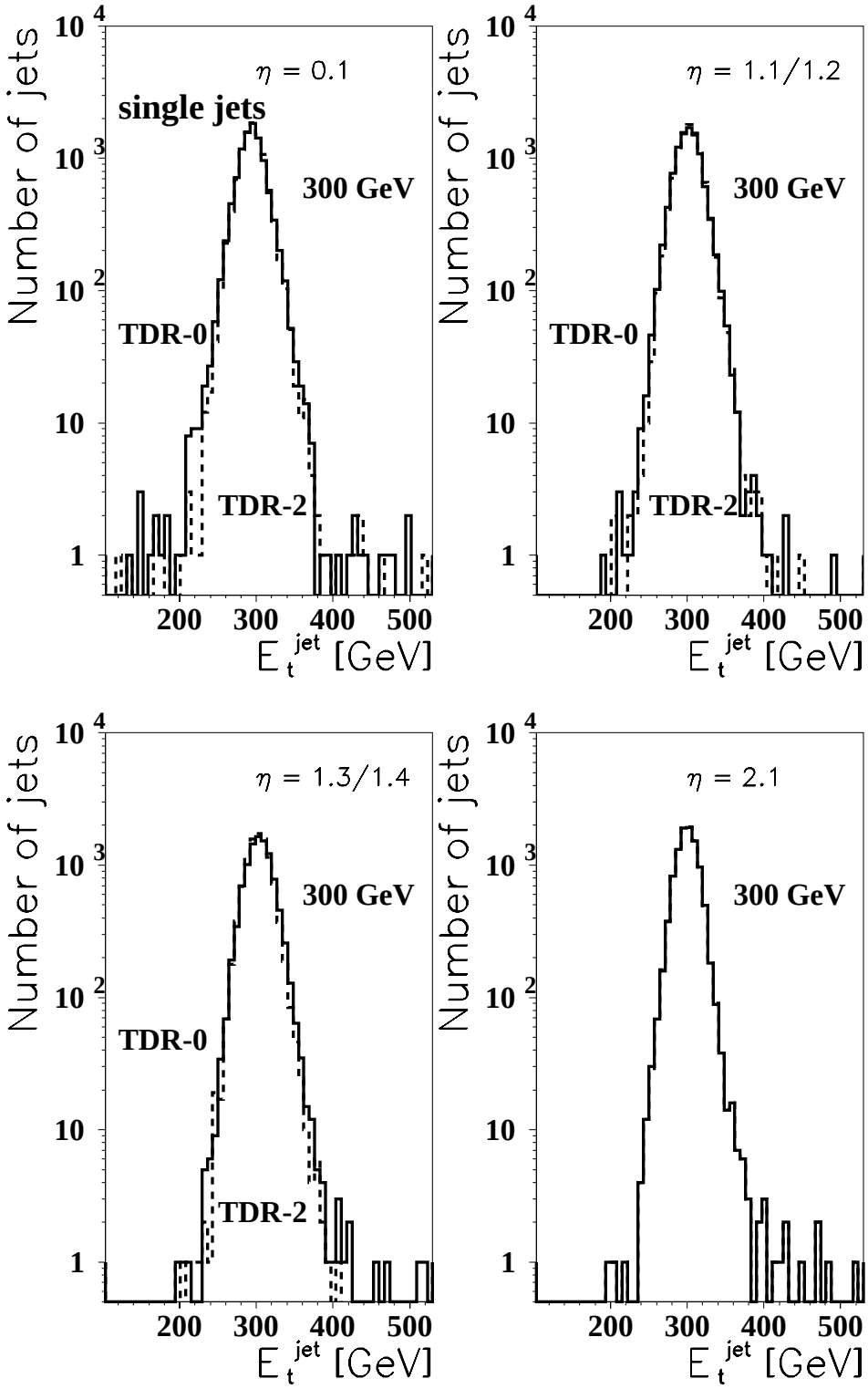

Fig. 1. 47: Jet energy measurements at E_T = 300 GeV for different η.

HB-HE boundary

The geometry of the HB-HE boundary has been extensively studied with GEANT prior to the TDR designs.[22] The study showed that any projective cracks and dead material significantly damage the energy measurements and thus the missing E_T performance of the

detector. In some designs the performance was very sensitive to the width of the cracks. The study concluded that in addition to HCAL, the ECAL should be hermetic with overlapping lips if possible. The present TDR design, with a crack at 53° to the beam line, is the best solution among those considered, because the resolutions showed the least variation with rapidity and the slowest build-up of the low energy tail with increasing crack size.

Fig. 1. 48 shows distributions of reconstructed energies for 300 GeV pions with a baseline 12cm crack and for wider 15cm and 18cm cracks. Compared to TDR-0, TDR-2 shows narrower distributions on the low energy side of the peak for all three crack sizes and a significantly slower build-up of the low energy tail below 200GeV, which is about 3σ below the mean at 300 GeV incident energy.

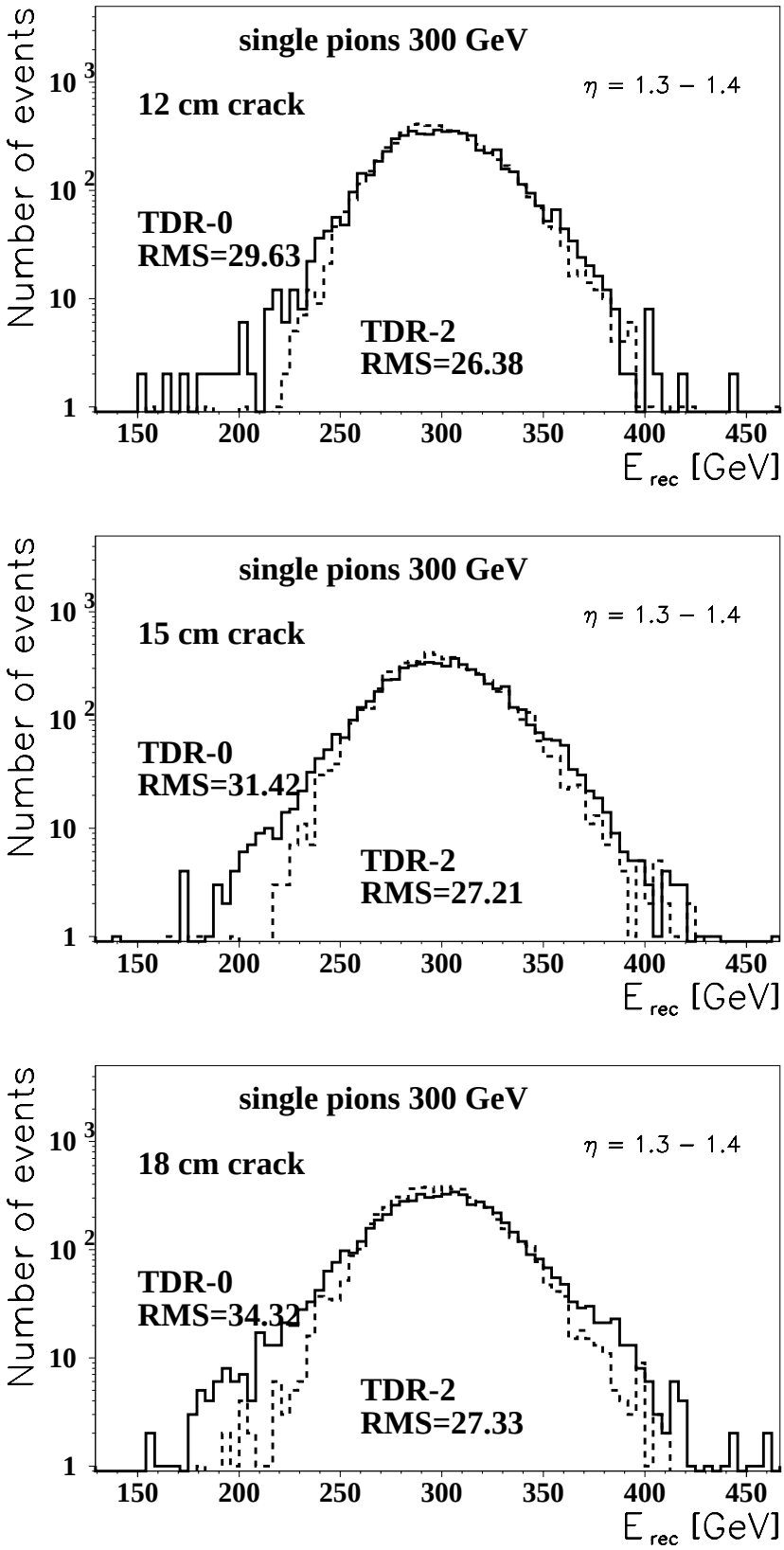

Fig. 1. 48: Reconstructed energy for 300 GeV pions incident on the HB/HE boundary for different crack sizes in TDR-0 and TDR-2.

ECAL-HCAL boundary

Shower particles from interactions in the crystals may spread in the space between ECAL and HCAL in the 4 Tesla field. In TDR-0 the distance between the back face of the crystals and the front face of HCAL is 27cm (56cm, 29cm) at η=0.0 (1.2, 2.2) along the particle direction. We have investigated the effect of this gap in various observables. Although this gap increases with rapidity in the HB region, our single particle and jet simulations show no significant degradation neither in the Gaussian resolutions nor in the low energy tails with increasing rapidity in the HB region.

To illustrate the effects of the magnetic field, Fig. 1. 49 shows distributions of reconstructed energies for 100 GeV pions with and without the 4 Tesla field. A small degradation (<1.5%) is observed in HB, while there is no significant degradation in HE. This effect of the magnetic field includes shower spreading in the HCAL-ECAL interface region as well as the path length effect in the HB absorber gaps discussed previously.

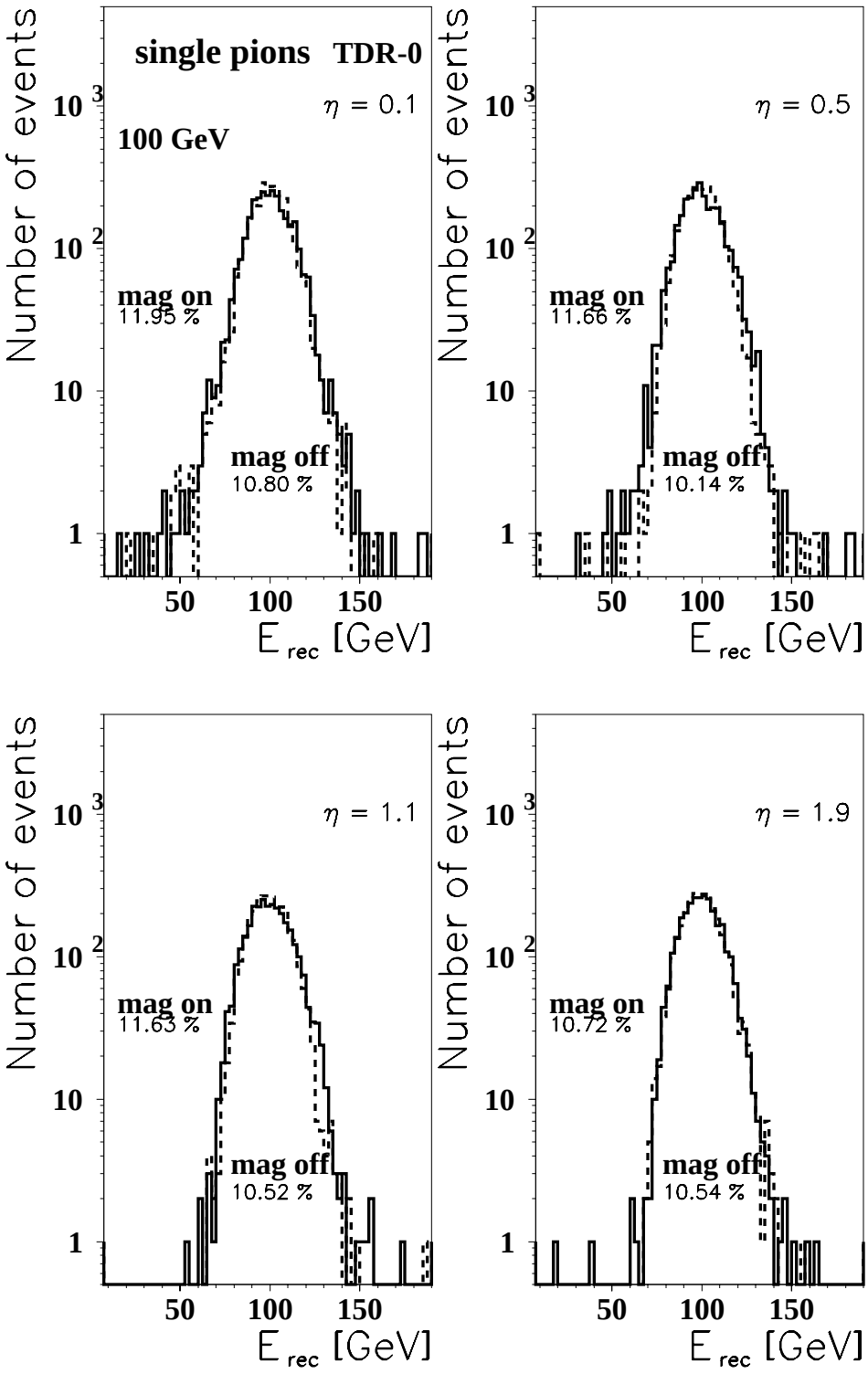

Fig. 1. 49: Reconstructed energy distributions for 100 GeV pions with and without 4T field.

HO simulation

The HB inside the solenoid is too thin to fully absorb the showers of most energetic particles expected. For $|\eta|<3$ HO provides at least 10λ as shown in Fig. 1. 50 to contain energetic showers and reduces the low energy tails in energy measurement. Fig. 1. 51 shows the reconstructed energy distributions for pions (E_T=200GeV) in the muon ring (η=0.33-0.86)

next to the central ring without HO and with HO1 and HO1+HO2, where HO1 is a HO layer before the first iron yoke and HO2 is a layer behind the iron yoke. A clear suppression of the low energy tail is seen with the addition of the two HO layers.

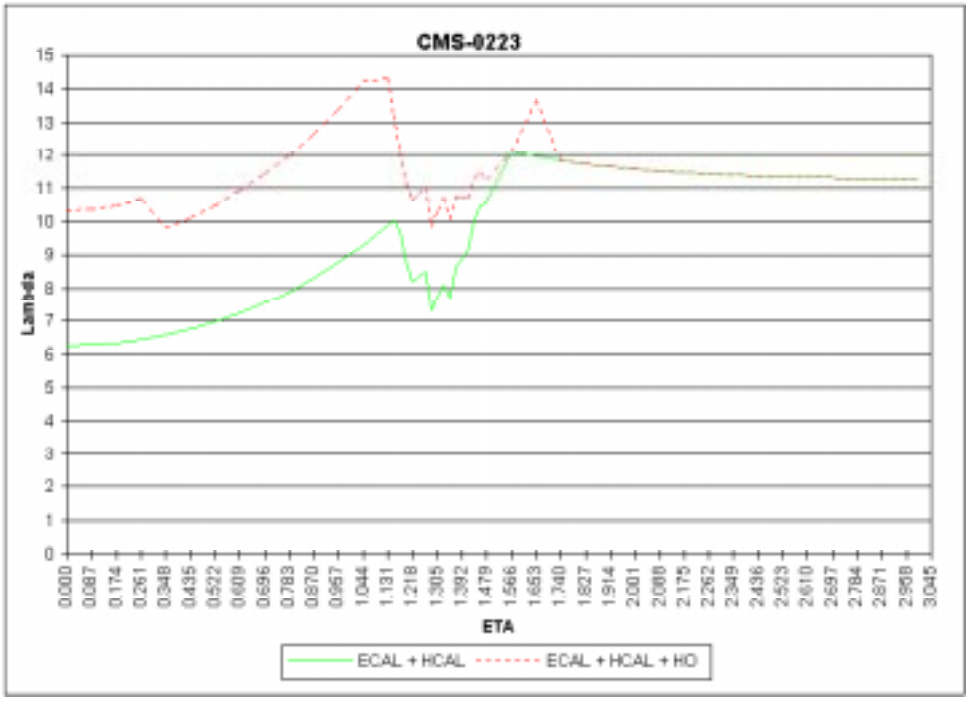

Fig. 1. 50: Interaction lengths for TDR-0.

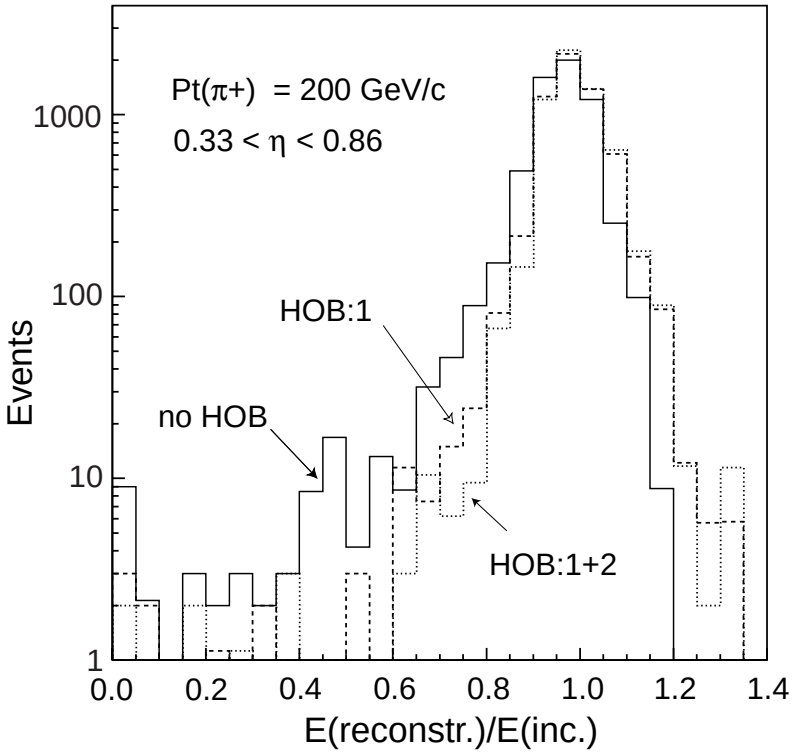

Fig. 1. 51: Single π response with and without HO samples.

1.5.5 HF simulation

The quartz optical fibers are embedded in a matrix of copper absorber and run along almost parallel to the incident particle direction. Due to the optical properties of fibers the maximum amount of Cherenkov light is detected when the charged particle hits the fiber at an angle $\theta = \cos^{-1}(1/n\beta)$, where n is the index of refraction and β is the particle speed. For particles with $\beta \sim 1$ this angle equals $\theta \sim 45^{o}$ or $\theta \sim 135^{o}$. Light produced by particles entering fiber at other angles has very low probability to be detected[23]. Therefore such calorimeter mainly detects electrons and positrons copiously produced in shower development because these particles in contrast to hadrons and nuclear fragments are distributed isotropically even at the beginning of the shower independently of the initial particle direction. Thus a calorimeter based on Cherenkov effect in optical fibers detects hadronic showers predominantly through their electromagnetic component.

The basic design choice is the length of the fibers constituting the longitudinal HF compartments. As with other calorimeters, the HF EM compartment has a depth of 10-20 X_o. Having chosen the longitudinal partition, the weighting strategy for jets must be specified. The response to electrons and hadrons can be adjusted to make $e/\pi = 1$ at a given energy. Minimization of a jet energy resolution as a function of the EM and HAD calibrations allows us to fix these coefficients at an optimal point. There is an unavoidable residual energy dependence to e/π after this procedure is performed.

Response to Jets

Tagging jets accompanying WW fusion have been generated using PYTHIA[24] in the pseudorapidity range $3 < |\eta| < 5$. Jets have been found using LUCELL jet finding algorithm within a cone $\sqrt{\Delta\eta^2 + \Delta\phi^2} < 0.5$ around the jet initiator. Jets were steered into the calorimeter. In this study we concentrated only on the effects of the shower to shower longitudinal fluctuations and their effect on the calorimeter characteristics. Therefore effects of the magnetic field or incomplete shower containment were neglected in order to simplify the procedure.

The calorimeter response to a jet was calculated using signals from SHORT and LONG fibers in two different ways:

- $E_J = N_{SH} + N_L$, that is LONG and SHORT fibers are readout by the same PMT;
- $E_J = \alpha N_{SH} + \beta N_L$. where weights α and β minimize the RMS of E_J under condition that $\langle E_J \rangle = E_J^{gen}$, this could be achieved using separate readout of SHORT and LONG fibers

Energy resolution for 1 TeV jets in the minimum point is 6.7 % whereas in the case when both fibers have the same length and run from end to end of the calorimeter it is about 9.3%, which occurs for any depth > X_o. Thus the optimal arrangement of sensitive media, though with lesser mean packing fraction allows us to achieve more than 30 % improvement in the jet energy resolution as shown in Fig. 1.52.

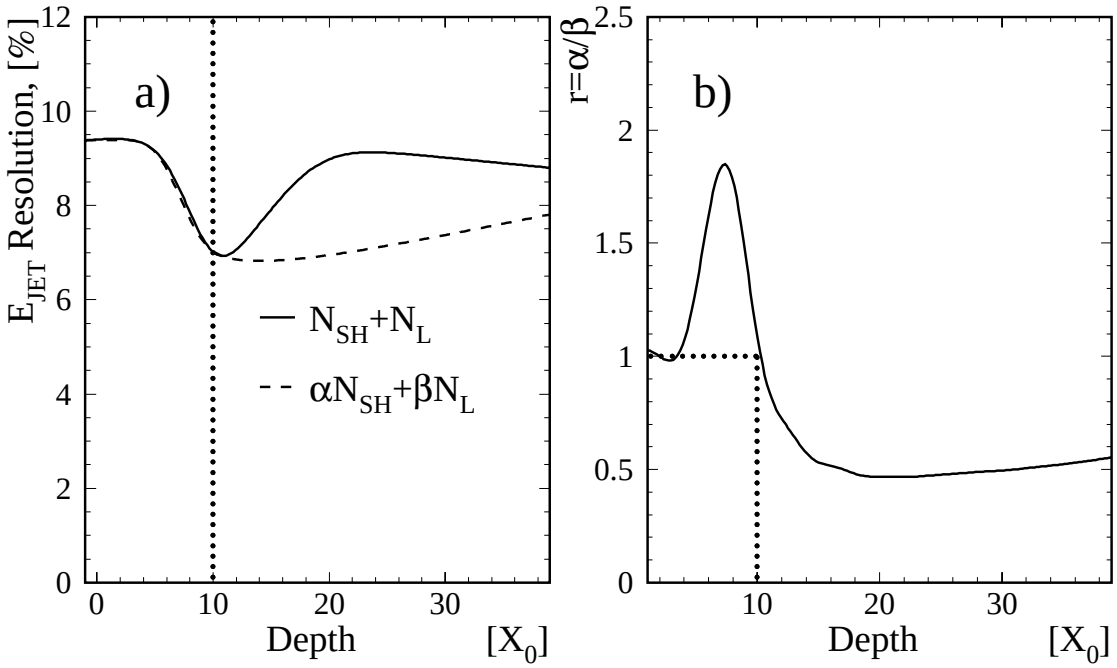

Fig. 1. 52: Jet resolution calculated if signals from long and short fibers are summed up (solid line) and if the signals from long and short fibers are weighted as described in the text (dashed line) as a function of depth; and b) $r = \alpha/\beta$ is the ratio of weights assigned to short and long fibers as a function of depth. r=1 at minimum.

The weighted resolution cannot be made less than minimum reached by the simple sum, but it can be kept at this level in the wider range of lengths L. Fig. 1. 52b shows the ratio of weights assigned to the SHORT and LONG fibers. At the point where jet resolution for the sum of LONG and SHORT fibers reached minimum this ratio should be equal to 1.

The jet response to a weighted sum for different jet energies as a function of the EM/HAD partition is shown in Fig. 1. 53. As with Fig. 1. 52, any depth > 10 X_o seems appropriate.

Fig. 1. 53 and Fig. 1. 54 show the result of the fits to the jet energy resolution for summed and weighted cases. The e/π ratio of the calorimeter is crucial to jet energy resolution. It is possible to compensate calorimeter based on Cherenkov effect in optical fibers by arranging fibers in such a way that packing fraction in the part of the calorimeter where the maximum of electromagnetic shower is deposited is less than in the rest of the calorimeter volume. It appears that we can achieve a 3% constant term for EM compartment depth >10 X_o.

Since the point of minimum jet energy resolution is at the same time the point where the calorimeter becomes almost compensating the short fiber length can be determined in the beam tests. Having found the optimal configuration it is possible to use single readout from long and short fibers, halving the number of electronic channels. This looks very attractive since it would decrease substantially the overall calorimeter cost. Since the position of the jet energy resolution minimum as a function of depth L is sensitive to jet energy and also is affected by fiber radiation damage, which occures at the maximum of EM shower, we suggest a separate readout scheme for long and short fibers. Choosing L=15-20 X_0 it is possible to avoid these problems using weighted sum of long and short fibers. Radiation damage in long fibers will lead only to re-adjustment of weights.

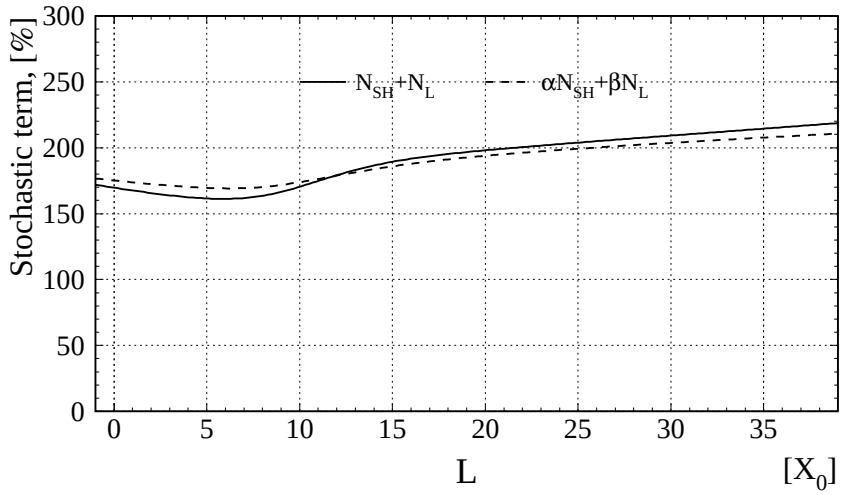

Fig. 1. 53: Jet resolution function - stochastic term versus short fiber depth.

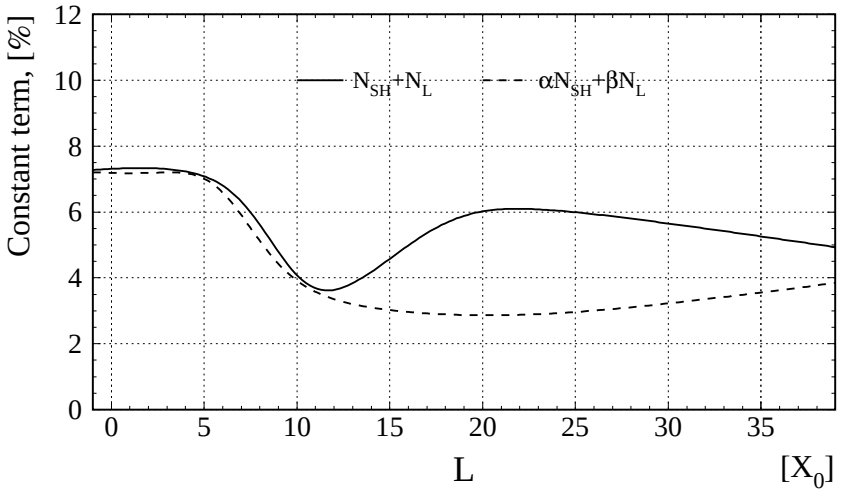

Fig. 1. 54: Figure 10. Jet resolution function - constant term versus short fiber depth.

The HE/HF interface: η dependence of the energy resolutions

The HE/HF interface is located at |η| = 3 where the coverage of HF starts. HE and HF are separated by about 7 m and use different techniques for energy reconstruction; HE utilizes scintillation light whereas the HF relies on the Cherenkov effect in the active medium of the calorimeter. We have studied the energy resolution performance at this transition region by simulating single particles and jets at and around this η region ($2 < |\eta| < 5$) using GEANT.

The expected energy resolution for various pion energies (10 - 800 GeV) is shown, in Fig. 1. 55, as a function of pseudorapidity. As can be seen, there is no significant effect in the HE/HF transition region (|η| =3). Aside from the expected difference in energy resolutions on either side of the crack (the intrinsic resolution of HE is better than that of HF), no surprising effect, such as a dramatic and rapid degredation in resolution due to change from HE to the HF, is observed. The worsening of energy resolution at |η| around 5 is due to incomplete shower containment.

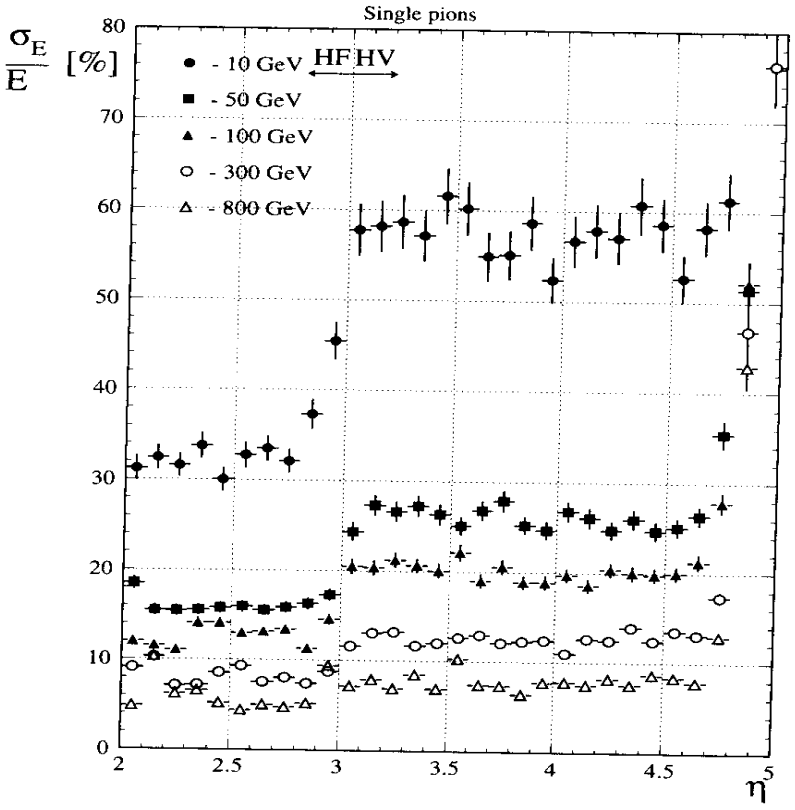

Fig. 1. 55. Energy resolutions for single pions in the energy range of 10 to 800 GeV as a function of η are given above. The HE/HF interface is located at |η| =3.

We have generated 1 TeV forward tagging jets using PYTHIA[24]. Jets are produced in qq→H qq reaction through VV→H→VV fusion process. The particles in jets generate cascades in the HE and the HF. Jets were reconstructed and comparison was carried out between the generated and the simulated signals. We display in Fig. 1.56 the E_{rec}/E_{gen}, E_{res}, $E_{t,rec}/E_{t,gen}$ and $E_{t,res}$ as a function of η. The results indicate that the overall response will drop by about 20% in amplitude in η = 3. The performance at HF, however, is stable up to η = 4.5. Beyond that, the performance worsens due to small angle leakage. The energy resolution remains at the level of 5% in the HE region, increases smoothly to about 10% at η = 3 and decreases to 8-9% in the HF domain up to η = 4.5. As with the HB/HE interface, a monotonic variation in the mean response and the resolution (at high E_T) is maintained in the HE/HF boundary.

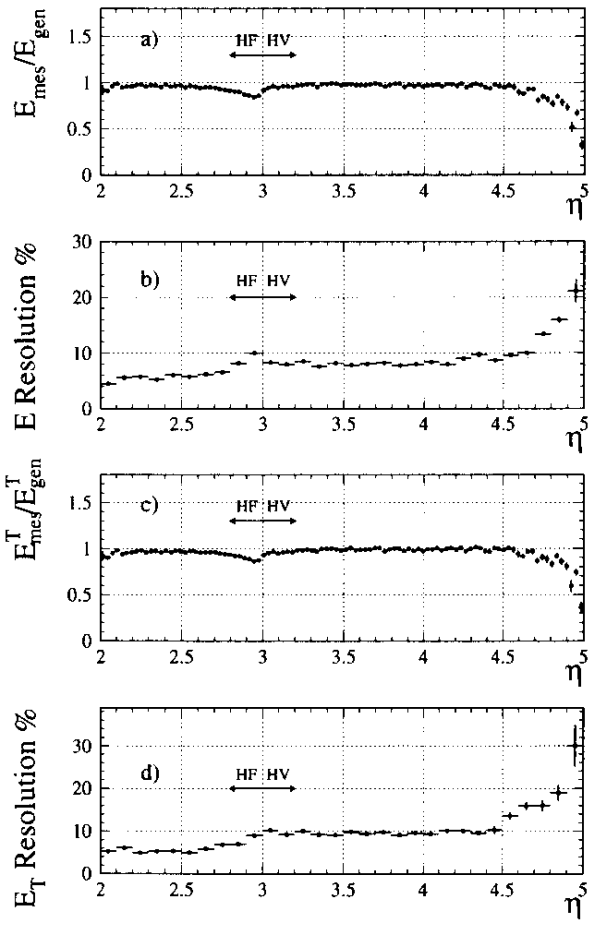

Fig. 1. 56: a) Normalized energy response; b) energy resolution, c) normalized transverse energy response; and d) transverse energy resolution for 1 TeV tagging jets as a function of η.

The effect of radiation damage on the HF performance

Pure silica, the material of the fiber core, is known to resist high radiation doses with minimal deterioration in its optical properties. The radiation hardness of quartz optical fibers also crucially depends on the cladding around the quartz core since the cladding material makes total internal reflection possible.

We convoluted the expected radiation levels in the HF (see chapter 5) as a function of η with the attenuation known and studied the influence of the fiber transparency loss on the energy resolution for jets after 10 years of LHC operation. We use the same 1 TeV jet sample as in the previous section in our calculations here[25]. The results are given in Fig. 1. 57 and they show the jet energy resolution as a function of η, for quartz/quartz fibers (top) and quartz/plastic fibers (bottom) for two cases: with (black circles) and without (open circles) a 10 years equivalent dose. The jet energy resolution practically does not change in the case of the quartz-quartz fibers while a significant deterioration starts to set in for quartz-plastic fibers at about $\eta = 4$. This is the primary reason that our design calls for quartz-quartz fibers in the region $|\eta| > 4$.

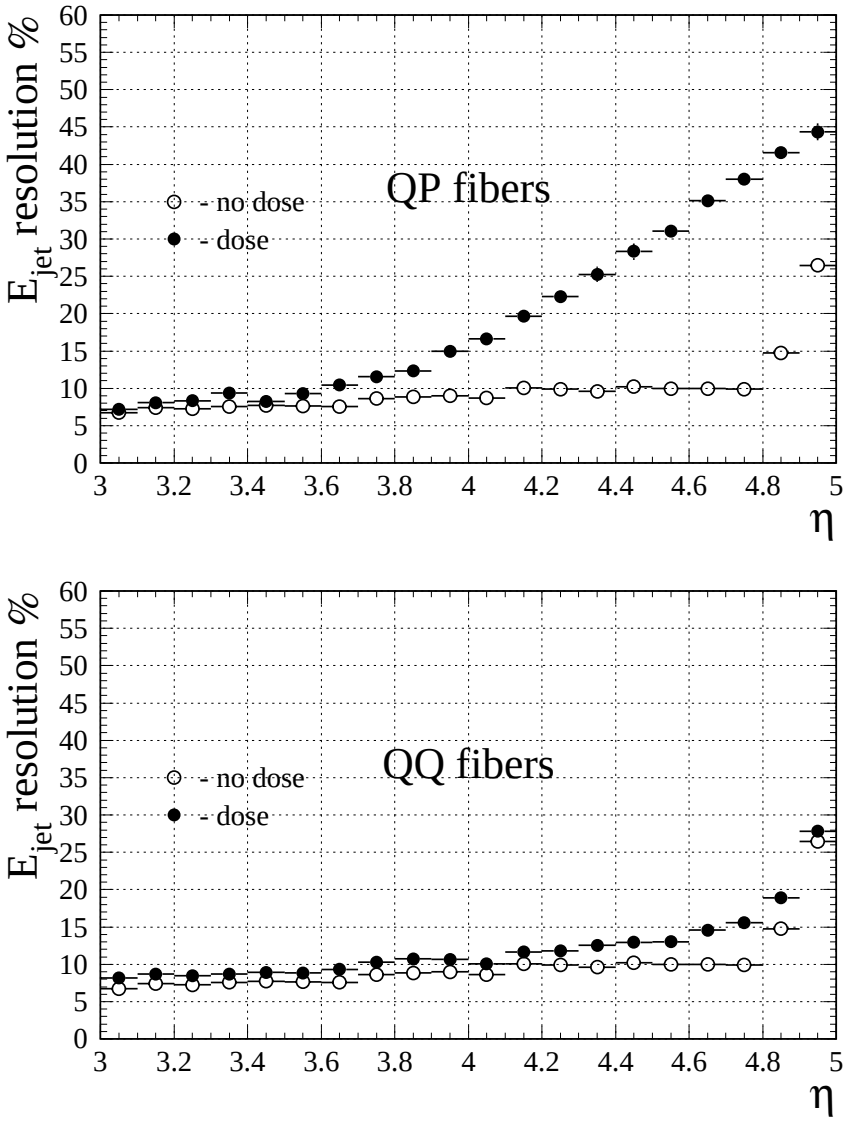

Fig. 1. 57: Energy resolutions for 1 TeV jets as a function of η, the quartz/plastic fibers (top) and the quartz/quartz fibers (bottom), are shown. Full circles in both figures correspond to radiation dose in fibers after 10 years of LHC operation.

Jet tagging and reconstruction: transverse granularity

The overall aim of this study is to find the optimal transverse granularity needed for forward tagging jet identification and reconstruction with simultaneous maximization of the pileup suppression. The working hypothesis is that the jets we are interested in are in the range 500 GeV ≤ E_{jet} ≤ 3 TeV, with E_T^{jet} 30 GeV[26].

Monte-Carlo generation of the pileup background

We have simulated background events using ISAJET.[27] We have considered a centre of mass energy per pp collision of 14 TeV, a σ_{pp}^{tot} = 100 mb, a luminosity of 10^{34} cm^{-2} s^{-1} and an interbunch crossing time of 25 ns. This corresponds to an average number of pp collisions per crossing equal to 25, Poisson distributed.

In addition we made the conservative hypothesis that the pp background collisions consist

of a mixture of 60 mb minijets ($qq \rightarrow qq$, $p_T^{jet} > 5$ GeV) and 40 mb minimum bias events.

The generated multiplicity distribution per LHC crossing has a mean value of ≈ 5700 with rms ≈ 1200. Here, γs are considered as stable particles. The multiplicity distribution of particles reaching the HF sensitive areas has a mean value of ≈ 1050 (per HF arm), with rms ≈ 320. More details about the expected pileup background can be found in the references.[28,29]

Monte-Carlo generation of the tagging jets

High mass Higgs events of the type $qq \rightarrow WW(ZZ) \rightarrow Hqq$, with $m_{Higgs} = 800$ GeV/c^2 were generated using PYTHIA[24].

On the average, the mean value of the energy of the particles inside a jet is much higher (<E> ≈ 60 GeV, rms ≈ 115 GeV) than for background particles[28] in HF (<E> ≈ 8.1 GeV, rms ≈ 13 GeV). This is one of the crucial jet features for the jet finding over the pileup background. The second important point concerns the collimation of the energy in a jet: on the average, ≈ 50% of the jet energy is concentrated in a radius of 5 cm. Due to the spread (although small) of the particles in a jet, the strong magnetic field and the central hole in the HF, not all the particles in a jet can reach the HF sensitive areas. The mean value of the multiplicity distribution of the tagging jets at the IP is ≈ 27 and ≈ 20 at HF. This loss of particles induces already an error in the reconstruction of the jets: the distribution of the misdetermination of the jet energy (at the level of particle energies) in terms of $\{[E^{jet}(IP) - E^{jet}(HF)]/E^{jet}(IP)\}$ has a mean value of ≈ 2% with an rms of ≈ 4%. In ≈ 2.5% of the cases, the energy lost accounts for more than 10% of the jet energy at the IP.

Monte-Carlo generation of the showers

The analysis that follows is done using one of the arms of the HF.

We have generated showers, using GEANT 3.21[21]. FLUKA[30] was used for the hadronic interactions. An E_{cut} of 10 keV was imposed on all particles in the showers. For cascade simulation, the HF is seen as a copper block of dimensions 3000x3000x1650 mm^3 (with a central hole of dimensions 300×300×35 mm^3), with quartz fibers embedded on it. The packing fraction is 1.5% by volume.

Every particle in a crossing which reaches the HF sensitive area gives rise to a shower. For cascade generation the impact point of the particle in the calorimeter and its three momentum are used as initial parameters, together with the particle identifier.

Under these conditions, we have made a full simulation of 200 background crossings and 1261 "tagging" jets in the HF.

The average transverse profile of a tagging jet is very narrow in space. On average, a significant fraction (≈ 30%) of the total jet light concentrates in a single 5×5 cm^2 tower. Note that the extent of the jet in rapidity is the same as in HB or NE.

The fraction of the energy containment in a jet, as a function of the tower transverse size (assumed square), is given in Fig. 1. 58 for three η regions. The jet extent in η space is essentially independent of η, so that a common segmentation is used in all CMS calorimetry, unless the hadronic shower size exceeds this segmentation as in HE at $|\eta| \sim 3$.

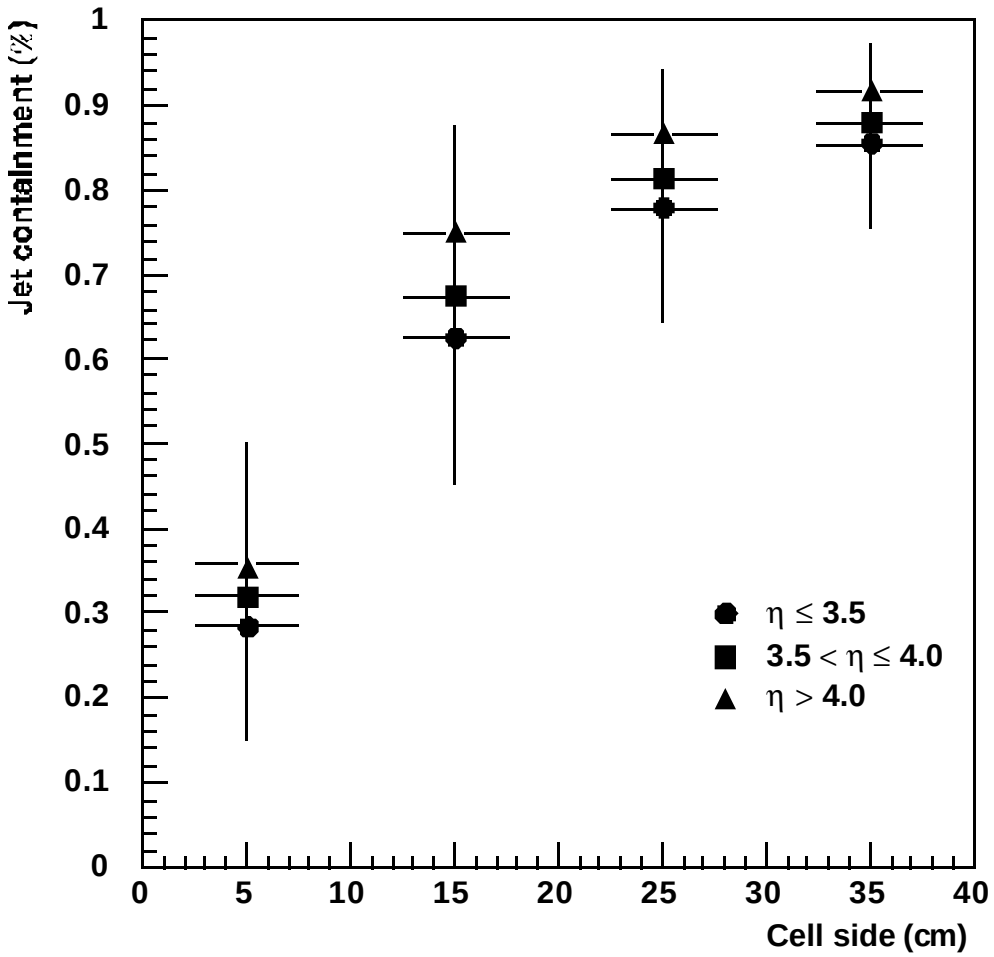

Fig. 1. 58: Jet shower containment (in %) as a function of the tower side dimension (see text), for three η regions.

A typical transverse profile of a jet event over a background crossing is shown in Fig. 1.59. The "min bias" energy flow and the tagging jet are distinct.

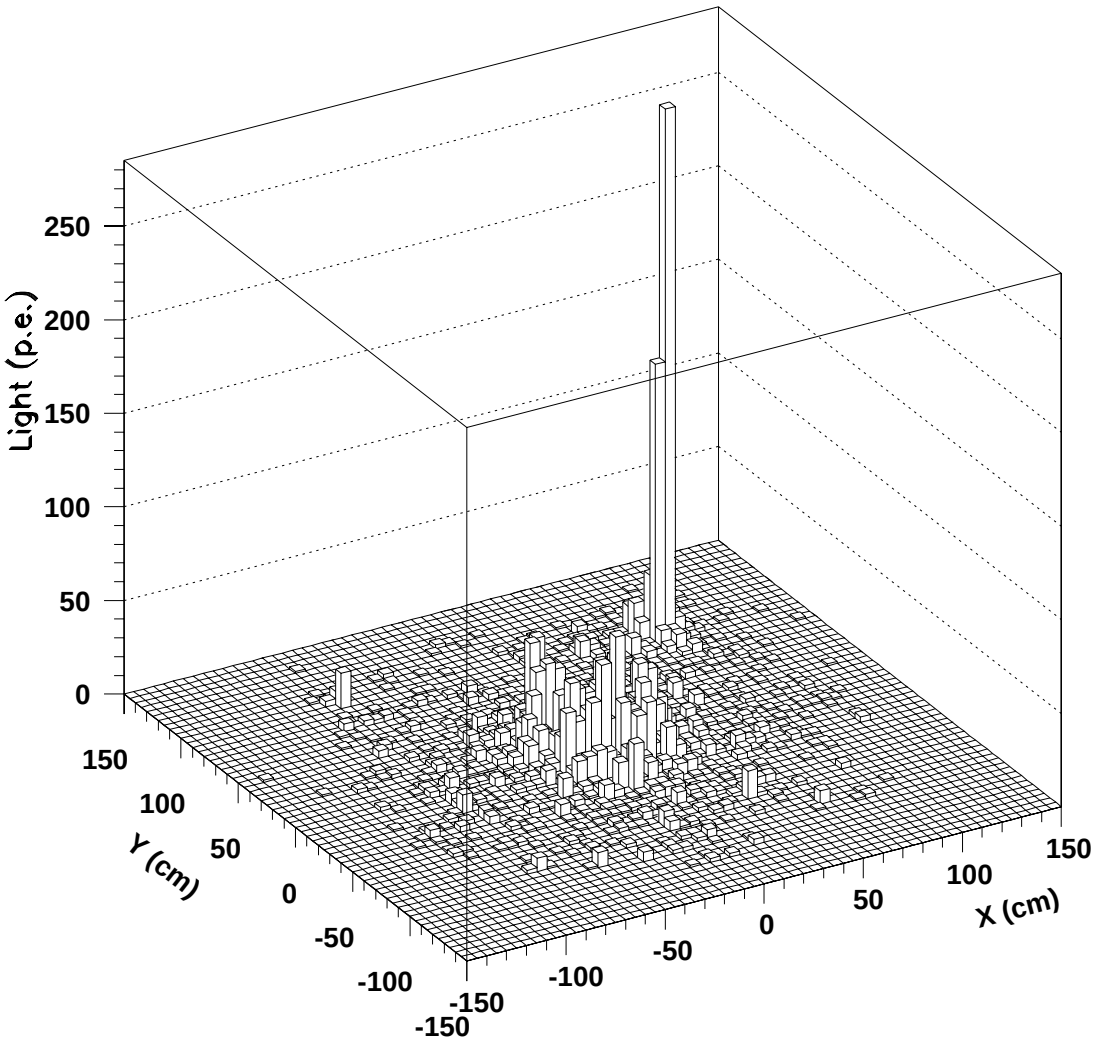

Fig. 1. 59: Transverse profile of a crossing containing a tagging jet.

Jet tagging and reconstruction

We have designed a simple tagging algorithm that allows to detect a jet and make a first calculation of E^{jet} and E_T^{jet}. The algorithm allows a high level of suppression of the pileup background.

The jet tagging is related to the issues of transverse granularity and energy and angular resolutions in the reconstruction of single jets, as well as in dijet systems.

The algorithm includes the following steps:

- Find a maximum among the light collected (S) in the considered towers of the HF. The number of physical towers depends on the transverse granularity used.
- Check whether $S > S_{cut}$ and $S_T > S_{T,cut}$.
  If these two conditions are fulfilled, we assume that a seed central tower (CT) of a tagging jet candidate is found.
- Go back to 1) and repeat the operation for other possible maxima.

Stop the cycle when no additional candidate is found or a maximum number of candidates has been obtained.

If the list contains at least one candidate:
- Choose as CT seed of the tagged jet the tower having the maximum S_T.
- Reconstruct the jet by summing up the content of the 3×3 towers around the maximum.

We assume that the jets we are looking for have E > 500 GeV and E_T > 30 GeV, which are typical lower values for tagging jets in the heavy mass Higgs production and for veto when looking for sleptons. The calibration constant is ≈ 0.4 p.e./GeV (in the assumed experimental conditions) and the maximum allowed number of jet candidates in a given crossing is set to 5.

Transverse granularities

We have applied the above algorithm using various transverse granularities, with the aim of determining the optimal one. This criterion guided our baseline choice of granularity.

Pileup background rejection power

A strong rejection power is mandatory. We have first applied the method described above to crossings containing only background (the 200 crossing sample fully simulated in the HF), looking for the E_{cut} and $E_{T,cut}$ that have to be applied to obtain 100% rejection in the investigated sample of pileup background events. The rejection power is only sensitive to the applied $E_{T,cut}$. On the other hand, the use of large surface granularities (as 15×15 cm^2) leads to no rejection power (at least for $E_{T,cut}$ < 30 GeV).

Jet tagging

We now mix each fully simulated jet in HF with each of the background crossings to form a sample of 252200 CMS crossings containing one jet per crossing at HF.

Different transverse granularities for HF lead to different efficiencies in jet tagging. The optimal granularity, that maximizes the jet finding efficiency (≈ 55.4%) with simultaneous suppression of the background, is that of towers of 5x5 cm^2 for $|\eta| \geq 4$, 10x10 cm^2 for $|\eta| < 4$. In what follows we will use this transverse granularity for jet finding and reconstruction over the pileup background.

Jet reconstruction

The tagged jets are reconstructed by summing up the light content of the 3×3 towers around the maximum, after applying the jet finding algorithm with the $E_{T,cut}$ that allows background suppression. The energy of the jet is defined as

$$E^{jet}(GeV) = 1/0.46 \times \sum_i S_i(p.e.),$$

where i runs from 1 to 9 and S_i(p.e.) is the light collected in tower i.

The jet "impact point" in HF is defined as the centre of gravity of the 9 towers. The X^{jet} and Y^{jet} coordinates allow to reconstruct E_T^{jet} and the transverse angle Θ^{jet}. The reconstructed jet energy and E_T, compared to the generated values, show a mean consistent with zero and an 18% (E^{jet}) and 17% (E_T^{jet}) fractional rms. The fractional azimuthal distribution is centered at zero with an rms = 2 degrees.

Two jet reconstruction in Higgs production

We have used PYTHIA to generate events of the type $qq' \rightarrow WW(ZZ) \rightarrow Hjj'$ with m_{Higgs} ≈ 800 ± 200 GeV/c^2. The inclusive η distribution of the jets is given in Fig. 1. 60. Note that

about half of the tagging jets are in HF and half in HE. Therefore, the HE/HF boundary must be very well understood.

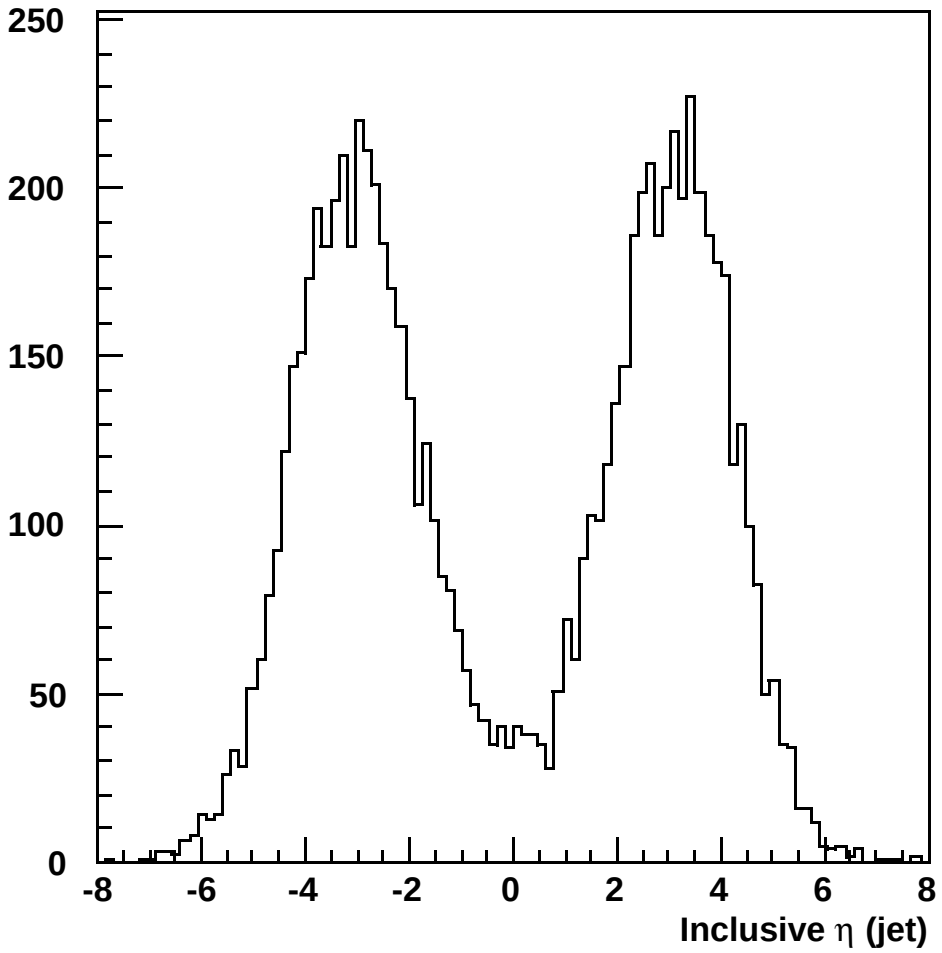

Fig. 1. 60: The inclusive η distribution of the tagging jets in the Hqq' sample.

We have considered the events having a forward and a backward jet in the region $3 < |\eta| < 5$ and smeared the jet energy and the jet transverse angle according to the resolutions found earlier. The resolution of the combined jets is correlated with $E_T^{jj'}$ (generated). The $E_T^{jj'}$ error has a 72% stochastic term and an 8% constant term.

Under these conditions, the error in the reconstruction of the $p_T^{jj'}$ of the dijet system, balancing the typical p_T^{Higgs} = 130 GeV/c, in an Hqq event, will be better than 15% (≈ 20 GeV/c).

1.6 LUMINOSITY MEASUREMENT AT CMS

1.6.1 The measurements required

A precise knowledge of the proton-proton luminosity at the CMS interaction region is an essential ingredient in the measurement of absolute cross sections in the experiment. Monitoring the instantaneous luminosity is also important for making corrections to the data for detector effects related to the number of interactions per beam crossing. A luminosity working group was formed in 1994 with representatives from several associated areas within CMS. The

responsibilities of the working group include the following topics:

- absolute luminosity measurements
- relative luminosity monitoring over time
- monitoring of beam-gas backgrounds and backgrounds during beam tuning and scraping
- providing real-time luminosity information to CMS and the LHC machine
- development of detectors for luminosity and background monitoring as needed.
- physics topics associated with detectors used for luminosity monitoring.

Several guidelines have been established for the luminosity measurements:

- The group will aim to measure the luminosity at CMS with a precision of better than 5%. This precision is chosen to match approximately the precision which theorists expect to achieve in predictions for hard scattering cross-sections at LHC energies by the year 2005.
- There should be sufficient redundancy in the detectors and techniques for luminosity monitoring to allow for consistency checks and the situation when one monitoring technique is not operational.
- Separate luminosity measurements must be made for all 2835 bunch crossings.

Several techniques are under study for determining the absolute luminosity. The first is called "counting zeros". Here, two sets of luminosity monitors, symmetrically located on each side of the IP, count the fraction of times a given bunch crossing results in no detected particles on either side. The luminosity is inferred from the rate of such zeros. This technique is used by the D0 and CDF experiments at the Fermilab Tevatron collider and leads to an uncertainty of order 5%. This method is only appropriate if the rate due to σ_I leads to a significant fraction of zeros. Thus it is used only up to ~0.01 of the design luminosity. The second is the Van der Meer method in which the proton-proton interaction rate is measured while the beams are displaced transversely through each other. This method was used successfully at the ISR with continuous beams and at the Fermilab Tevatron collider with bunched beams. A third possibility is to use the trigger tower sums as a "current" of rate. This technique could then be used at design luminosity and we could transfer the measurement to it at low luminosity from the "zeros".

This chapter also describes the monitoring of relative luminosity over time and accelerator backgrounds using overlapping techniques. Both HF and the Level 1 Calorimeter Trigger are used in relative luminosity monitoring.

Calibrating the luminosity system will require both low-luminosity running, where there will be an average of one interaction per bunch crossing, and running the LHC at a center-of-mass energy of 1.8 or 2.0 TeV, so that the calibration can be cross checked with certain measured cross sections at the Fermilab Tevatron. The former will happen as a matter of course, since the LHC start-up luminosity will be a factor of 10 to 100 lower than the design luminosity of 10^{34} cm^{-2} s^{-1}. The latter is also feasible, according to discussions with LHC machine physicists.

1.6.2 Absolute luminosity measurements

Two techniques are presently foreseen to determine the absolute luminosity.

Counting zeros method

The counting zeros technique works as follows. Two sets of luminosity monitors,

symmetrically located on each side of the IP, count the fraction of times a given bunch crossing results in no detected particles on either side. The luminosity is inferred from the rate of such zeros.

The counting zeros technique is used by the D0 and CDF experiments at the Fermilab Tevatron collider and leads to an uncertainty of order 5%. A modified version of this technique is expected to yield similar precision at CMS at low luminosity.

The probability of having an empty crossing, a "zero", where the forward/backward counters detect no particles is given by:

$$P(0) = e^{-n_2/2} \times (2e^{-n_2/2} - e^{-n_1})$$

where n_2 is the average number of forward/backward coincidences and n_1 is the average number of one-side hits. n_1 and n_2 are related to the instantaneous luminosity, L, according to

$$n_1 = L\tau(\varepsilon_1^{sd}\sigma^{sd} + \varepsilon_1^{dd}\sigma^{dd} + \varepsilon_1^{hc}\sigma^{hc})$$

and

$$n_2 = L\tau(\varepsilon_2^{sd}\sigma^{sd} + \varepsilon_2^{dd}\sigma^{dd} + \varepsilon_2^{hc}\sigma^{hc})$$

In these expressions, τ is the LHC machine revolution period, σ^{dd}, σ^{dd}, and σ^{hc} are the cross sections for single-diffractive, double-diffractive, and hard-core scattering, respectively. ε_2^{sd}, ε_2^{dd}, and ε_2^{hc} are the acceptances for forward/backward coincidences from these processes, and ε_1^{sd}, ε_1^{dd}, and ε_1^{hc} are the acceptances for single-side hits.

The counting zeros technique for measuring absolute luminosity relies on knowing the above components of the total cross section at the center-of-mass energy of 14 TeV. Measuring these cross sections is part of the physics program of the proposed FELIX experiment.

Fig. 1. 61 shows the probability of recording a zero per bunch crossing as a function of instantaneous luminosity, assuming a proton-proton total cross section of 100 mb. One sees that for luminosities in the range 10^{32} to 10^{33}, which is the anticipated luminosity range during the first 2 years of LHC operation (similar to the present situation at the Fermilab Tevatron), the probability of obtaining a zero is not negligible.

Fig. 1. 62 shows the time between zeros as a function of luminosity for full, 50%, and 10% acceptance luminosity detectors. At start-up luminosity, the HF array yields a counted zero as frequently as every microsecond, yielding a luminosity measurement with negligible statistical uncertainty in a fraction of a second.

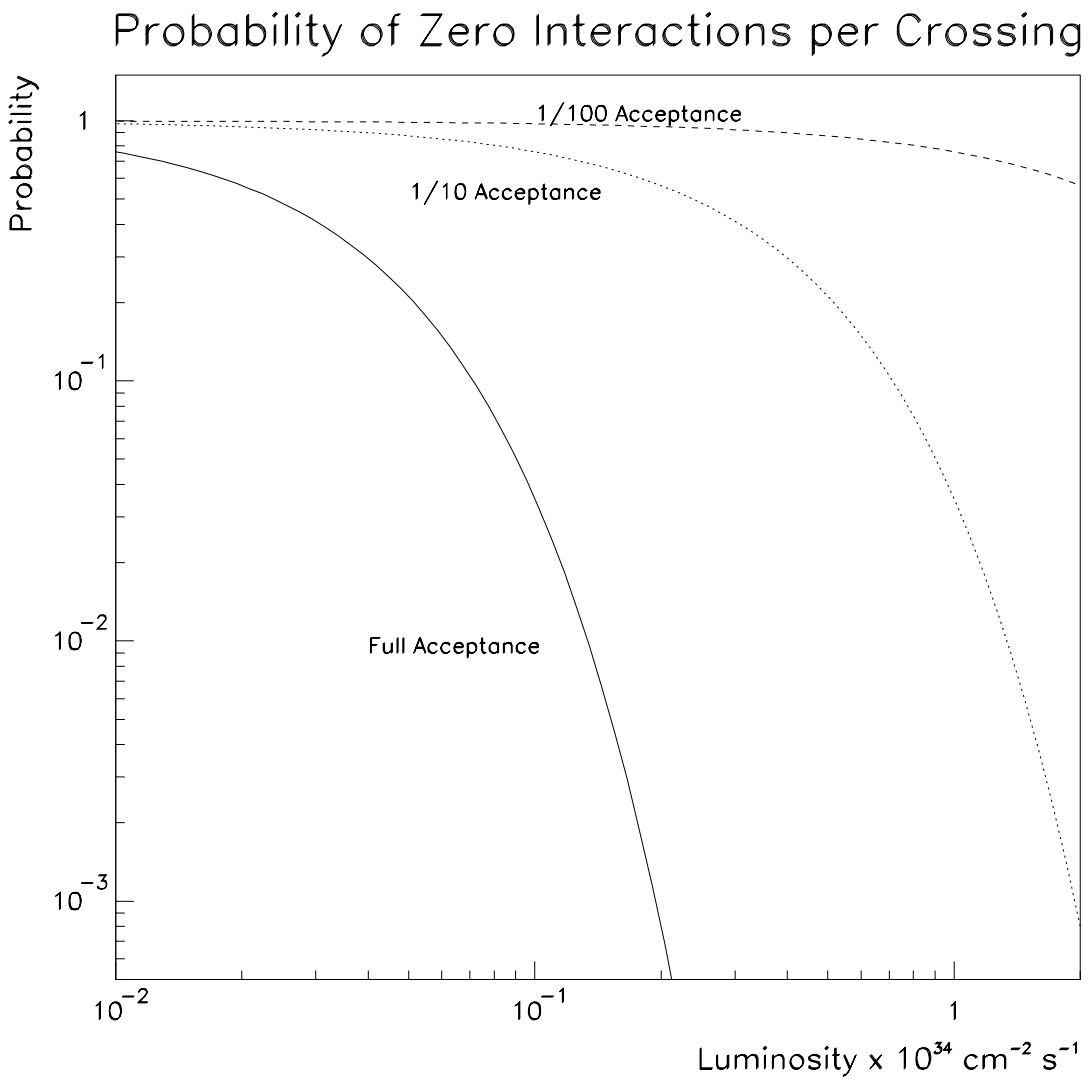

Fig. 1. 61: The probability of recording a zero (no particles detected in the forward and backward luminosity counters) vs. instantaneous luminosity.

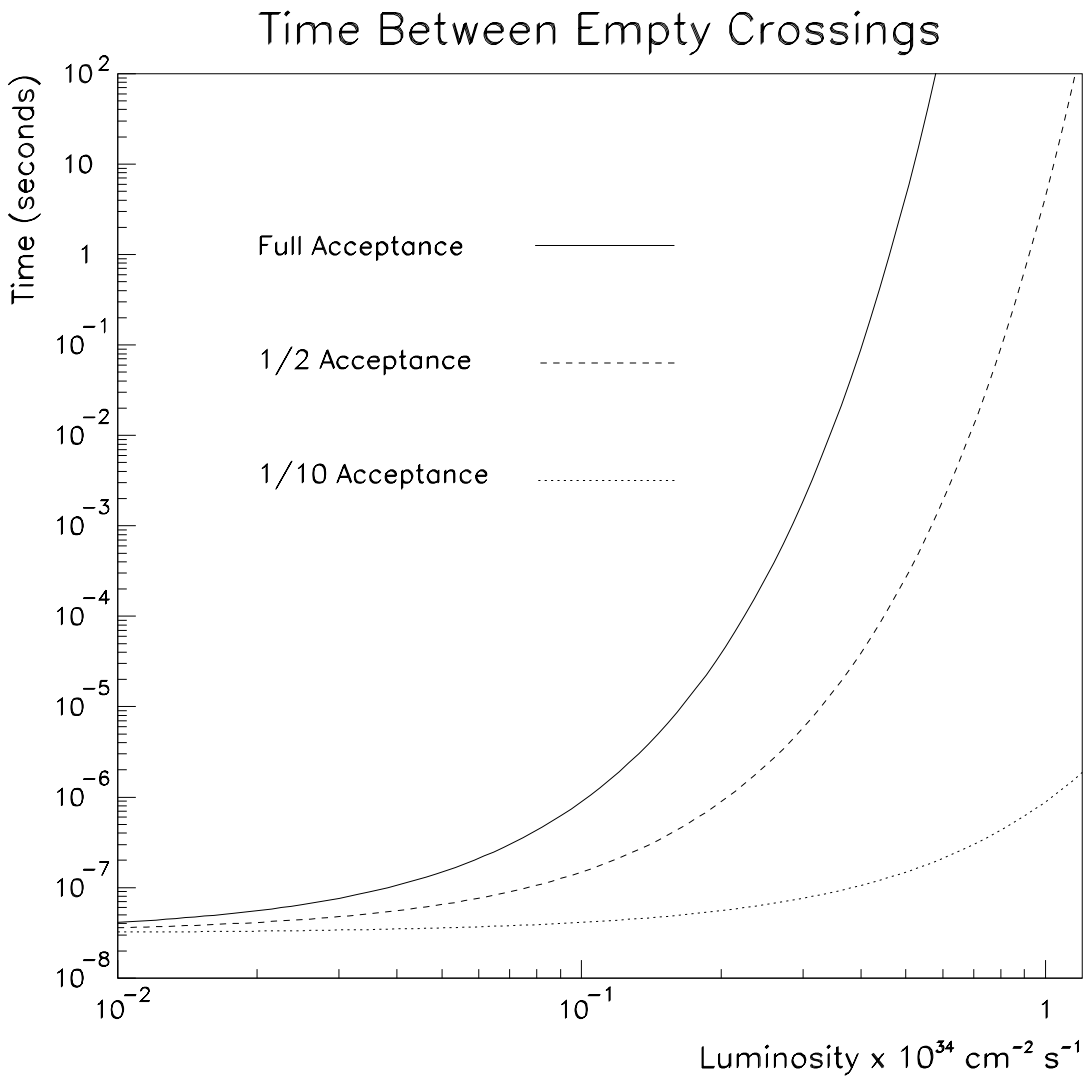

Fig. 1. 62: The average time between recorded zeros vs. instantaneous luminosity.

Van der Meer method

The Van der Meer method is a promising candidate for a measurement of the absolute luminosity. With bunched beams as in the LHC, the Van der Meer method involves calculating the luminosity according to the formula

$$L = N_1 \; N_2 \; f/h_{eff} \; w_{eff}$$

where N_1 and N_2 represent the number of particles in the two protons beams, f is the LHC machine revolution frequency, and h_{eff} and w_{eff} are the effective height and width of the beam overlap region at the interaction point. The two beam currents are determined precisely by the accelerator, and f is known exactly. h_{eff} and w_{eff} are measured by displacing the beams with respect to each other, separately in the horizontal and vertical directions, while monitoring the proton-proton interaction rate with one or several relative luminosity detectors as a function of the beam displacement. Difficulties may arise because the small transverse beam sizes (σ's of order 15 μm) will require the control and monitoring of beam displacements with μm precision. It is expected that Van der Meer scans would be performed on an occasional basis at relatively

low luminosity and would serve to calibrate relative luminosity monitors for continuous measurements. The feasibility of controlled Van der Meer scans is being studied by LHC machine physicists, and discussions between CMS and the LHC machine are being coordinated by LEMIC (the LHC Experiment - Machine Interface Committee).

1.6.3 HF as the luminosity monitor for couting zeros

The HF detectors are on each side of the interaction region, covering the pseudorapidity range of approximately $3 < |\eta| < 5$, and will be used in the counting zeros technique.

The HF elements have the following characteristics: good and well-determined acceptance for detecting hard-core scattering, very tight (i.e. sub-ns) timing resolution in the high-rate environment, high efficiency for single minimum ionizing particles, a large dynamic range and radiation hardness.

Hits in the HF towers will be used to count the number of front-back coincident events, the number of front-only or back-only events, and the number of neither-side-hit events for each of the bunch crossings. These rates, the acceptances of the counters for hard-core scattering, single diffractive and double-pomeron-exchange scattering, and measured (by CMS and other experiments) cross sections for these processes at $\sqrt{s}$ = 14 TeV will combine to yield the luminosity for each bunch crossing. The HF towers will be used for several other purposes. They will monitor interaction rates during separated beam scans (Van der Meer method), which will aid in the absolute luminosity calibration. They will also provide real-time accelerator diagnostics during scraping, beam tuning, and throughout a physics store (run).

During the first few years of LHC running, the anticipated luminosity will be a factor of 10 to 100 lower than the design luminosity of 10^{34} cm^{-2} s^{-1}, although the number of bunches will be the design value of 2835. Rates in the HF towers during low luminosity running will calibrate other luminosity tools for transfer to higher luminosities. Other tools include the rates of easily-identified and reconstructed physics process. Rates for W, Z, and high-p_T J/ψ production are candidate physics processes for luminosity monitoring.

An important step in calibrating the HF towers will be to run the LHC at a lower center-of-mass energy where the total pp cross section and its components (hard-core, elastic, single-diffractive, ...) have been accurately measured. For example, it will be possible to run the LHC as low as 2 TeV, albeit with reduced luminosity, so that the luminosity calibration can be cross checked with the measured cross sections at the Tevatron. (Note that the cross sections in proton-proton and proton-antiproton collisions are approximately equal for the above processes at 2 TeV.)

1.6.4 Relative luminosity monitoring using HF

Luminosity measurement by HF is intended mainly to serve two purposes; one is to provide input to accelerator tuning during the initial phases of LHC operation and the other is to monitor luminosity during data taking. The constraints on this system are the following:

- it is required that the system is ready to function in day one of LHC start up,
- it is independent of other systems, *i.e.* it can operate in a stand-alone mode,
- it is able to measure relative luminosity within 10% accuracy, and
- the data output from this system can easily be transmitted and interpreted.

The principle idea is to measure pile up events as an average current from a group of HF towers. The average energy deposition and its rms for a minimum bias event can be measured

and connected to the low luminosity zero measurement at some appropriate luminosity.

The rms and the average photoelectrons for a given bunch crossing are determined from the following relationships.

$$(rms) = G^2\mu(rms)^1 + G^2\mu <E>^2 + G\mu <E>$$

$$N_{pe} = G\mu < E > \quad (1)$$

The average energy deposition and rms of the energy deposition in one tower for a minimum bias event are <E> and $(rms)_1$, while μ is the average number of proton-proton interactions per bunch crossing and *G* is the number of photoelectrons per GeV of deposited energy in the calorimeter (~ 0.5 pe/GeV). For the outer ring towers, for example, at high luminosity, $(rms)/<N_{pe}>$ is about 2.9. For a group of 16 towers and <5% accuracy, 0.9 x 10^3 bunch crossings are needed.

Each tower is assumed to be calibrated prior to the HF installation and that each tower is gain monitored during data taking with the aid of LEDs and a laser system to maintain gains of each photomultiplier within 5% .

References

[1] The Compact Muon Solenoid. Letter of Intent. CERN/LHCC 92-3, LHCC/I 1, 1 October 1992.

[2] J. Ranft, Phys. Rev. D51 (1995) 64.

[3] P. Aurenche et al., Computer Physics Commun. 83 (1994) 107.

[4] P.A. Aarnio et al, CERN TIS-RP/168 (1986) and CERN TIS-RP/190 (1987)
A. Fasso et al., Proc IV Int. Conf. On Calorimetry in High Energy Physics, La Biodola, Sep 20-25, 1993, Ed. A. Menzione and A. Scribano, World Scientific, p. 493 (1993).

[5] S.Bertolucci et al., Nucl. Instr. and Meth. A254 (1987) 561.
D.Blomker et al., IEEE Transactions on Nuclear Science, Vol. 37/2(1990) 220.
J.P.Cumalat et al., Nucl. Instr. and Meth. A 293 (1990) 606.

[6] V. Abramov, Nucl. Instr. and Meth. A 374 (1996) 34.

[7] See: CDF End Plug Hadron Calorimeter Upgrade, P. de Barbaro at al, IEEE Trans. on Nucl. Science, vol 42, #4, p510-517).

[8] J.Freeman and W.Wu. FNAL-TM-1984 (August 1996).

[9] S. Abdullin, CMS-TN/94-180.

[10] I. Gaines et al., CMS-TN/96-058.

[11] S. Abdullin, at LHCC SUSY Workshop, CERN, October 1996.

[12] I. Gaines et al., CMS-TN/95-154.

[13] J. Freeman and W. Wu, Fermilab-TM-1984, 1996.

[14] *Scintillator Tile-Fiber Calorimeters for High Energy Physics: The CDF End Plug Upgrade, Selected Articles*., edited by P. de Barbaro and A. Bodek, University of Rochester preprint UR-1309, October 1994.

[15] P. de Barbaro et al., *Construction and Quality Control of Scintillator Tiles with WLS Fiber Readout for the 1995 CMS Test Beam Hadron Calorimeter*, University of Rochester preprint UR-1430, July 1995.

[16] K. Michaud et al., *Comparison of the 1995 H2 Test Beam data with the Geant Simulation of the CMS End Cap Calorimeter*, University of Rochester preprint UR-1432, CMS TN 95-116.

[17] P. de Barbaro et al., *Performance of the CMS Hadron Barrel Calorimeter Prototype using the 1995 Test Beam data*, CMS TN/96-077.

[18] Nucl. Instr. & Meth. Article in preparation.

[19] N. Akchurin et al., Beam Test Results from a Fine-Sampling Quartz Fiber Calorimeter for Electron, Photon and Hadron Detection, submitted to Nucl. Instr. Meth. Also CMS/TN 97-XXX.

[20] O. Ganel and R. Wigmans, Nucl. Instr. Meth. A365 (1995) 104.

[21] "GEANT" R. Brun et al., CERN DD/EE/84-1 (1987). See also CERN Program Library Long Writeup W5013 (1993).

[22] CMS Note 1996/020, D. Denegri and V. Genchev, "Study of the CMS hadron calorimeter barrel/endcap trtansition region".

[23] D. Litvintsev, CMS/TN 95-098.

[24] "PYTHIA: The Lund Monte Carlo for Hadronic Processes" H.U. Bengtsson and T. Sjostrand, Sep. 1991.

[25] "Study of degradation of the quartz HF response due to fiber radiation damage", D.

Litvintsev, CMS/TN 96-106.

[26] "Jet tagging and reconstruction over the expected pileup background in the CMS quartz fibres very forwardcalorimeters" A. Ferrando et al., CMS IN/97-xxx, May 1997.

[27] F. Paige and S. Protopopescu, BNL 38774 (1986).

[28] "Incoming particle rates, irradiation and power dissipation in the CMS very forward calorimeters due to the pileup bacckground" C. Burgos et al., CMS TN/95/035, March 1995.

[29] "Particle fluxes in the gaps of gas of the CMS iron/PPC very forward calorimeters due to the pileupbackground" A. Ferrando et al., CMS TN/95-036, RD37 TN/95-5, March 1995.

[30] "FLUKA92" A. Fasso, A. Ferrari, J. Ranft, P.R. Sala, G.R. Stevenson and J.M. Zazula, Proceedings of the Workshop on Simulating Accelerator Radiation Environments, Santa Fe, USA, January 1993.

Table of Contents